Interaction of atoms with intense laser fields and ultrashort pulses

by
M. Sci.. Carla Figueira de Morisson Faria

from Belém (Brazil)

Thesis presented at the Department 4 (Physics)
of the Technical University, Berlin
for obtaining the degree
"Doktorin der Naturwissenschaft"

Berlin, 1999
D 83

Evaluating committee:

President: Prof. Dr. Eckehard Schöll

First referee: Prof. Dr. Wolfgang Sandner

Second referee: Prof. Dr. Gebhard von Oppen

Thesis submitted on: March 23, 1999
Date of oral examination: May 19, 1999

Gedruckt mit Unterstützung des Deutschen Akademischen Austauschdienstes

"He who knows not and knows not he knows not, He is a fool- Shun him.
He who knows not and knows he knows not, He is simple- Teach him.
He who knows and knows not he knows, He is asleep- Awaken him.
He who knows and knows that he knows, He is wise- Follow him."

Bruce Lee

Contents

Chapter 1

Preface and general overview

The study of light-matter interaction processes at the atomic level has already a long tradition as an area of Physics [1]. More than one hundred years ago (more precisely in 1886 and 1887), Hertz realized that light could influence matter, observing that an electron discharge could be enhanced by ultraviolet light. At the beginning of this century, Albert Einstein proposed the existence of photons, and even raised the possibility that multiphoton processes might exist [2]. The first systematic studies of these processes, by Maria Göppert-Mayer, date from 1931 [3]. In the sixties, with the advent of laser sources, the external fields involved in the optical processes achieved higher intensities, and a wide range of new possibilities was opened. As a very important example, in 1961 Franken et al. [4] found that a ruby laser beam incident in crystalline quartz generates a very weak beam of UV radiation, its frequency being twice that of the ruby laser. Almost simultaneously, Kaiser and Garret reported a very similar experimental observation [5]. This was a clear sign that a medium can respond nonlinearly to external laser fields. Since then, nonlinear optics has evolved from a laboratory curiosity to a very important area in Physics, with applications in innumerous fields of science and technology, as diverse as, for instance, laser fusion, biomedical instrumentation or femtosecond spectroscopy [6]. Moreover, the development of laser sources made the study of multiphoton ionization possible [7], which has attracted the attention of several groups in the last three decades.

Up to one decade ago, all external fields involved either in these nonlinear interactions or in ionization processes were much weaker than the typical atomic binding forces. Thus, phenomena occurring in the context of the interaction of atoms and radiation were well described by perturbation theory in the external laser field. As a direct consequence, our whole physical intuition concerning such problems has been strongly influenced by this "perturbative viewpoint". Within the past decade, however, laser sources with peak intensities of the order of $10^{16} W/cm^2$ have become experimentally feasible. In this intensity regime, the external laser field is comparable to the binding energies of the electrons, and therefore it can no longer be treated as a perturbation [8]. The inadequacy of this theory has also been confirmed by several experimental observations concerning high-intensity optical phenomena, whose description require alternative theoretical methods [1]. Therefore, this intensity regime poses now a great challenge to both theoretical and experimental physicists, such that this field of research constitutes one of the most active areas within atomic physics. Apart from the understanding of the main effects like high-harmonic generation and ionization in strong laser fields, one expects possible applications for instance to plasma physics [10] (in particular fusion),

[1] In fact, experiments have shown that standard perturbation theory already fails for fields of the order of $10^{13} W/cm^2$. This is possibly related to the fact that, for these intensities, the stark shifts of the atomic levels become comparable to the photon energy, for typical frequencies used [9].

particle physics [11], XUV [12] and X-Ray sources [13].

Moreover, for laser intensities of the order of $10^{18} W/cm^2$, for typical frequencies, the kinetic energy transferred to the atomic system by the field is of the order of the rest mass of the electron [14][2]. This means that the laser-atom interaction needs a relativistic treatment [11, 15].

This thesis addresses mainly two high-intensity effects: high-harmonic generation (Part I) and atomic stabilization (Part II). These phenomena occur within the same physical framework, which is discussed in detail in Chapter 2.

High-harmonic generation (HHG) is a high-intensity phenomenon in which matter responds nonlinearly to an external laser field, emitting harmonics (i.e. coherent light whose frequency is a multiple of the frequency of the external field) up to more than the 100-th order. This effect was first observed independently in the late eighties, at the University of Illinois, Chicago [16], and in Saclay [17], in experiments related to harmonic generation in gaseous media subject to external fields of the order of $10^{13} - 10^{15} W/cm^2$. The emission spectra in these experiments presented very particular features, which turned out to be independent of the atomic species in question and can not be described by taking the field as a perturbation. In Chapter 3 these features, as well as our "perturbative expectations", are discussed in detail. Chapter 4 presents some of the widely used theoretical approaches to the problem, which will be useful in the subsequent chapters of Part I. These are concerned with a detailed investigation of the validity and limitations of such models, for monochromatic (Chapters 5 and 6) and bichromatic (Chapter 7) driving fields.

Roughly speaking, atomic stabilization means that atomic bound states become resistant to ionization in ultra-intense laser fields. This strong-field effect is a very controversial theoretical observation, and the first studies suggesting its existence reported strong deviations of ionization rates from the predictions of Fermi's golden rule [18, 19]. These rates started to decrease with the external field strength, provided the field intensity and frequency are high enough. Alternatively, several groups refer to a decrease in the ionization probability [3]. The existence or not of this phenomenon is not settled yet, since experimental measurements in the required intensity and frequency domain do not exist[4]. In Part II, analytical methods for investigating the absence or existence of stabilization with respect to the pulse shape are proposed and several examples are presented. In particular, in Chapter 9 a new mathematical method in this context is discussed and applied to the Hydrogen atom. In Chapter 10 , we investigate the connection between the absence or existence of this phenomenon and the total classical momentum transfer and displacement caused on the electron by the external field. Particularly in Sec. 10.2 this discussion is extended to a specific example, namely the one-dimensional delta potential. The computations of Part II were performed in collaboration with Dr. A. Fring and Prof. Dr. R. Schrader, of the theory group of the Free University Berlin.

In both parts, we concentrate on the single atom- field interaction. Effects such as the propagation of the harmonics in the gaseous medium [22, 23] or the interaction between strong fields and more complex systems, as for instance molecules [24, 25, 26], are not discussed in this work. Furthermore, we consider the atom to have only a single electron, assumption known as the Single Active Electron (SAE) approximation. Multielectronic effects such as electron-electron correlation or double ionization have been addressed, for instance, in [27, 28].

Part III is somehow different from Parts I and II . Therein, a nonlinear optical process involving much lower intensities is discussed: Second harmonic generation. For strictly monochromatic driving fields, this phenomenon is well-understood and can be found in every textbook on nonlinear optics. For short pulses, however, it is still an open problem to a very large extent (see e.g. [6, 29] for reviews

[2] Relativistic lasers already exist at the Lawrence Livermore Laboratory (USA), the University of Rochester (USA), Laboratoire d'Optique Appliquée (Paris), the Lund Laser Center (Sweden) and the Max-Born-Institut (Berlin).

[3] In Sec. 8.2, we provide a precise definition of stabilization, which is used throughout this work. One must note, however, that a unified definition of this phenomenon, within the scientific community, seems not yet to exist.

[4] Experimental evidence for some sort of stabilization is given in [20, 21], but these experiments do not deal with the "ultra-intense" regime for which the theoretical predictions are made.

on the subject). We present a general, nonstationary and analytical solution for the SHG problem, valid for a fundamental incident wave of arbitrary pulse shape, provided both fundamental and second harmonic waves are amplitude-modulated. This investigation is of interest in the context of the present work, since, under experimental conditions, high-intensity fields are only achieved using short-pulsed laser radiation. As a first approximation, high-intensity phenomena are investigated using strictly periodic fields. For instance, in Part I we address HHG using monochromatic and bichromatic driving fields, namely a high-intensity field of frequency ω and its second harmonic. However, in order to describe experiments quantitatively, one must use short pulses whose shapes are well determined. For bichromatic $\omega - 2\omega$ driving fields, for instance, realistic driving pulse shapes can be obtained using the results of Part III. This part also differs from Parts I and II in the sense that, instead of considering the response of a single atom to an external field, we look at the pulse propagation in the medium.This work was a result of a collaboration with the group 'Nichtklassische Strahlung' of the Humboldt University Berlin.

The appendices provide information of either complementary or technical nature, related to the main parts of this thesis. Appendix A presents the definition of the atomic units, which are used throughout. Harmonic generation and ionization within the weak-field regime are discussed in Appendix B, with emphasis on which aspects cease to be valid for high intensities. In Appendix C an important formula concerning ionization rates within the context of static fields, which is useful in Part I, is briefly recalled. The subsequent appendices concern the numerical methods used (Appendix D) and technical details of the derivations performed in Part II (Appendices E and F).

Chapter 2

Physical framework

The object of our investigations is an atom in the presence of a sufficiently intense [1] laser field, which may be described in the non-relativistic regime by the time-dependent Schrödinger equation in the dipole approximation

$$i\frac{\partial\left|\psi(t)\right\rangle}{\partial t} = H\left(t\right)\left|\psi(t)\right\rangle. \tag{2.1}$$

We use atomic units throughout. The time-dependent external electric field will be treated classically and is assumed to be linearly polarized (i.e. $\vec{E}(t) = E(t)\hat{e}_x$, where $\hat{e}_x$ denotes the unit vector in the x-direction), of the general form $E(t) = E_0 f(t)$, with E_0 being the field amplitude and $f(t)$ some arbitrary function which equals zero for $t < 0$ and $t > \tau$, such that τ defines the pulse length. Depending on the context it is convenient to express the Hamiltonian in equation (2.1) in different gauges. These gauge-equivalent Hamiltonians are connected by unitary transformations, which will be recalled below and are extensively used in this thesis, particularly in Part II.

2.1 Gauge equivalent Hamiltonians

Taking $\mathcal{A}_{j\leftarrow i}(t)$ to be a one parameter family of unitary operators, we may construct the gauge equivalent Hamiltonian $H_i\left(t\right)$ from $H_j\left(t\right)$ by the usual gauge transformation

$$H_i(t) = i\partial_t\mathcal{A}_{j\leftarrow i}(t)\mathcal{A}^{-1}_{j\leftarrow i}(t) + \mathcal{A}_{j\leftarrow i}(t)H_j(t)\mathcal{A}^{-1}_{j\leftarrow i}(t). \tag{2.2}$$

Choosing the most conventional gauge, the so-called length gauge, the Hamiltonian to describe the above mentioned physical situation is the Stark Hamiltonian

$$H^S_l(t) = H^0_l + V\left(\vec{\mathbf{r}}\right) + \vec{\mathbf{r}}\cdot\vec{E}(t). \tag{2.3}$$

$V\left(\vec{\mathbf{r}}\right)$ is the atomic potential and $H^0_l = \vec{\mathbf{p}}^2/2$ denotes the Hamilton operator of the free particle. We introduced here sub-and superscripts in order to keep track of the particular gauge we are in and to identify a specific Hamiltonian, respectively. In our conventions $\vec{\mathbf{p}}$ and $\vec{\mathbf{r}}$ denote operators, whilst $\vec{p}$ and $\vec{r}$ are elements in R^3. Other commonly used Hamiltonians are the one in the velocity gauge

$$H^S_v(t) = \frac{1}{2}(\vec{\mathbf{p}} - b(t)\hat{e}_x)^2 + V\left(\vec{\mathbf{r}}\right) \tag{2.4}$$

[1] "Sufficiently" refers to the validity of a classical treatment of the laser field. For very weak fields, a quantum-mechanical treatment is sometimes necessary (see for instance [30] for a discussion of physical effects related to the quantum-mechanical nature of the external field).

and the one in the Kramers-Henneberger (KH) frame [31]

$$H^S_{KH}(t) = H^0_l + V(\vec{\mathbf{r}} - c(t)\hat{e}_x). \tag{2.5}$$

These Hamiltonians may be obtained from each other by using

$$\mathcal{A}_{v\leftarrow l}(t) = e^{ib(t)\mathbf{x}}, \tag{2.6}$$
$$\mathcal{A}_{v\leftarrow KH}(t) = e^{-ia(t)}e^{ic(t)\mathbf{p}_x}, \tag{2.7}$$
$$\mathcal{A}_{l\leftarrow KH}(t) = e^{-ia(t)}e^{-ib(t)\mathbf{x}}e^{ic(t)\mathbf{p}_x}, \tag{2.8}$$

in (2.2). $\mathbf{p}_x$ is the component of the momentum operator in the x-direction. We have employed the important quantities

$$b(t) = \int_0^t ds\, E(s), \tag{2.9}$$

$$c(t) = \int_0^t ds\, b(s), \tag{2.10}$$

$$a(t) = \frac{1}{2}\int_0^t ds\, b^2(s), \tag{2.11}$$

which are the classical momentum transfer, the classical displacement and the classical energy transfer, respectively. These quantities have a slightly different physical meaning from the vector potential $A(t)$, its indefinite integral $F(t)$ and the indefinite integral $\int dsA^2(s)$, which are also used, within the atom physics community[2], in the transformations (2.6)-(2.8) and the Hamiltonians (2.4) and (2.5). By taking *definite* integrals in (2.9)-(2.11) we are fixing initial conditions for the physical problem. In other words, we impose that, at t=0, the momentum transfer, the classical displacement and the energy transfer caused on the atom by the field are zero. This makes physically sense, since at $t = 0$ no electric field is yet present. This condition is not always fulfilled by the vector potential $A(t)$. For instance, for an instantaneously switched-on monochromatic field, $E(t) = E_0 \sin\omega t$, $A(0) = E_0/\omega$.

In Part I, these details are not relevant to the physical discussion. First, this problem does not appear since we take, in all computations (see, Chapter 4, specifically Sec.4.3), $A(t)$ to be smoothly switched-on, such that in this particular case $b(t) = -A(t)$. Second[3], the phenomenon we are investigating is mainly originated by the periodic character of the field, instead of its turn on and off. To emphasize this, we use (and refer to) $A(t)$ in all Hamiltonians and gauge transformations therein. In Part II, however, these distinctions will become important, since the total momentum transfer and the classical displacement at the end of the pulse, $b(\tau)$ and $c(\tau)$, are the crucial parameters for the description of the phenomenon we are going to discuss[4]. These parameters are highly dependent on how the pulse is switched on and off. For several pulse shapes, it is not only necessary to guarantee that no momentum transfer has occurred at $t = 0$, but also that this momentum transfer takes place continuously in time. In some particular cases, the use of $A(t)$ may artificially introduce "kicks" in the electron at the end of the turn-on, or extra time-dependent terms

[2] The notations presented here are, however, extensively used within Mathematical Physics, for the reasons discussed in this chapter (see also [32]).

[3] For HHG involving ultrashort pulses, these parameters may have a larger influence. Studies on this subject have been recently initiated in [33].

[4] The classical energy transfer $a(t)$ is not a crucial quantity since it enters all expressions only as a phase and will therefore cancel in all relevant physical expressions.

in the classical displacement, and yield misleading results [5]. Some artificial results obtained by these discontinuities are discussed, for instance, in [34], within the context of atomic stabilization.

In our considerations we will also need the Hamiltonians

$$H^A_l(t) = H^0_l + V(\vec{\mathbf{r}}), \quad H^{GV}_l(t) = H^0_l + \mathbf{x}E(t) \tag{2.12}$$

which describe an electron in the atomic potential or in the electric field, respectively. Of course these Hamiltonians may also be transformed into the other gauges by (2.6)-(2.8). Notice that $H^{GV}_{KH}(t) = H^0_l$.

Another useful unitary transformation, related to the elimination of the purely time-dependent term in the Hamiltonian (2.4), is given by

$$\mathcal{A}_{\tilde{v}\leftarrow v}(t) = e^{-ia(t)}. \tag{2.13}$$

This transformation is used for instance in Sec. 4.3.

[5] For instance, for a trapezoidal (i.e. linearly switched on and off) electric field, there is a discontinuity for the vector potential at the end of the switch-on ramp, in case the switch-on time differs from an integer number of half cycles of the field. This discontinuity does not exist for $b(t)$.

Part I

High-harmonic generation

Chapter 3

Introduction

Harmonic generation owes its existence to the nonlinear response of the time-dependent atomic dipole moment to an external laser field. The emission spectrum is proportional to the modulus square of the Fourier transform of this quantity, taken in its length ($r(t)$)or acceleration form ($\ddot{r}(t)$). For weak fields, it is a standard and well-understood problem, well-explained by taking the electric field as a perturbation. However, in the experiments reported in [16, 17], after the expected decrease of the low-order harmonics, the spectra presented a long frequency range with harmonics of roughly the same intensities, the so-called "plateau", followed by an abrupt decrease in the harmonic yield, the so-called "cutoff". Intuitively, one would expect a monotonic decrease in the harmonic intensity with harmonic order. Surprisingly, a computation performed in [35] using perturbative methods concerning the field predicts a "mountain" (i.e. too strong harmonic yields) for the higher harmonics, after this initial decrease. As an illustration, Fig. 3.1 shows measurements of the harmonic intensity as a function of the harmonic wavelength in the plateau and cutoff regions, obtained experimentally for Neon at the Max Born Institute [36], with a Ti:Sa laser system. The harmonic orders are also marked in the figure. One clearly sees an emission spectrum constituted of odd harmonics [1], with a sharp intensity decrease after H53.

Several experiments of the same type confirmed that these features are independent of the gaseous species involved [37, 38, 39]. Detailed investigations showed the decrease of the cutoff energy for higher frequencies and its increase with the intensity of the external field and the ionization potential[2] of the atomic species in question [38]. These results already suggested the existence of a simple, explicit and universal cutoff law. Several models, such as the three-step model [40, 41, 42], a driven two-level atom [43, 44, 45, 46], the fully numerical solution of the time-dependent Schrödinger equation (TDSE) [47, 48, 49, 50], and the Floquet approach [51], were concerned not only with the obtention of this law, but with the description and understanding of the mechanisms involved in high-harmonic generation altogether. Particularly the three first theoretical approaches will be discussed in detail in Chapter 4.

The cutoff law which showed the best agreement with the experiments was first obtained empirically in 1992 after detailed theoretical studies based on a TDSE computation [49], for several one- and three-dimensional model atoms, including rare gases, Hydrogen, and various short- and long range potentials. According to this law, the maximal harmonic photon energy is given by $\varepsilon_{max} = |\varepsilon_0| + 3.17U_p$. Here ε_0 is the field-free binding energy of the ground state and U_p the ponderomotive energy of an electron in the laser field. This latter quantity is proportional to the

[1] For a gas, due to symmetry considerations, even harmonics are absent. For more details we refer to [6] and Appendix B.

[2] The gases for which HHG experiments were most efficiently performed turned out to be rare gases, for which this quantity is particularly high.

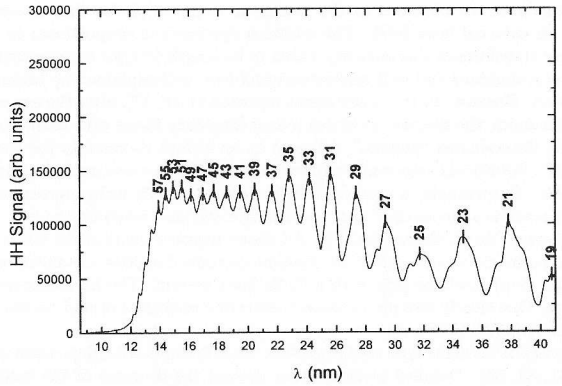

Figure 3.1: Harmonic spectrum for Neon, for a Ti:Sa laser system with peak intensity of the order of $10^{15} W/cm^2$ and wavelength of $795nm$. The measurement was performed by G. Sommerer et. al. at the Max Born Institute, Berlin.

driving laser field intensity (defined as the energy flux per unit area) and inversely proportional to the square of its frequency. The same cutoff law is not only recovered, but also explained by the three-step model, which was an extremely important step towards the understanding of high-harmonic generation. The original idea for this model was given in [40], and its full quantum-mechanical development was achieved in the early nineties [41, 42][3]. Since then, the three-step model has been checked and confirmed by several other methods, like the TDSE [50] and time-frequency analysis [52, 53, 54, 55, 56, 57], with good agreement both for the spectral and temporal profiles of the harmonics. This is one of the reasons why the three-step model has become the current paradigm for describing HHG. The other reason is its simplicity: until its development, the TDSE provided the closest reproduction of the experimental results [47, 49]. However, for a realistic, three-dimensional model-atom, the fully numerical solution is extremely demanding in terms of computer time. In fact, in order to reproduce experiments accurately, one must take into account a gaussian beam interacting with an atomic *ensemble*. Therefore, the single-atom response computation must be performed in each point of the gaseous sample, and these results must be propagated in the gaseous medium using Maxwell's equations [22, 23]. Only the study of these collective effects already requires considerable numerical efforts (in order to give an idea of the complexity of these computations we refer, for instance, to [58]).

In this work, only the single-atom response will be discussed. However, one should keep in mind that propagation may strongly affect the harmonic signal. In order to achieve a good conversion efficiency, the harmonics generated in each point of the medium must be phase-matched, i.e., they must be in phase, such that the corresponding electric fields do not interfere destructively. Several collective effects may be detrimental to phase matching. For instance, the phase of the emitted harmonics, with respect to the driving field, is extremely intensity-dependent [59]. Since the incident laser beam has a gaussian intensity distribution, harmonics emitted by atoms in different points of the medium have in principle different phases. Phase-matching is also influenced by the spatial change of the geometrical phase of the laser beam, which may lead to a substantial spectral, temporal and spatial broadening of the harmonic signal [60]. Moreover, ionization introduces dispersion in the medium, through depletion (which introduces a time dependence in the atomic density) and the release of free electrons. This dispersion influences the propagation velocity of the harmonics. Other propagation-related effects are for instance the enhancement or suppression of groups of harmonics and the shift of the cutoff towards lower energies. Furthermore, phase-matching effects in HHG can in principle be used in the production of attosecond pulses [61, 62].

High-harmonic generation has also attracted a lot of attention in the last few years due to a wide range of possible applications. For instance, the fact that the plateau may extend to very high frequencies (see, e.g., [39], in which the observation of the 169th harmonic of an 800nm laser, i.e., 4.7 nm, has been reported; in average, nowadays frequencies up to the order of 7nm have been reached by several groups [38]) makes HHG very attractive as XUV and soft X-Ray sources. The advantage of high-order harmonics over more traditional sources of XUV radiation[4] is that it preserves the characteristics of the driving laser field, i.e., of short pulse duration, coherent and narrowband.

Part I is outlined as follows: in Chapter 4, we discuss the three-step model (Sec. 4.1), the two-level atom (Sec. 4.2), the TDSE (Sec. 4.3), and the time-frequency or wavelet analysis (Sec. 4.4), providing the necessary theoretical and methodical background for understanding our results. In order to make this background complete, especially for Secs. 4.3 and 4.4, we discuss some aspects which have so far received little or no attention in the current literature. The main results of Part I are presented in Chapters 5, 6 and 7. In Chapter 5, we perform a comparison between the TDSE

[3] Roughly speaking, the three-step model states that high-harmonic generation is mainly a consequence of the recombination of an electron driven by the external laser field with its parent ion. A more precise definition will be given in Sec. 4.1.

[4] Examples of "traditional XUV sources" are synchroton radiation [63], X-ray lasers [64], or the radiation from laser-produced plasmas [10].

and the three-step model using time-frequency analysis, with the objective of identifying the main contribution to HHG within a field cycle. The influence of the excited bound states in harmonic generation is discussed in Chapter 6, in which, among other studies, we compare the TDSE to a two-level atom. Chapter 7 addresses HHG by bichromatic driving fields, with emphasis on the time profile of harmonic generation (Sec. 7.1) and the investigation of an explicit cutoff law (Sec. 7.2). These studies required a high degree of numerical analysis, with the development of computer codes for each theoretical approach of Chapter 4. The numerical methods used are discussed in Appendix D.

Chapter 4

Theoretical approaches

4.1 Three-step model

The most successful model for describing HHG, the so-called "three-step model" is based on a very simple idea: As the "first step", the atom ionizes through tunneling or multiphoton ionization, at the start time t_0. The newly-freed electron is then accelerated by the external field (the "second step") and, depending on its time of ionization, may be driven back towards the ionic core to recombine with the ground state at the return time t_1, generating harmonics in this process (the "third step"). During the electron's excursion in the continuum, the influence of the potential is neglected. This is reasonable for intense laser fields and should clearly work better for shorter-range potentials. Thus, the atom acts simply as a source for the electrons, for the first "step" and as a nonlinear interaction for the third "step", while the atomic internal structure, notably its excited states, play no important role in the process. The cutoff in the harmonic spectra corresponds to the maximal kinetic energy of the electron upon return.

The ionization mechanism is determined by the important parameter

$$\gamma = \sqrt{\frac{|\varepsilon_0|}{2U_p}}, \tag{4.1}$$

connecting the field-free ground state energy ε_0[1] to the ponderomotive energy U_p(given by the time average of the square of the vector potential), whose origin is related to the work of Keldysh concerning ionization processes in strong fields [65]. The Keldysh parameter separates regions of different physical behavior: for $\gamma < 1$, tunneling takes place, whereas for $\gamma > 1$, multiphoton ionization occurs. For typical field frequencies and intensities related to the observation of HHG, the first step is predominantly a tunneling process. Intuitively, this also explains part of the success of the three-step model for describing experimental results, since, for $\gamma > 1$, atom-laser resonances (and therefore the atomic internal structure) should play a relatively important role. In a tunneling process, the external field considerably distorts the atomic potential, such that the electron, in order to leave the atom, must tunnel through the resulting time-dependent potential barrier, given by

$$V_{eff} = V(r) - \vec{r} \cdot \vec{E}(t). \tag{4.2}$$

Using this physical picture (i.e., of a distorted effective potential), one can also interpret the Keldysh parameter as being roughly the ratio of the tunneling time (i.e., the width of the barrier divided by

[1] Strictly speaking, γ may be defined with respect to *any* field-free bound-state, of energy ε_n. For our purpose, we take the ground state.

the electron velocity) to the period of the driving field. If the field frequency is very low ($\gamma \ll 1$), there is enough time for the the electron to tunnel through the barrier, such that, to good approximation, the field is considered as being static. In the opposite regime ($\gamma \gg 1$) the atom is driven back and forth by the field too rapidly for tunneling to occur. Thus, ionization takes only place due to multiphoton processes. Strictly speaking, in most cases an "intermediate" behavior is observed, which, depending on γ, presents features which are either characteristic of tunneling or multiphoton ionization. The larger or smaller γ, the more "tunneling-" or "multiphoton-like" the ionization process.

Figures 4.1 and 4.2 present schematic illustrations of the three-step model. In Fig. 4.1, we concentrate on the three-steps, i.e., ionization (S_1), propagation (S_2) and recombination (S_3), whereas in Fig. 4.2 we emphasize the tunneling process through the effective potential barrier, as well as the relation between the kinetic energy of the electron and the emitted harmonic frequencies.

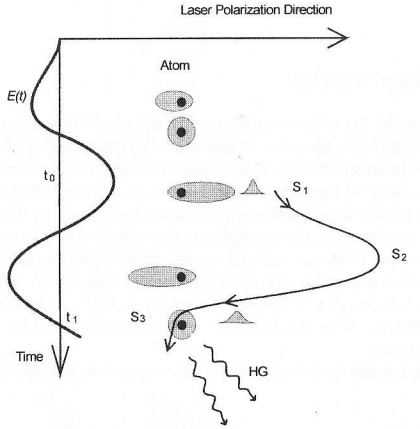

Figure 4.1: Schematic illustration of the three-step model. The electron, given by the wave packet in the figure, leaves the atom at t_0, when the atom is strongly distorted by the field, being driven back at t_1, emitting harmonics. The first, second and third steps are given, respectively, by S_1, S_2 and S_3.

Another important point concerning the multiphoton or tunneling regime is related to the injection of the electron in the continuum: The emission rate for an electronic wave packet in the tunneling regime ($\gamma < 1$) is proportional to $\exp\left[-C/|E(t)|\right]$ [66], where the constant C depends on the potential barrier in question. In the multiphoton regime, the emission of the electron in the continuum is equally probable for all times.

In the next subsections, the semiclassical [40] (also known as "simpleman's model") and quantum mechanical approaches [41, 42] to this model will be discussed.

4.1.1 Semiclassical description and graphical method

The "simpleman's model" mixes quantum-mechanical effects, such as tunneling or multiphoton ionization and recombination (the first and third "steps"), with the propagation of a classical particle

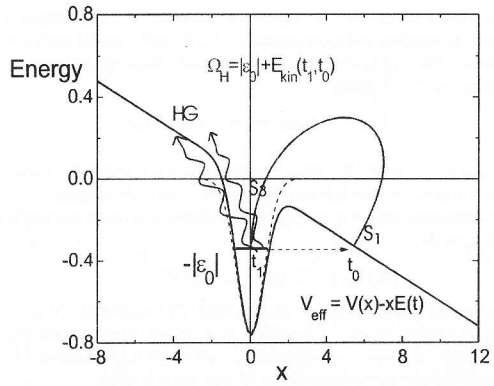

Figure 4.2: One-dimensional illustration of the tunneling and recombination processes in the three-step model. The undistorted and distorted potential are given, respectively, by the dashed and solid lines. The frequency of the harmonic photon corresponds to sum of the kinetic energy of the electron and the energy gained by the recombination, i.e., $|\varepsilon_0|$, and is denoted by Ω_H. The upgoing arrows represent the harmonic generation process, and the curve connecting the "steps" S_1 and S_3 is an auxiliary construction, illustrating the electron trajectory in the continuum.

in the time-dependent continuum. Already within this framework, some of the most important features concerning HHG, like the cutoff law, are already recovered, as shown below.

Let us consider a classical electron, assumed to be released in a time-dependent laser field at $t = t_0$ with zero velocity. Since the field is taken to be linearly polarized, all the ensuing motion takes place in its direction, to which we shall mainly refer. Classically, the electron propagates in the continuum according to the equation of motion

$$\ddot{x}(t) = -dV(x)/dx + E(t). \tag{4.3}$$

For the intensities involved, the first term on the right-hand side of (4.3) can be neglected. Being subject just to the laser field, it returns at $t = t_1$ to the site of its release (the position of its parent ion, at $x = 0$) recombining with the potential and emitting harmonics. In the whole process, canonical momentum is conserved, so that the electron velocity and its coordinate x as functions of time are given respectively by

$$v(t) = A(t) - A(t_0) \tag{4.4}$$

and

$$x(t) = (t - t_0)\, A(t_0) - \int_{t_0}^{t} ds\, A(s), \tag{4.5}$$

with $A(t)$ being the vector potential. At a certain time t the electron will therefore have the kinetic energy $E_{\rm kin}(t, t_0) = \frac{1}{2}\left[A(t) - A(t_0)\right]^2$, which corresponds to a harmonic photon with frequency $\Omega = |\varepsilon_0| + E_{\rm kin}(t_1, t_0)$. A pair (t_1, t_0) for which $E_{\rm kin}(t_1, t_0)$ is extremal will correspond to a cutoff frequency. These emission and return times can be found by means of a simple graphical method, which has been successfully used in the context of high-harmonic generation and above-threshold

ionization[2] with bichromatic fields [67, 57] (see also Chapter 7). The advantage of the graphical method is that it allows to qualitatively understand, check, and predict such results on the back of an envelope, for arbitrary field configurations, provided only that the polarization is linear.

The return condition $x(t_1) = 0$ yields

$$F(t_1) = F(t_0) + (t_1 - t_0)\, F'(t_0), \tag{4.6}$$

with $F(t) = \int^t ds A(s)$ and $F' \equiv dF/dt$. This means that, for a given emission time t_0, the return time t_1 ($t_1 > t_0$) is determined by the intersection of $F(t)$ with its tangent at $t = t_0$ for $t > t_0$. For the cutoff, using the condition $\partial E_{\rm kin}(t_1, t_0)/\partial t_0 = 0$, where t_1 and t_0 are connected by the return condition (4.6), one can write

$$A(t_0) = A(t_1) - (t_0 - t_1)\, E(t_1), \tag{4.7}$$

which, this time, asks to find the intersection of $A(t)$ with its tangent at $t = t_1$ for $t < t_1$. Equations (4.6) and (4.7) determine pairs (t_1, t_0) of emission and return times which yield extremal kinetic energies upon return.There is always an infinity of solutions to equations (4.7) and (4.6). The various t_0 and t_1 depend on the time-dependence of the electric field.

For a monochromatic field of amplitude E_0 and frequency ω, i.e.,

$$E(t) = E_0 \sin(\omega t), \tag{4.8}$$

this method yields one pair of maximal-energy emission and return times, $t_0 \simeq 0.3T$ and $t_1 \simeq 0.95T$, which corresponds to the well-known cutoff energy

$$\varepsilon_{\rm max} = |\varepsilon_0| + 3.17 U_p. \tag{4.9}$$

The ponderomotive energy U_p is defined as the time-average of the square of the vector potential within a field cycle $T = 2\pi/\omega$, and, for the specific case of a monochromatic field given by $U_p = E_0^2/4\omega^2$. A quick inspection of the cutoff expression (4.9) confirms all results observed experimentally, i.e., that the plateau should reach higher harmonic orders for higher intensities and ionization potentials and lower frequencies. An illustration of the graphical method concerning the cutoff $\varepsilon_{\rm max}$ is presented in Fig. 4.3(a). In part (b) of the same figure, we show how this method can be extended to bichromatic fields, finding a cutoff trajectory for a driving field which is a superposition of (4.8) with its second harmonic. The two straight lines in both parts satisfy the conditions of equations (4.7) and (4.6), respectively, and thus determine a pair of emission and return times.

Equations (4.6) and (4.7) can also be solved analytically in the specific case of a monochromatic field using an adequate change of variables [42]. Therein, another simple argument concerning the cutoff law is presented: the time average of $E_{\rm kin}(t, t_0)$ for a monochromatic field is given by

$$\langle E_{\rm kin}(t, t_0) \rangle = U_p \left(1 + 2\cos^2 \omega t_0\right). \tag{4.10}$$

Clearly, its maximum as a function of t_0, $3U_p$, roughly corresponds to the harmonic photon given by (4.9).

Apart from the well-known cutoff energy $\varepsilon_{\rm max}$, additional cutoffs which correspond to longer excursion times of the electron in the continuum also exist. With the restriction $t_1 - t_0 \leq 2T$, these cutoffs are at $\varepsilon_{1\,\rm max} = |\varepsilon_0| + 1.54 U_p$ and $\varepsilon_{2\,\rm max} = |\varepsilon_0| + 2.4 U_p$. For the former cutoff, ionization and recombination take place at, respectively, $t_0 \simeq 0.3T$ and $t_1 \simeq 1.5T$, whereas for $\varepsilon_{2\,\rm max}$ the free-electron "born" at the same time returns at $t_1 \simeq 2T$. These cutoffs do not contribute significantly to harmonic generation, due to the spreading of the electronic wave packet. This effect is of quantum-mechanical nature and will be discussed in more detail in the following subsection.

[2] "Above-threshold ionization" is a strong-field phenomenon in which an atom absorbs more photons that are actually necessary for it to ionize; see e.g. [8] for a review on the subject.

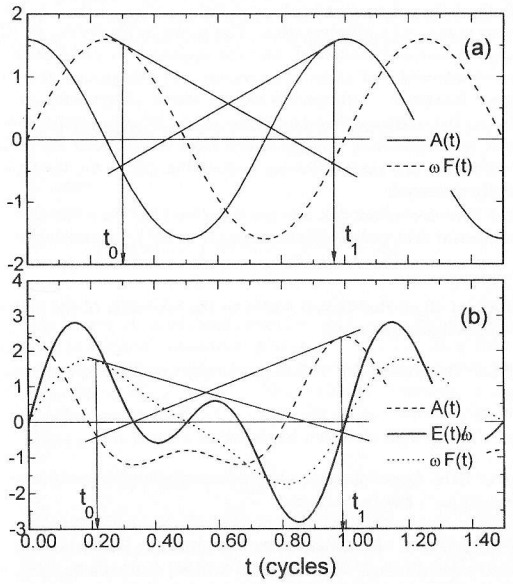

Figure 4.3: Graphical method for a monochromatic field of the form (4.8)(Part (a)), with $E_0 = 0.08$ *a.u.*, and a bichromatic field of the form $E(t) = E_0(\sin(\omega t) + \sin(2\omega t))$, with $E_0 = 0.04$ *a.u.*(Part (b)). For both fields, $\omega = 0.05$ *a.u.* The thin straight lines in both parts yield the return and the cutoff conditions, given respectively by Eq. (4.6) and (4.7). The emission and return times, given by respectively t_0 and t_1 in the figure, yield $E_{kin}(t_1, t_0) = 3.17 U_p$(Part (a)) and $E_{kin}(t_1, t_0) = 4.86 U_p$ (Part (b)). One should note that $\omega F(t)$ and $E(t)/\omega$ overlap for the monochromatic case.

4.1.2 Quantum mechanical description

The semiclassical description explains very well the cutoff law and the emission and return times for an electron in a field, which, within the three-step model framework, correspond to the main contributions to HHG within a field cycle T. However, it does not take into account important quantum-mechanical effects, such as the quantum diffusion of the electronic wave packet and the interference of two or more semiclassical trajectories for the returning electron. Throughout this thesis, it will become clear that such effects play a very important role in high-harmonic generation. Their study requires a fully quantum-mechanical three-step model. Two closely related theoretical approaches exist, both of them keeping the physical transparency of the "simpleman's model" and being of relatively easy numerical implementation: The model by Becker et. al. [42], which calculates HHG for a zero-range potential atom-model, and the approach by Lewenstein et. al. [41], which considers an arbitrary potential, but takes into account only the ground state and the continuum, using a series of approximations. Both models can be solved analytically up to a quadrature: In the former case, due to the mathematical properties of the delta potential, and in the latter case, due to a saddle-point approximation, through which most integrations are performed. A detailed discussion of their differences and similarities can be found in [68]. Here, the approach of Lewenstein et.al.[41] will be briefly discussed.

We start from the time-dependent Schrödinger equation (2.1) for a one-electron atom subject to a linearly polarized electric field in the length gauge ($H = H_l^S$), considering the following approximations:

1. The contribution of all excited bound states to the evolution of the system is negligible (we consider a single-bound-state atom).

2. In the continuum, the potential $V(\mathbf{r})$ has practically no effect on the motion of the electronic wave packet.

3. The depletion of the ground state can be neglected.

4. Contributions to HHG from transitions between continuum states (the so-called "continuum-continuum transitions") can be neglected[3].

Assumption 1 is expected to be reasonable for the tunneling ionization regime. Its validity and the role of the atomic excited bound states in HHG will be discussed in more detail in Chapter 6. Assumption 2 clearly holds for short-range potentials and is also reasonable for hydrogenlike atoms in case $U_p \gg |\varepsilon_0|$. Assumption 3 is valid provided it takes many cycles of the driving field for the atomic ground state to ionize completely, which is the case for typical field strengths used in HHG experiments. Assumption 4 has been extensively investigated in [68] and has proven to hold reasonably well. With assumptions 1 and 2, the time-dependent wave function can be written as a superposition of the ground-state $|0\rangle$ and continuum states $|\vec{v}\rangle$,

$$|\psi(t)\rangle = e^{i|\varepsilon_0|t}\left(C_0(t)\,|0\rangle + \int d^3v C_v(\vec{v},t)\,|\vec{v}\rangle\right), \tag{4.11}$$

where the ground-state and continuum amplitudes are given respectively by $C_0(t) \simeq 1$ (assumption 3) and $C_v(\vec{v},t)$. For the amplitude $C_v(\vec{v},t)$, the Schrödinger equation can be solved analytically and

[3] One of the main differences between the models [41] and [42] concerns the neglect of these transitions. Concerning the physical predictions of [41] and [42], discrepancies in the behavior of plateau harmonics with the ellipticity of the driving field were observed [68].

yields

$$C_v(\vec{v},t) = i\int_0^t dt_0 E(t_0) d_x(\vec{v}+\vec{A}(t)-\vec{A}(t_0)) \exp\left\{-i\int_{t_0}^t dt''\left[(\vec{v}+\vec{A}(t)-\vec{A}(t_0))^2/2+|\varepsilon_0|\right]\right\}. \tag{4.12}$$

In this derivation, also assumption 4 was taken into account. Equation (4.12) shows that all the dependence on the potential lies in the matrix element $d_x(\vec{v}) = \langle\vec{v}|\,\mathbf{x}\,|0\rangle$. The choice of this matrix element may affect the harmonic spectra quantitatively [41], as well as the time profile of some groups of harmonics (see e.g. Chapter 5 of this thesis and [55]). In this work, we will adopt a 1D three-step model, for which $x(t)$, written in terms of the canonical momentum $p = v + A(t)$, is given by

$$x(t) = \int_0^t dt_0 \int dp E(t_0) d_x(p - A(t_0))\, d_x^*(p - A(t)) \exp\left[-iS(p,t,t_0)\right] + c.c, \tag{4.13}$$

with the time-dependent action

$$S(p,t,t_0) = \int_{t_0}^t dt'' \frac{(p - A(t''))^2}{2} + |\varepsilon_0|. \tag{4.14}$$

Equation (4.13) has a simple physical interpretation: at $t = t_0$, the electron makes a bound-continuum transition with probability amplitude $E(t_0)d_x(p - A(t_0))$. It is then propagated from t_0 to t, with the time-dependent phase $\exp[-iS(p,t,t_0)]$ and recombines with the ground state at t, with the probability amplitude $d_x^*(p - A(t))$. The oscillatory behavior of the time-dependent dipole moment is mainly determined by $S(p,t,t_0)$, and the major contribution to $x(t)$ comes from its stationary points. These points correspond to

$$\nabla_p S(p,t,t_0) = x(t) - x(t_0) = 0. \tag{4.15}$$

Physically, the condition (4.15) means that the main contributions to HHG come from an electron freed at t_0, returning to the origin at t, which is exactly the rescattering condition of Sec. 4.1.1. This is not a coincidence: in classical mechanics, the equations of motion are determined by the condition that the classical action be extremal [69]. With respect to the momentum p, there is a single point p_{st} which satisfies this condition. One can perform the integral in momentum space in (4.13) very easily expanding the action around p_{st}:

$$S(p,t,t_0) \simeq S(p_{st},t,t_0) + \frac{1}{2}(p - p_{st})^2 \frac{\partial^2 S}{\partial p^2}\Big|_{p=p_{st}}. \tag{4.16}$$

The momentum and time-dependent dipole moment at the stationary point are given respectively by

$$p_{st} = \frac{1}{t - t_0}\int_{t_0}^t A(t'')dt'' \tag{4.17}$$

and

$$x(t) = \lim_{\epsilon\to 0} i\left(\frac{\pi}{\epsilon + i/2(t-t_0)}\right)^{1/2}\int_0^t dt' d_x(p - A(t_0))\, d_x^*(p - A(t)), \tag{4.18}$$

where the constant ϵ was introduced such that (4.18) does not diverge for $t = t_0$. The term multiplying the integral on the right hand side of (4.18) corresponds to the spreading of the electron wave packet. From its form, it is obvious that the larger the time difference between emission and return times, the smaller the contributions to HHG. For a 3D model [41], the saddle point integration yields an exponent 3/2 instead of 1/2 in (4.18). Physically, this difference is related to the transverse spreading of the wave packet. For the one-dimensional model, the higher-order returns to the origin, with longer excursion times for the electron, tend to be enhanced in probability. Consequently, their contributions to HHG are more pronounced in this case.

Equation (4.18) was calculated imposing an extremal condition in $S(p, t, t_0)$only with respect to p. According to the principle of the minimal action, a classical electron would follow a trajectory satisfying (4.15), and the additional conditions

$$\frac{\partial S(p,t,t_0)}{\partial t} = 0, \tag{4.19}$$

$$\frac{\partial S(p,t,t_0)}{\partial t_0} = 0, \tag{4.20}$$

which are fulfilled by *several* pairs (t_1, t_0). Thus, equation (4.18) for the time-dependent dipole moment in fact comprises several classical trajectories. More details on the saddle point method can be found in [41]. As an illustration, in Fig. 4.4 we present the emission and return times (t_1, t_0) for a classical electron in a monochromatic external field as a function of its kinetic energy upon return, $E_{\rm kin}(t_1, t_0)$. $E_{\rm kin}$ is plotted on the horizontal axis in units of the ponderomotive potential, and the associated values of the emission and return times t_0 and t_1 are given in the lower and the upper part of the figure, respectively. The diagram was obtained from the numerical integration of the classical equation of motion (4.3) using a fourth-order Runge-Kutta method. The influence of the binding potential was neglected in this calculation. Each triplet $(t_0, t_1, E_{\rm kin}(t_1, t_0))$ is associated with a classical trajectory for the returning electron. A similar diagram is also presented in [54]. The extremal energies, marked with arrows, correspond to the cutoff trajectories $\varepsilon_{\rm max} = |\varepsilon_0| + 3.17U_p$, $\varepsilon_{1\,\rm max} = |\varepsilon_0| + 1.54U_p$ and $\varepsilon_{2\,\rm max} = |\varepsilon_0| + 2.4U_p$. Each of these maximal-energy trajectories splits into two, corresponding to a shorter and a longer excursion time for the electron in the continuum. Thus, for a given $E_{\rm kin}(t_1, t_0)$, there may be many possible trajectories for the returning electron. Quantum-mechanically, the probability amplitudes related to the electron following each of these trajectories interfere. For the most energetic cutoff, the single pair (t_1, t_0) mentioned in Sec. 4.1.1 can be clearly seen. The shorter and longer excursion times resulting from the splitting of the maximal-energy trajectory $\varepsilon_{\rm max}$, denoted by respectively τ_1 and τ_2, are also shown in the figure, marked by thick arrows.The corresponding two return times have recently been observed in experiments [70]; see also Ref. [23, 59, 60].

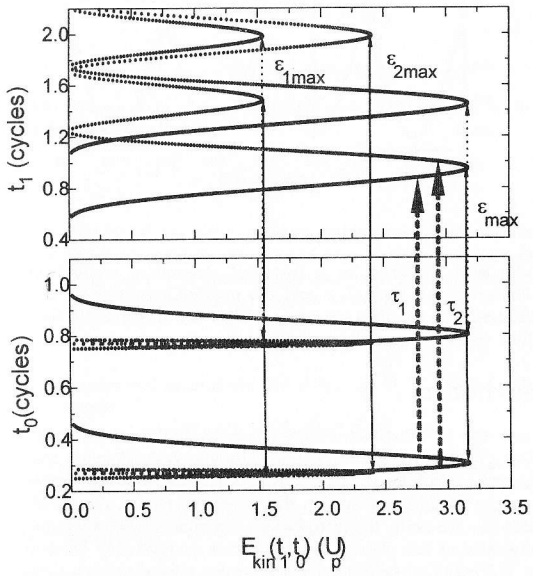

Figure 4.4: Emission and return times for an electron in a monochromatic field, as functions of its kinetic energy upon return. The upper and lower parts of the figure yield respectively the return and emission times, given in field cycles. The kinetic energy $E_{\rm kin}(t_1, t_0)$ is given in terms of the ponderomotive energy. The emission and return times corresponding to the cutoff energies $\varepsilon_{\rm max}$, $\varepsilon_{2\,\rm max}$ and $\varepsilon_{1\,\rm max}$are marked with thin arrows. The splitting of the emission and return times for the most energetic cutoff into a shorter $(t_1 - t_0 = \tau_1)$ and longer $(t_1 - t_0 = \tau_2)$ excursion times are shown with thick dashed arrows. All trajectories are periodic within $T/2$.

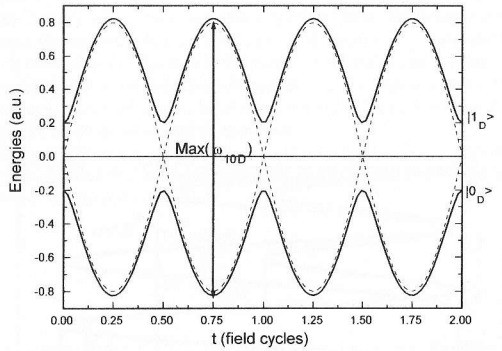

Figure 4.5: Periodic level crossings for a two-level atom in a monochromatic field $E(t) = 0.8\sin(0.05t)$.The dressed states $|0_D\rangle, |1_D\rangle$ and the avoided crossings are shown respectively by the solid and dotted lines. The maximal harmonic energy, which represents the cutoff in this model, is marked with a thick arrow.

4.2 Two-level atom

Harmonic spectra can also be described within a completely different physical picture, namely a driven two-level atom [43, 44], for which bound-continuum transitions do not exist. This model also yields a plateau and a cutoff for the harmonic spectra. However, the plateau comprises a much narrower frequency range in this case than in the three-step model, the cutoff being proportional to the field amplitude E_0. Recently, the introduction of ionization rates within this model resulted in a considerable extension of this plateau towards higher energies [44]. Within the two-level atom picture, the plateau and cutoff of the harmonic spectra are related to periodic level crossings of the time-dependent dressed states, which occur at every half cycle of the driving field, close to minimal field. An illustration is given in Fig. 4.5 for a monochromatic driving field of the form (4.8). One clearly sees that the time-dependent dressed states follow the field adiabatically, except close to the avoided crossing. This originates a highly nonlinear behavior in the time-dependent atomic dipole moment for this temporal region.We refer to [46] for a detailed discussion of this mechanism.

We shall address now the driven two-level atom case in detail, with and without ionization. A comparison between this model and results from a TDSE computation will be presented in Chapter 6. For a "closed" (non-ionizing) two-level atom in an external field $E(t)$, the time-dependent wave function and Hamiltonian are given by, respectively [71],

$$|\psi(t)\rangle = C_0(t)\,|0\rangle + C_1(t)\,|1\rangle \tag{4.21}$$

and

$$H = H_A + H_I. \tag{4.22}$$

The amplitudes $C_n(t)$, $n = 0, 1$ are $C_n(t) = \langle n|\psi(t)\rangle$. The indices 0 and 1 relate to respectively the

ground and excited state. The atomic Hamiltonian is

$$H_A = |0\rangle\,\varepsilon_0\,\langle 0| + |1\rangle\,\varepsilon_1\,\langle 1|\ , \tag{4.23}$$

with ε_n the field-free energies, such that $H_A\,|n\rangle = \varepsilon_n\,|n\rangle$. The atom-field interaction is represented by

$$H_I = -x_{10}\,E(t)\,(|1\rangle\langle 0| + |0\rangle\langle 1|)\,, \tag{4.24}$$

x_{10} being the matrix element $\langle 1|\,\mathbf{x}\,|0\rangle$. The dipole moment and acceleration operators are given respectively by

$$\mathbf{x}_{TL} = x_{10}\,(|1\rangle\,\langle 0| + |0\rangle\,\langle 1|) \tag{4.25}$$

and

$$\ddot{\mathbf{x}}_{TL} = -\omega_{10}^2\mathbf{x}_{TL} + 2\omega_{10}\,x_{10}^2\,E(t)\,(|0\rangle\,\langle 0| - |1\rangle\,\langle 1|)\,, \tag{4.26}$$

with the energy difference $\omega_{10} = \varepsilon_1 - \varepsilon_0$. The amplitudes $C_n(t)$ are the solution of the following system of coupled differential equations

$$i\frac{d}{dt}\begin{pmatrix} C_0 \\ C_1 \end{pmatrix} = \begin{pmatrix} \varepsilon_0 & x_{10}E(t) \\ x_{10}E(t) & \varepsilon_1 \end{pmatrix}\begin{pmatrix} C_0 \\ C_1 \end{pmatrix}. \tag{4.27}$$

Introducing now ionization [44, 72], we choose an atom with a ground state in the tunneling ionization regime and the excited state in the over-the-barrier ionization regime, with time-dependent ionization rates respectively $\gamma_0(t)$ and $\gamma_1(t)$. The ground-state ionization rate was chosen as the quasi-static tunneling formula [66] for the one-dimensional case

$$\gamma_0(t) = D_1\ \exp(-D_2/|E(t)|), \tag{4.28}$$

where D_1 and D_2 are positive real parameters (see Appendix C for the derivation of this formula). For the excited state we took

$$\gamma_1(t) = D_3\ \exp(-D_4/|E(t)|^2), \tag{4.29}$$

where D_3 and D_4 are adapted as discussed in Sec. 6.2.1. The equations (4.27) will now be solved with the energies ε_n replaced by the complex quantities $\tilde{\varepsilon_n} = \varepsilon_n - i\gamma_n(t)/2$. The energies of the time-dependent dressed states are obtained by diagonalizing the Hamiltonian (4.22). The instantaneous transition frequency between these dressed levels is given by

$$\omega_{01D}(t) = \{[\varepsilon_0 - \varepsilon_1 - i(\gamma_0(t) - \gamma_1(t))/2)]^2 + 4x_{10}^2E(t)^2\}^{1/2}. \tag{4.30}$$

The cutoff frequency is the maximal value of $Re[\omega_{01D}(t)]$. For very high intensities, this cutoff is proportional to the Rabi frequency $\Omega_R = 2x_{10}E_0$. The energy width introduced by ionization in principle can cause an increase in the cutoff frequency. Furthermore, harmonics can be generated by the nonlinearity introduced by the functional forms of γ_0 and γ_1.

4.3 Fully numerical solution of the time-dependent Schrödinger equation

A third and widely used approach consists in solving the time-dependent Schrödinger equation (2.1) fully numerically (TDSE). Within the context of atoms in strong laser fields, this method was first used in the late seventies [47]. Since then, it has been applied to a wide range of strong-field optical phenomena, including high-harmonic generation [48, 49, 50]. The main advantage of the TDSE is that it encompasses *all* time-dependent physical effects arising from the time-propagation of the

Schrödinger Hamiltonian. Moreover, it can in principle be applied to an external field and binding potentials of arbitrary shape. Its main drawback is of practical nature: For quantitatively describing realistic systems, at least a two-dimensional computation must be performed[4]. This already involves considerable numerical efforts, and is extremely time-consuming. Furthermore, the multitude of coupled physical effects involved may sometimes be detrimental to the physical interpretation of a particular phenomenon.

Particularly concerning high-harmonic generation, this approach takes into account not only the physical mechanisms discussed in Sec. 4.1 and 4.2, but also effects like bound-state depletions, ionization and continuum-continuum transitions. Therefore, it will be taken as the full, "benchmark" solution in the subsequent Chapters of Part I, against which all other approaches will be tested. We solve the Schrödinger equation for a one-dimensional model atom in a time-dependent external laser field. The one-dimensional case is particularly interesting and widely used for modeling harmonic generation in linear polarization [50], since it requires much less computer time than three-dimensional computations, being therefore amenable to an expedient, yet accurate numerical solution.

We consider an "atom" in a box of length L, with arbitrary potential $V(x)$. In all computations presented in this thesis involving the TDSE, we take as initial condition the atom in the ground state, i.e., $|\psi(t=0)\rangle = |0\rangle$. The initial atomic wave function is calculated fully numerically using the inverse iteration method. The time-propagation is performed in the velocity gauge, using the standard finite-difference Crank-Nicolson method. The time-dependent Hamiltonian is

$$H = \frac{\mathbf{p}^2}{2} - \mathbf{p}\, A(t) + V(\mathbf{x}), \tag{4.31}$$

obtained from the velocity-gauge Hamiltonian $H_v^S(t)$ of Sec. 2.1 through the unitary transformation (2.13), $\mathcal{A}_{\vec{v}\leftarrow v} = \exp[-i\int A^2(t)dt]$. In order to minimize numerical transient effects, the vector potential $A(t)$ must be switched on smoothly. An important technical detail concerns the reflection of the time-dependent wave function $|\psi(t)\rangle$ on two hard walls at the edges of the box, artificially introduced by its finite size. These reflections may lead to unphysical effects, as for instance spurious high-frequency harmonics, and therefore must be minimized. This can be done by:

1. Choosing the box several times larger than the classical excursion length of the electron wave packet in the continuum, defined as the time average $\alpha_0 = \langle F(t)\rangle$, $F(t)$ defined in Sec. 4.1.1. This way we assure that just very little of the propagating wave packet will reach the boundary.

2. Introducing a function close to the boundaries, which "absorbs" part of the reflecting wave function. In our calculation, we multiply $|\psi(t)\rangle$ by a mask function $f(x)$, introduced from an arbitrary point $x = x_0$ until $x = L$, such that $f(\pm L) = 0$ and $f(\pm x_0) = 1$. In all simulations presented in Part I, we take

$$f(x) = \begin{cases} 1, & |x| < |x_0| \\ \cos^4\left[\frac{\pi}{2}\left(\frac{x-x_0}{L-x_0}\right)\right], & |x| > |x_0| \end{cases}, \tag{4.32}$$

which, for our parameters, has proven to yield the best results.

Specifically for calculating harmonic spectra, the above-stated conditions sometimes are not enough to prevent spurious effects. In this case, one must additionally take the dipole acceleration

[4] For linearly and circularly polarized light, this is possible using symmetry properties of the electric field and atomic potential. For elliptically polarized light, however, the whole 3D problem must be solved.

$\ddot{x}(t) = \langle\psi(t)|\,\ddot{\mathbf{x}}\,|\psi(t)\rangle$ instead of the dipole length $x(t) = \langle\psi(t)|\,\mathbf{x}\,|\psi(t)\rangle$. The dipole acceleration operator is calculated using Ehrenfest's theorem [73, 74], and is given by

$$\ddot{\mathbf{x}} = -\frac{dV(\mathbf{x})}{dx} + E(t). \tag{4.33}$$

The equation above already provides some information about the high harmonics: the second term on the right-hand side of (4.33) only contributes to the fundamental, since it oscillates with the field frequency. The high harmonics are originated by the quantum average of the operator $-dV(\mathbf{x})/dx$.

For the dipole length, TDSE computations yield the appearance of a large background and spurious high-frequency harmonics, as intense as those of the plateau, provided there is appreciable ionization. A simple argument concerning the appearance of this background, which we will briefly recall, was presented in [73]: Let us consider a time-dependent dipole moment, induced by an external field switched on and off at respectively $t = 0$ and $t = \tau$. The Fourier transform of the dipole length and acceleration are related by

$$\int_0^\tau \ddot{x}(t)\exp[-i\omega t]\,dt = [\dot{x}(\tau) - i\omega x(\tau)]\exp[-i\omega\tau] - \omega^2\int_0^\tau x(t)\exp[-i\omega t]\,dt, \tag{4.34}$$

with $x(0) = \dot{x}(0) = 0$. The first term on the right hand side of (4.34) is responsible for the background observed. This term is particularly large in case there is significant ionization, since this implies large $\dot{x}(\tau)$ and $x(\tau)$. Otherwise, it is negligible and the power spectra of the dipole length and acceleration are equivalent, apart from a factor ω^4. A detailed investigation of this background based on the TDSE also suggested that it might be related to the influence of excited bound states on HHG [74].

The generation of spurious harmonics for the $x(t)$ spectra is the consequence of the reflection of the time-dependent wave function at the boundaries. Their absence for the power spectra of $\ddot{x}(t)$ is very easily explained: The dipole acceleration weights the time-dependent wave function in such a way that the contributions of $\langle\psi(t)|\,\ddot{\mathbf{x}}\,|\psi(t)\rangle$ from points far away from the atomic core are negligible. For instance, for a one-dimensional soft Coulomb potential $V(x) = -\alpha/\sqrt{(x/\beta)^2+1}$, which is extensively used in the literature, the dipole acceleration according to (4.33) is given by

$$\langle\psi(t)|\,\ddot{\mathbf{x}}\,|\psi(t)\rangle \sim \langle\psi(t)|\frac{\mathbf{x}}{[(\mathbf{x}/\beta)^2+1]^{3/2}}|\psi(t)\rangle + E(t). \tag{4.35}$$

For short-range potentials, the corresponding matrix element decays even more rapidly with the coordinate x.

4.4 Time-frequency analysis

One can determine in which frequency an atom responds to an external laser field by taking the modulus squared of the Fourier transform of the time-dependent induced atomic dipole. However, by calculating the power spectra, all the temporal information about harmonic generation is lost. Certain features of harmonic generation, which yield considerable information on its physical mechanisms, such as the semiclassical return times in the three-step model [54], or the time-dependent level crossings in the two-level atom [46, 56], can only be revealed by a time-frequency or wavelet analysis.

This theoretical method has been first proposed by Gabor in 1946 [75] and has been extended and generalized by innumerous groups in the subsequent decades. Since then, it has been used in several fields of research, as diverse as for instance image processing, acoustical phenomena, or medicine [76, 77]. Particularly with respect to high-intensity optical phenomena, several groups [52, 53, 55, 56,

57] have employed time-resolved spectra for analyzing the time-dependence of harmonic generation. These spectra are obtained by performing a Fourier transform with a temporally restricted envelope[5], defined, for an arbitrary function $f(t)$, as

$$\mathcal{W}(t,\Omega,\sigma) = \int_{-\infty}^{+\infty} dt'\, f(t')\, W(t,t',\Omega,\sigma). \tag{4.36}$$

In (4.36), σ and Ω denote respectively the time width and the center of the window function. These parameters, as well as the shape of the window function $W(t,t',\Omega,\sigma)$ must be chosen according to the problem at hand [77]. Clearly, by introducing time resolution, as a direct consequence of the uncertainty principle[6] we lose frequency information. The frequency width σ_ω of the window function can be found by performing its Fourier transform, and is related to σ by

$$\sigma_\omega \sigma \geq 1/2. \tag{4.37}$$

In the subsequent chapters of this thesis, we perform a wavelet transform with a Gaussian window function (Gabor transform), which is given by

$$W_G(t,t',\Omega,\sigma) = \exp[-(t-t')^2/\sigma^2]\, \exp[-i\Omega t'] \,, \tag{4.38}$$

of width σ and centered at a harmonic frequency $\Omega = N\omega$. For this choice of window function, the temporal width σ corresponds to a frequency bandwidth $\sigma_\omega = 2/\sigma$. The usual Fourier transform, in which all temporal information is lost, is obtained for $\sigma \to \infty$.

We choose the time width of the window function narrower than a period of the external laser field. The center of the window function is then "moved" in time such that at least one period of the laser field is taken into account. The Gabor yield, given by

$$\mathcal{G}_Y = |\mathcal{W}(t,\Omega,\sigma)|^2 \,, \tag{4.39}$$

is then calculated for each timestep within this interval. In this way the contribution from a particular group of harmonics to the emitted radiation can be determined as peaks in the time-dependent spectra. This procedure differs slightly from the time-frequency analysis performed by most groups [52, 53], which take this width larger than the laser period T in order to investigate the time profile of a single specific harmonic.

In principle, the harmonic generation process is almost periodic, with the period of the driving laser frequency, or with half this period, depending on the field in question[7]. For instance, within the three-step model framework, for a monochromatic field, one expects, in the cutoff region, a single peak at $t_1 = 0.95\ T \mod T/2$. At the end of the plateau, this peak splits into two, as discussed in Sec. (4.1.2), corresponding to a shorter and longer return times. Depending on the time width σ, these substructures may or may not be resolved. This is illustrated in Fig. 4.6, where the return times predicted by the three-step model as functions of $E_{\rm kin}\,(t_1,t_0)$ are shown, together with the time-frequency regions delimited by the generic window functions W_1 and W_2. The window function W_1, for instance, can not resolve the splitting of the cutoff return times, but includes harmonics only in the cutoff region. Only in regions where the two return times are further apart, i.e., for

[5] Some authors adopt a more restrictive definition of wavelet according to the time resolution of the window function, which must be variable in order to contain a constant number of oscillations [76].

[6] This principle states that the energy spread of a function and its Fourier transform can not be simultaneously arbitrarily small.

[7] For instance, for monochromatic fields and bichromatic fields consisting of a monochromatic driving wave and its (2n+1)-th harmonic, this periodicity is reduced to $T/2$.

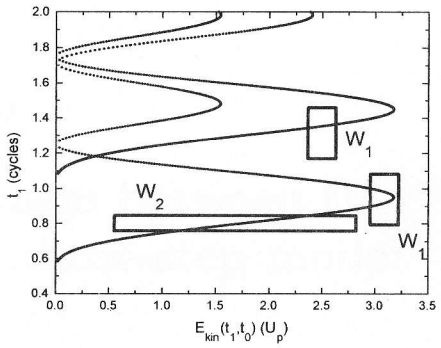

Figure 4.6: Areas defined in the time-frequency plane by the window functions W_1 and W_2, together with the returning times t_1 as functions of the kinetic energy $E_{\rm kin}(t_1,t_0)$ predicted by the three-step model for an electron in a monochromatic field. We give t_1 in terms of the field cycle T, such that $t_1 \leq 2T$, and $E_{\rm kin}(t_1,t_0)$ in terms of the ponderomotive energy. W_1 is shown in the cutoff and high plateau frequency region.

lower harmonic frequencies, this would be possible. Another possibility is using W_2, but then a much broader frequency range is taken into account. In fact, for this latter window function, one has a much complex pattern for the time-resolved spectra than the two return times seen in Fig. 4.6. This is clear, since the semiclassical trajectories corresponding to this whole frequency region strongly interfere. Moreover, longer return times may also contribute to the Gabor yield. However, due to wave packet spreading, the peaks corresponding to these trajectories are not expected to be prominent in the time profile.

In the results that follow, sometimes the wavelet yield is only *approximately* periodic in T or $T/2$. This is related to effects, such as, for instance, turn-on transients and ionization. This is the case for the fully numerical solution of the Schrödinger equation and, in Subsec. 6.2.1, for the two-level atom with ionization.

Chapter 5

Comparison between the TDSE and the three-step model

According to the three-step model, the main contributions to HHG within a field cycle correspond to the semiclassical return times of an electron to its parent ion. Concerning the plateau and cutoff harmonics, this model yields clear predictions related to the time profile of HHG:

- At the cutoff, a *single* return time for the recombining electron is present.
- At the end of the plateau, this return time splits into two, corresponding to a longer and a shorter excursion time for the electron in the continuum, denoted respectively by τ_2 and τ_1.
- For the plateau as a whole, there are several possible trajectories for the returning electron, but the ones related to τ_2 and τ_1 are dominant. As the harmonic energy decreases, these return times get further and further apart.

These features can be clearly seen in Figs. 4.4 and 4.6, and were investigated in detail within the three-step physical picture using a time-frequency analysis by Antoine et al. [54]. Clearly, if the above-stated temporal behavior can be extracted from both the three-step model and the fully numerical solution of the Schrödinger equation, the same physical mechanisms are responsible for HHG in both models. This comparison, using the Gabor transform discussed in Sec. 4.4, is the main concern of this Chapter (see also [55]). In this investigation, we used, as numerical methods, the Crank-Nicolson scheme and the six-point integration, both discussed in Appendix D.

We test the quantum-mechanical three step model against a one-dimensional TDSE computation, considering a monochromatic field (4.8) of angular frequency $\omega = 0.05$ and amplitude $E_0 = 0.08$. The corresponding vector potential is turned on smoothly within two cycles of the driving field. For both models, we calculate the wavelet yield of the dipole acceleration $\ddot{x}(t)$.

For the fully numerical time-dependent computation, we consider a short-range potential of the form

$$V(x) = -0.76 \exp(-x^2/1.76), \tag{5.1}$$

with a single field-free bound state, denoted $|0\rangle$, at energy $\varepsilon_0 = -0.401$. Thus, we exclude any possible influence of the excited bound states in the process, concentrating on the ground-state-continuum transitions, and expect a negligible influence of $V(x)$, as soon as the electron is outside the range of the potential. This potential choice is therefore a very adequate test case for the

three-step model (see approximations 1-3 in Subsec. 4.1.2). Within this latter framework, for the monochromatic field (4.8), the stationary action (4.16) is given by

$$S_{\rm st}(t,\tau) = \tau|\varepsilon_0| - \frac{\tau}{2}p_{\rm st}^2(t,\tau) + \frac{1}{2}\int_{t-\tau}^{t} dt' A^2(t'), \tag{5.2}$$

while the stationary momentum (4.17) is given by

$$p_{\rm st}(t,\tau) = \frac{E_0}{\omega^2\tau}\left[\sin(\omega t) - \sin(\omega t - \omega\tau)\right]. \tag{5.3}$$

In equations (5.2) and (5.3), with respect to Subsec. 4.1.2, we introduced the change of variable $\tau = t - t_0$ (not to be confused with the pulse length τ used in the previous chapters), which yields the electron excursion time. These expressions are then inserted in (4.18), which gives the time-dependent dipole moment for the three-step model, within the stationary phase approximation. Equation (4.18) has a clear physical interpretation: the dipole at time t receives contributions from all trajectories that started at the origin a time τ earlier, "picked up" the action $S_{\rm st}$ and returned to the origin at t, which for a free classical evolution is possible only for a definite average momentum, $p_{\rm st}$.

In order to compute the Gabor transform of the dipole acceleration from the three-step model dipole length $x(t)$, one must use the formula

$$\int dt\, \ddot{x}(t)\, W_G(t,t',\Omega,\sigma) = \int dt\, x(t)\, \ddot{W}_G(t,t',\Omega,\sigma), \tag{5.4}$$

where

$$\ddot{W}_G(t,t',\Omega,\sigma) = \{(-2/\sigma^2) + [i\Omega - 2(t-t')/\sigma^2]^2\} W_G(t,t',\Omega,\sigma), \tag{5.5}$$

$W_G(t,t',\Omega,\sigma)$ being defined in (4.38). This is obtained by partial integration, noting that W and its derivatives vanish at the integration endpoints.

Figure 5.1 presents the results from the time-frequency analysis over one cycle; we show the square of the magnitude of the Gabor transform of the dipole acceleration, for t' varying from $5.7\,T$ to $6.7\,T$. The dashed lines in the figure correspond to the results obtained using the three-step model [41], while the solid lines are the results of the fully numerical solution.

Peaks in the harmonic time-frequency spectrum $\mathcal{G}_Y$ arise from classical trajectories returning to the origin, leading to strong nonlinear response within the range of the potential. These classical return time peaks are clearly visible in the harmonic response centered on the cutoff harmonics ($\Omega = 49\,\omega$, $\sigma = 0.1\,T$), for both the TDSE and the three-step model, shown in part (a). This has been observed before in [52]. When more plateau harmonics are included, as in Fig. 5.1.b, ($\Omega = 45\,\omega$, $\sigma = 0.055\,T$) the single peak splits into two, whose temporal positions correspond approximately to the two (semi-) classical shortest return times, τ_1 and τ_2 (see Fig. 3 in [54] and Figs. 4.4 and 4.6 in this thesis). It is however apparent that the two peaks are farther apart for the full solution than for the three-step model. Furthermore, the τ_1-peak has gained additional substructure in the full solution.

When most of the plateau harmonics are included, in Fig. 5.1.c, there are still two dominant peaks; the "shortest classical return" peak (denoted by τ_1) is composed of many sub-peaks since many harmonics are included. In fact, the shorter return time varies more rapidly with harmonic energy. The return peak τ_2 is prominent in both sets of results. This is comparable to the case considered in [54], Fig. 2.

Our results show that the three-step model contains the essential physics leading to high-harmonic generation in a linearly polarized laser field. The multiple peak structure of [54] is reproduced in

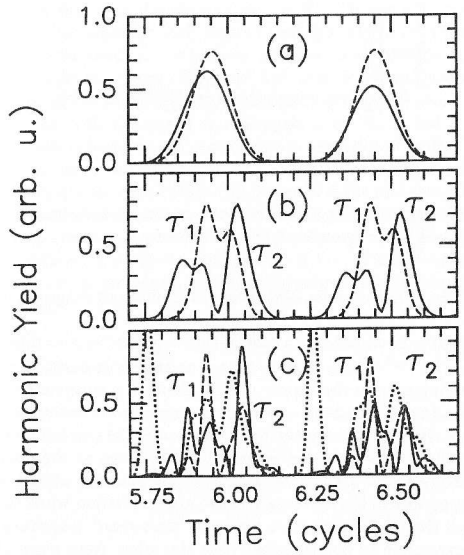

Figure 5.1: Wavelet analysis of the time-dependent dipole acceleration over one cycle of the driving laser field. Part (a): $\Omega = 49\ \omega$, $\sigma = 0.1\,T$; Part (b) : $\Omega = 45\ \omega$, $\sigma = 0.055\,T$; Part (c) : $\Omega = 37\ \omega$, $\sigma = 0.024\,T$. Solid line : full time-dependent (TDSE) solution, dashed line : three-step model [41, 54] with gaussian dipole approximation, dotted line (only in part (c)) : three-step model with exact dipole matrix element.

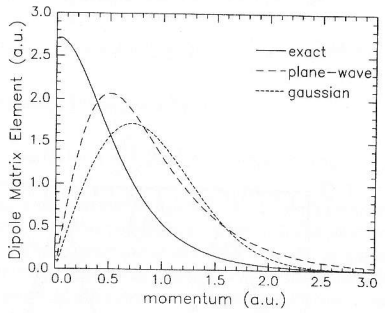

Figure 5.2: Dipole matrix elements $d_x(p)$. Dotted line : exact; dashed line : plane-wave continuum approximation; short-dashed line : "gaussian" approximation.

qualitatively similar fashion in both results, with peaks at similar positions and of similar magnitude.

However, the agreement is good only for a special choice of the "atomic dipole" function $d_x(p) = \langle p|\, x\, |0\rangle$, namely $d_x(p) \sim pe^{-\alpha p^2}$, with $\alpha = 1$, shown as the short-dashed line in Fig. 5.2. This "gaussian dipole" approximation to the dipole matrix element corresponds to a gaussian ground state wave function in position-space and plane-wave continuum wave functions. If we take for $d_x(p)$ the "exact" dipole matrix element between the bound state and the continuum state at energy $p^2/2$, calculated fully numerically for the gaussian potential (5.1), (given as the dotted line in Fig. 5.2) we obtain the dotted line in figure 5.1.c, exhibiting a strong spurious peak near $E(t) = E_0$. This spurious peak appears generally in the stationary phase approximation when the width (in p-space) of $d_x(p)$ is made so small that the contribution near the "zero-time" trajectory is strongly peaked: physically this would correspond to contributions near the origin from parts of the wave function that are being 'accelerated' by the field within the range of the potential. It is evident from the fully numerical solution (solid line) that this is not an important mechanism of harmonic generation in the present case. Furthermore, for such a peaked $d_x(p)$, the stationary phase approximation starts to become invalid.

In the actual physical process of high-harmonic generation at low laser frequency the "rescattering" wave packet appears through a tunnel ionization process and thus it is not astonishing that the modeling through a dipole matrix element is not adequate. On the other hand, for the second interaction in equation (4.18), which "generates the harmonics", the dipole matrix element should be quite appropriate.

Our time-profile from the full solution is only approximately symmetric under a shift of $0.5\,T$. This is clear since in our full time-dependent case there is strong ionization and thus the dipole moment decays in time, in addition to other explicitly time-dependent effects. Finally, although we are probing the harmonic response over times shorter than the laser field period, the harmonic generation process must happen over several cycles of the laser field in a quasi-periodic fashion [78]. In fact, when calculating the time profile of *a single* harmonic, one must take a window function several times larger than the period of the driving field [53]. The mathematical reason for this choice

has already been discussed in Sec. 4.4.

Concluding, the general plateau harmonic generation spectra, with the expected cutoff energy at $\epsilon_{max} = |\epsilon_0| + 3.17U_p$, are reproduced by a wide variety of choices of the matrix element $d_x(p)$ within the three-step model framework. But the time-dependence of the harmonic generation is a much more differential and thus sensitive measure, in which not simply the magnitudes but the relative phases of all contributing harmonics are involved. When only cutoff harmonics are involved, as shown in Fig. 5.1.a, the time of harmonic generation is just 0.45 and 0.95 in units of the laser period, that is, just before the field minimum. This result again is not very sensitive towards changes in $d_x(p)$: most choices for the dipole matrix element correctly predict the time-dependence of the *cutoff* harmonics. Both results are in agreement with the observations in [41, 54] concerning the independence of the cutoff spectral and temporal behavior with respect to $d_x(p)$. However, when more and more of the *plateau* harmonics are superposed, a much more complex time-behavior emerges, which this time depends on the matrix element chosen. From the full time-dependent solution, it is clear that the three-step picture which predicts two dominant shortest return time peaks is qualitatively correct, as shown by the solid line with the peaks τ_1 and τ_2 in Figs. 5.1.b and c. The exact shapes and substructure of these peaks is however not quantitatively reproduced by the three-step model. First, we found that a spurious peak can appear at $E(t) = E_0$ when $d_x(p)$ is chosen too peaked in the three-step model. Second, the shortest-return time τ_1 peak splits into several peaks with comparable magnitude. The three-step model indicates that one of these is dominant, which is not the case in the full solution. Third, the longer-return time τ_2 peak is narrower in the full solution. Despite these quantitative differences, the results obtained with the TDSE computation can be traced to the semiclassical return times predicted by the three-step model, strongly suggesting a common mechanism for HHG in both cases.

Chapter 6

Influence of excited bound states on high-harmonic generation

The three-step model and the two-level atom describe HHG as a result of completely different physical mechanisms: the former states that this phenomenon is due to free-bound transitions of an electronic wave packet, whereas the latter relates HHG to bound-bound transitions. In the previous chapter (see also [55]), we considered the case of an atom with a *single* bound state. We used time-frequency analysis in order to compare the fully time-dependent solution of the Schrödinger equation with the three-step model [41]. The time profiles of the plateau and cutoff harmonics were qualitatively similar for both models, corresponding to the semiclassical return times for the electronic wave packet. However, for an atom with more than one field-free bound state, such a coincidence is not always observed, especially for the lower order plateau harmonics.

Therefore, in the present chapter, we address the question of whether the two pictures of rescattering and bound-level transitions can be compatible and what are their respective ranges of applicability concerning harmonic generation, for atoms with several bound states. The goal of these studies is to gain some insight in the process of generation of harmonics when several bound states are involved, and to include information about the complementary temporal structure of the harmonics, with the eventual aim of being able to control this emission for tailoring harmonic pulses of desired characteristics. For that purpose, one needs of course to consider further computations of the propagation of harmonic radiation, for which the two-level atom, TDSE or three-step model may provide the initial conditions [22].

Again, we base our discussion on the fully numerical solution of the time-dependent Schrödinger equation. This approach includes all bound-bound, bound-continuum and continuum-continuum transitions, thus incorporating time-dependent effects like ground- and excited-state depletion, ionization and recombination. Therefore, as a first step we must define and isolate the different mechanisms and investigate their contribution to harmonic generation. To first approximation, we project the time-dependent wave function onto the field-free bound states, the remainder being an effective time-dependent continuum. Using spectral and time-frequency analysis, we perform a detailed investigation of the radiation emitted by the atom. The case of a system with two bound states and a continuum is analyzed in detail and compared with a two-level atom model. A particular motivation for this specific analysis lies in a recent work, in which the inclusion of a "three-step-like" recombination mechanism in the bound-state populations of a two-level atom was able to reproduce a plateau and sharp cutoff at $\omega_{10} + 3.17\, U_p$, where $\varepsilon_1 - \varepsilon_0 = \omega_{10}$ is the energy difference between the bound states [45]. The "bound-bound transitions" from the TDSE include such recombination mechanisms. Furthermore, we consider ionizing bound-state populations in the two-level atom

model. Recent studies have shown that this procedure may prolong the plateau in the harmonic spectra, depending on the functional forms of the ionization rates [44] (see also discussion in Sec. 4.2). Therein, a similar rate as in Sec. 4.2 (i.e., Eq.(4.28)) and a step function were used for, respectively, the ground- and excited-state populations.

The Chapter is organized as follows: in the next section, we discuss a theoretical projection method, which is used to isolate different "classes" of transitions from the TDSE solution. In Sec. 6.2, we have taken several model potentials to investigate: two bound states in a short range potential (Subsec. 6.2.1), one deeply bound and many weakly bound states in a long-range (soft Coulomb) potential (Subsec. 6.2.2), several deeply bound (and many weakly bound) states in a deep soft-Coulomb potential (Subsec. 6.2.3), and the same potential as in Subsec. 6.2.3, but with its Coulomb tails cut off (Subsec. 6.2.4). In Sec. 6.3 we state our conclusions.

6.1 Fully time-dependent projections

The time-dependent wave function $|\psi(t)\rangle$ from the TDSE computation (Sec. (4.3)) can be expanded into the field-free-bound-state basis

$$|\psi(t)\rangle = \sum_n C_n(t)|n\rangle + |\phi_c(t)\rangle, \tag{6.1}$$

where the bound states are denoted by $|n\rangle$, the remaining continuum part of the wave function by $|\phi_c(t)\rangle$ and $C_n(t) = \langle n|\psi(t)\rangle$. These time-dependent amplitudes are calculated fully numerically. The advantage of taking such a basis concerns the orthogonality between the bound states and the continuum. In case this property is not fulfilled, the computation of the amplitudes $C_n(t)$ is not straightforward.. We took as initial condition the atom in the ground state, i.e., $|\psi(t=0)\rangle = |0\rangle$. The average dipole acceleration $\ddot{x}(t) = \langle\psi(t)|\,\ddot{\mathbf{x}}\,|\psi(t)\rangle$ can therefore be split into

$$\langle\psi(t)|\,\ddot{\mathbf{x}}\,|\psi(t)\rangle = \ddot{x}_{bb}(t) + \ddot{x}_{bc}(t) + \ddot{x}_{cc}(t). \tag{6.2}$$

Inserting the expression for $\ddot{x}(t)$ given by Ehrenfest's theorem (Eq. (4.33)) in (6.2) , the bound-bound, bound-continuum and continuum-continuum contributions are written as respectively

$$\ddot{x}_{bb}(t) = \sum_{n,m} C_m^*(t)C_n(t)\langle m\left|\frac{-dV(\mathbf{x})}{dx}\right|n\rangle + E(t)\sum_n |C_n(t)|^2 \quad , \tag{6.3}$$

$$\ddot{x}_{bc}(t) = \sum_n 2Re\left[C_n(t)\langle\phi_c(t)\left|\frac{-dV(\mathbf{x})}{dx}\right|n\rangle\right] \tag{6.4}$$

and

$$\ddot{x}_{cc}(t) = \left\langle\phi_c(t)|\frac{-dV(\mathbf{x})}{dx} + E(t)|\phi_c(t)\right\rangle. \tag{6.5}$$

As discussed in Sec. 4.3, the $E(t)$ term in (4.33) contributes only to an enhancement in the fundamental in the spectrum of the full acceleration. However, for the bound-bound and continuum-continuum contributions (6.3) and (6.5), there is the introduction of an extra time-dependence in this term, coming from the bound-state and continuum populations[1]. This term does however not introduce any important contributions, as will be shown in Sec. 6.2.

We perform the decomposition (6.1) taking the time-dependent wave function both in the velocity and in the length gauge. For the length gauge wave function, we apply the unitary transformation

[1] Adding (6.3) and (6.5), since $\sum_n |C_n(t)|^2 + < \phi_c(t)|\phi_c(t) >= 1$, this extra time-dependence disappears.

$\mathcal{A}_{l\leftarrow v} = e^{-ixA(t)}$ on $|\psi(t)\rangle$ after each step of the time propagation. In both cases, we use the *same* time-independent states $|n\rangle$ calculated for the field-free atomic Hamiltonian. This approach is widely used in the literature and is well-known as a "hybrid procedure" [79]. One should keep in mind, however, that through keeping the field-free eigenstates, one breaks the gauge invariance for each isolated projection [80]. Only for the full acceleration, $\ddot{x}(t)$, this property is maintained. In order to keep the gauge equivalence for the projections $\ddot{x}_{bb}(t)$, $\ddot{x}_{bc}(t)$, and $\ddot{x}_{cc}(t)$, it is necessary to perform the same unitary transformation also on $|n\rangle$, such that changing from a representation (μ) to a representation (ν), one would have time-dependent states for one of the representations, according to $|n_{(\nu)}(t)\rangle = \mathcal{A}_{\nu\leftarrow\mu}|n_{(\mu)}\rangle$. Using the hybrid procedure, one obtains, instead, for the amplitudes $C_n(t)$ in the different representations,

$$C_{n(\nu)}(t) = \sum_{j=0}^{n} \langle n|\,\mathcal{A}_{\nu\leftarrow\mu}\,|j\rangle\, C_{j(\mu)}(t) + \langle n|\,\mathcal{A}_{\nu\leftarrow\mu}\left|\phi_{c(\mu)}(t)\right\rangle \ , \tag{6.6}$$

with the continuum being

$$\left|\phi_{c(\nu)}(t)\right\rangle = |\psi_{(\nu)}(t)\rangle - \sum_n C_{n(\nu)}(t)|n\rangle \quad . \tag{6.7}$$

The choice of gauge for which the field-free bound state basis yields physically reasonable results, as well as a justification for that choice, is a highly controversial issue. There are two main arguments in the literature in favor of using bare bound states in the length gauge: The picture of the quasi-static distorted potential considered in Sec. 4.1, which is used in the physical description of the three-step model, corresponds to the length gauge Hamiltonian. Thus, as a first approximation, one should do the projections on the undistorted bound states in the length gauge [81, 82]. Another argument uses the fact that the *mechanical* momentum Π and not the canonical momentum p is a physical observable [83]. In the absence of the field and in the length gauge, such quantities coincide. In the velocity gauge, however, they are related by $\Pi = p - A(t)$. According to several authors, this discrepancy is responsible for unphysical results projecting onto the eigenstates of the field-free Hamiltonian in the velocity gauge, H_v^A [79].

Even though the arguments above are not completely agreed upon, we could in fact observe unphysical behavior for the amplitudes $C_n(t)$ using field-free bound states in the velocity gauge. The misleading results obtained using the velocity gauge are presented and discussed in Subsec. 6.2.5. Obviously, the expansion into a *field-free* bound-state basis yields just an approximate picture for the bound-state subspace, since in a real atom the higher excited bound states are strongly distorted by the field and coupled to the continuum. Moreover, the projections $\langle\psi(t)|n\rangle\langle n|\,\ddot{\mathbf{x}}\,|m\rangle\langle m|\psi(t)\rangle$ are *not* equivalent to the respective second temporal derivatives of the dipole length projections, $d^2\langle\psi(t)|n\rangle\langle n|\mathbf{x}|m\rangle\langle m|\psi(t)\rangle/dt^2$, since the projection operators $|n\rangle\langle n|$ do not commute with the full Hamiltonian (4.31). Therefore, for an atom with two bound states, a direct comparison between $\ddot{x}_{bb}(t)$ of Eq. (6.3) and the dipole acceleration of a two-level atom is questionable. This error is not introduced if we compare the bound-bound projections and the two-level atom dipole in the length form, used as a test in Subsec. 6.2.1.

Just as for the time dependent dipole, one can split the time-dependent power spectra discussed in Sec. 4.4 into the corresponding bound-bound, bound-continuum and continuum-continuum contributions. We thus obtain the wavelet transform of the dipole acceleration (6.2) and its projections,

$$\begin{aligned}|\mathcal{W}(t,\Omega,\sigma)|^2 \;=\; & |\mathcal{W}_{bb}(t,\Omega,\sigma)|^2 + |\mathcal{W}_{bc}(t,\Omega,\sigma)|^2 + |\mathcal{W}_{cc}(t,\Omega,\sigma)|^2 \\ & +2\,Re\{\mathcal{W}_{bb}(t,\Omega,\sigma)\mathcal{W}_{bc}^*(t,\Omega,\sigma) + \mathcal{W}_{bc}(t,\Omega,\sigma)\mathcal{W}_{cc}^*(t,\Omega,\sigma) \\ & +\mathcal{W}_{bb}(t,\Omega,\sigma)\mathcal{W}_{cc}^*(t,\Omega,\sigma)\},\end{aligned} \tag{6.8}$$

where not only the separate contributions but also their relative phases play an important role, since there are crossed terms.

6.2 Results

6.2.1 Short-range potential

In order to test the two-level atom against the fully time-dependent solution of the Schrödinger equation, we chose a Gaussian short-range potential

$$V_G(x) = -0.76\exp(-x^2/4). \tag{6.9}$$

This potential supports two field-free bound states, at $\varepsilon_0 = -0.499$ a.u. and $\varepsilon_1 = -0.099$ a.u. We consider an external field of frequency $\omega_L = 0.05$ a.u. and amplitude $E_0 = 0.08$ a.u., which is clearly in the tunneling regime for the ground state. These conditions are comparable to the ones considered in [44], i.e., ground state in the tunneling regime, excited state in the over-the-barrier regime and dipole matrix element $\langle 0|x|1\rangle = 1.066$ a.u. According to the three-step models, the expected cutoff for the present case should be at $\Omega = 49\ \omega_L$, which is in very good agreement with the spectrum for the full acceleration, shown as the dotted line in Fig. 6.1. In fact, the dotted line beyond the harmonic 21 superposes exactly on the solid line, which gives only the bound-continuum part of the spectrum, resulting from $\ddot{x}_{bc}\,(t)$, Eq. (6.4). At low energy the bound-continuum part underestimates the full results, while the bound-bound part gives the dominant contribution. The bound-bound spectrum presents a completely different cutoff (at roughly $\Omega = 35\ \omega_L$) and no clear indication of a plateau, in contrast to the full dipole acceleration. An interesting feature of the bound-bound spectrum is a pronounced increase in the harmonic intensity, a so-called "low-energy hump" around the 7th harmonic, which resembles the features observed for molecular HHG spectra [24, 25]. This resemblance is related to a common harmonic generation mechanism, which will be discussed further in this subsection.

In order to verify whether these features correspond to a two-level atom, we compare the bound-bound part with the corresponding two-level atom, with and without ionization. We solved the Bloch equations (4.27) numerically using a standard fourth-order Runge-Kutta method (see Appendix D for a discussion of this method). The resulting time-dependent amplitudes $C_n(t)$ are then inserted in the two-level dipole acceleration, Eq. (4.26), from which the power spectra are calculated. Without taking ionization into account, we do not observe a plateau structure at all in the emission spectra for the field parameters above. In fact, the only peaks observed correspond to the fundamental, a few very weak harmonics (up to the 5th) and the resonance peak around the transition $|0\rangle \rightarrow |1\rangle$. Harmonic spectra with an extended plateau structure are only observed for much higher intensities, where any real atom would ionize practically instantaneously and the two-level atom description is unrealistic. These results are not shown in the figure.

As a further step, we introduce ionization rates for the bound-state populations as stated in Sec. 4.2. The tunnel formula for the ground state yields $D_1 = 0.72$ and $D_2 = 0.665$ in (4.28). For the excited state we choose $D_3 = 0.05$ and $D_4 = 0.0026$ in (4.29). The harmonic spectrum obtained in this case is very different from the full solution spectrum or from the bound-bound part of the full solution. Harmonics up to the 9th are visible, which is in agreement with the instantaneous two-level transition frequency (4.30), but these harmonics are much weaker than those of the full result. We conclude that the driven two-level atom is not a good model for computing the harmonic response, not even for the low harmonics which can be extracted as the bound-bound part of the spectrum. A strongly nonlinear ionization rate within the two-level atom model can enhance the harmonics and prolong the plateau, but then the field-dependent ionization rate does not reproduce the full solution's time dependence for the populations of the bound states, obtained by the time dependent projection onto the unperturbed states, shown in Fig. 6.2. Actually, the rate $\gamma_1(E(t))$ of Eq. (4.29) for the excited state is just an ad-hoc adjusted quantity since a tunnel formula is not too appropriate for this state whose binding energy $\varepsilon_1 = -0.099$ a.u. is only $2\hbar\omega_L$. Choosing a step

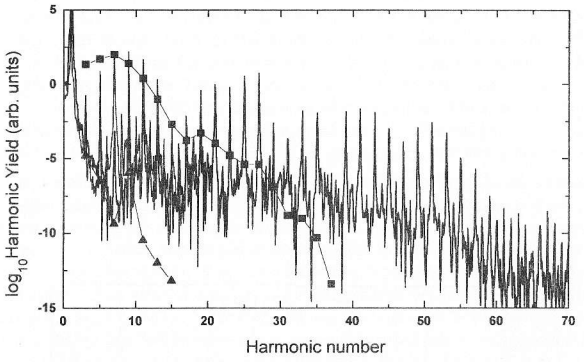

Figure 6.1: Power spectra for the short-range Gaussian potential (6.9) and its two-level atom model. Dotted line: full acceleration; solid line: bound-continuum part; squares: bound-bound part; triangles: two-level atom including ionization (for the latter two, only the harmonic peak heights are shown, connected by a thin line)

function as a model of the over-the-barrier ionization process yields more harmonics since it is more nonlinear [44], but it is arguably less realistic.

The ground- and excited state populations depicted in 6.2 show reasonably similar behavior for the full solution and the two-level atom model. The excited-state population of the full solution is quasi-periodic in time, with a zero at the times for which the field is zero. There are small dips (after the second cycle) at the times for which the field is maximal. The small dips in the excited state population are mirrored by corresponding peaks in the ground state population These dips, which are absent in the two-level atom results, are an indication that a nonlinear process is taking place around the peak field intensity, which involves just the two bound states. Both the full and the two-level atom calculations contain irreversible ionization, partially over-the barrier ionization, the excited state having the function of an intermediate state between the ground state and the continuum, and partially tunneling ionization. It must be noted that, even though recombination is present in the bound state part of the time evolution for the full results, the bound-bound part of the spectrum in Fig. 6.1 does not exhibit the cutoff at $\omega_{10} + 3.17\ U_p$ observed by [45].

The Gabor transform allows a more detailed analysis of the harmonic generation process. In Fig. 6.3, parts a to d, we present results obtained for low harmonics taking a time-width $\sigma = 0.1\ T$. In Fig. 6.3.a, we plot the wavelet transform for $\Omega = 7\ \omega_L$. In this case, the main contribution to harmonic generation within a field cycle for the full solution occurs close to the field peak. The full and the bound-bound contributions have very similar shapes, same amplitudes and coincident peaks. However, the bound-bound wavelet transform of the fully time-dependent computation and the two-level atom wavelet transform are remarkably different. The two-level atom results exhibit peaks at $t = 0.5\ T$ modulo $T/2$, that is, when the field $E(t)$ is zero. The full or the bound-bound results have also a small shoulder at $t = 0.5\ T$ mod $T/2$, but their main peak is 90° out of phase with

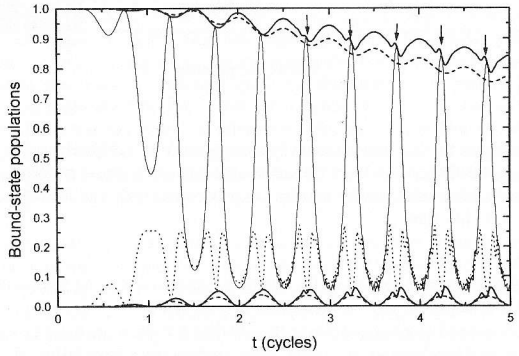

Figure 6.2: Bound-state populations. Solid heavy lines: full time-dependent computation for the short-range Gaussian potential. Dashed heavy lines: two-level atom with ionization. Solid and dotted light lines: full time-dependent calculation with projections in the velocity gauge. The upper curves are for the ground state, the lower ones for the excited state. The small dips related to the abrupt population transfer close to the field peak are marked with arrows.

the two-level-atom results, being at $t = 0.25\ T \bmod T/2$. In order to test whether this discrepancy is introduced by the fact that the projection operators onto the bare bound states do not commute with the full Hamiltonian (4.31), we performed the same calculation using the bound-bound projections and the two-level atom dipole, both in the *length* form; the result is shown in Fig. 6.3.b. The bound-bound contributions from the full solution in the length and acceleration forms in parts a and b exhibit peaks at the same times. This shows that the error introduced by the fact that $[|n\rangle\langle n|, H] \neq 0$ is of no qualitative importance in this situation. Once more, the two-level atom results in part b present peaks at times different from the x_{bb}. The shape and location of the peaks obtained for the two-level atom are not sensitive to variations in the ionization rates γ_0 and γ_1.

These results, together with the large difference in the magnitude of the harmonics, visible in Fig. 6.1, strongly suggest that the process of generation of these low harmonics must be quite different in the two cases, even though the full results are recovered in their two-bound-state projections. The generation of harmonics within the two-level-atom model has been investigated by Gauthey *et al.* [46] (See also Sec. 4.2 in this thesis). They conclude that harmonics occur due to a crossing between the two dressed states. The wavelet transform for the parameters used in [46] exhibits indeed well-localized sharp peaks at $t = 0.5\ T \bmod T/2$. In our present case however, the time-width of the avoided crossing between the two dressed levels becomes comparable to (although still smaller than) the laser field period and thus the peaks are no longer so sharp. For the full 1-D atom results, on the other hand, the field is driving the bound part of the electronic wave packet primarily within the two lowest bound states, as can be seen in Fig. 6.2 (the slow decrease in the ground-state population is due to irreversible ionization). Apart from a main oscillation, in which the bound part of the wave packet follows the field adiabatically, there is an abrupt population transfer between the two bound states close to peak field, arising from a "charge oscillation" of the wave packet between dipoles of opposite parity in the atom, seen as the small but sharp peaks in the TDSE populations, marked with arrows in Fig. 6.2. These peaks can be interpreted as follows. The anti-symmetrical wave function $\varphi_1 = \langle x\,|1\rangle$ is more concentrated at the edges of $V_G(x)$ and the symmetrical ground-state wave function $\varphi_0 = \langle x\,|0\rangle$ at its center. Thus, the overlap between the bound part of the wave function $\langle x\,|\psi_b(t)\rangle = C_0(t)\varphi_0 + C_1(t)\varphi_1$ and φ_1 (i.e., $C_1(t)$) decreases as the bound wave packet approaches $x = 0$. Simultaneously, its overlap with φ_0 increases. Subsequently, there is a sharp increase in $C_1(t)$ as the wave packet reaches the other side of the atom. It is only a small part of the wave packet that performs this motion, but this is the significant part producing the lower plateau harmonics. In fact, the time interval between the two small peaks in the excited-state population, of about 10 a.u., is roughly the time it takes for a classical particle to be taken from one "edge" of the atomic potential to the other (a distance of approximately 4 *a.u.*), with constant acceleration $a_{max} = E_0$. This mechanism is not taken into account in the two-level-atom model.

The same mechanism is present in the emission of harmonics from a diatomic molecule when considering the two lowest bound even- and odd-parity states [24, 25]. Intuitively, this charge oscillation is clearer in the molecular case: if each atom of the molecule has a single bound state, the molecule has a symmetrical state $\varphi_s = \langle x\,|s\rangle$ and an anti-symmetrical state $\varphi_a = \langle x\,|a\rangle$, with similar spatial distributions as φ_0 and φ_1. The generation of the low plateau harmonics is described as a three-step process, in which an electronic wave packet tunnels from one molecular center to the other when the field is at its maximum [25]. Clearly, the bound part of the electron wave packet can also be written as a superposition of $|s\rangle$ and $|a\rangle$, and, as the electron moves, one would expect a similar population transfer between $|s\rangle$ and $|a\rangle$ as for the two-bound-state potential $V_G(x)$. Also for the molecular case, the time profile of the low plateau harmonics presents peaks around times for which $E(t) \simeq E_0$ [26]. However, for a diatomic molecule, the bound-bound contributions occur slightly after the peak-field time $0.25T \bmod T/2$. This is possibly related to the spatial dimensions of the molecule, which are larger than the range of $V_G(x)$. Thus, the bound part of the wave packet has to cross a larger distance, spending slightly more time.

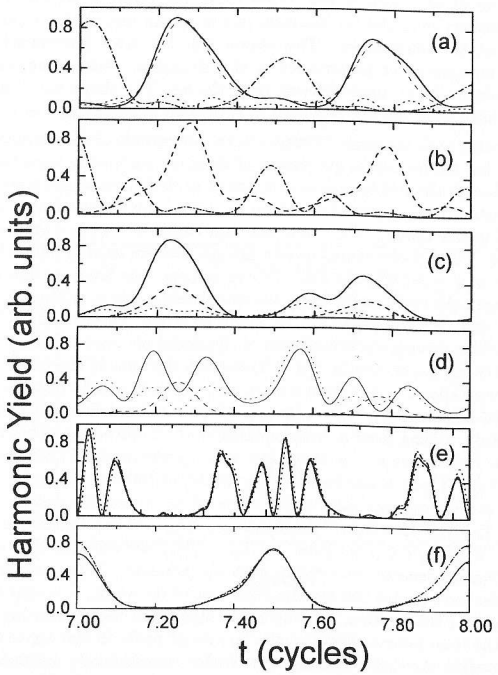

Figure 6.3: Wavelet analysis of the time-dependent dipole over one cycle of the driving laser field for the short-range Gaussian potential. Parts (a), (c) to (f) give the dipole acceleration, whereas part (b) gives the dipole length. Parts (a) and (b): $\Omega = 7\ \omega_L$, $\sigma = 0.1\,T$; Part (c): $\Omega = 15\ \omega_L$; Part (d): $\Omega = 17\ \omega_L$. Part (e): $\Omega = 37\ \omega_L$, $\sigma = 0.024\,T$ (plateau harmonics), part (f): $\Omega = 49\ \omega_L$, $\sigma = 0.1\,T$ (cutoff harmonics). Solid line: full dipole acceleration. Dashed line: bound-bound contributions. Dotted line: bound-continuum contributions. Dotted-dashed line: in parts (a) and (b) results from the two-level atom with ionization (multiplied by 3000); in parts (e) and (f) continuum-ground-state contributions.

Considering now the wavelet transform centered at the low-frequency end of the plateau harmonics, $\Omega = 15\ \omega_L$, shown in Fig. 6.3.c, one observes that the full wavelet has significant contributions from both the bound-continuum and the bound-bound parts. Increasing the center frequency just slightly, to $\Omega = 17\ \omega_L$, the bound-bound part rapidly loses its importance. In Fig. 6.3.d the bound-continuum and the full wavelet almost coincide, the bound-bound contributions now being out of phase with the full solution. Thus the dominant contribution in the full results shifts from the bound-bound part for the low harmonics to the bound-continuum part, over just a few harmonics, as is evident also from Fig. 6.1.

Finally, in Figs. 6.3.e and f we analyze the plateau and cutoff regions. In Fig. 6.3.e, we consider a window function of time width $\sigma = 0.024\ T$ centered at $\Omega = 37\ \omega_L$, so that most of the plateau harmonics are included. For this situation, we observe a near-perfect coincidence between the bound-continuum (dotted line) and the full (solid line) results, in accord with the results in Fig. 6.1. The main contributions to the bound-continuum part come from the ground-state-continuum transitions (dotted-dashed line).

Figure 6.3.f shows the wavelet transform for the cutoff harmonics, $\Omega = 49\ \omega_L$, with time width $\sigma = 0.1\ T$. Here the full result and the contributions involving the ground-state-continuum transitions (dotted-dashed line) and the bound-continuum transitions $\ddot{x}_{bc}(t)$ are almost identical. The peak in part f corresponds to the classical return time of an electron with maximum kinetic energy (see e.g. [54] or [55] and references therein). We observed small variations in the position of this peak between $t = 0.4\ T$ and $t = 0.5\ T$, which is reasonable since this return time is very sensitive towards small variations in the electron energy, as discussed in [54].

For all cases, the continuum-continuum transitions yield very small contributions, in accord with the analysis of [68].

6.2.2 Shallow long-range potential

In the following two subsections, in order to investigate the influence of the potential shape on harmonic generation, we consider model atoms with the widely used soft Coulomb potential

$$V_C(x) = -\alpha\Big[(x/\beta)^2 + 1\Big]^{-1/2}. \tag{6.10}$$

We take $\alpha = 0.38$ and $\beta = 0.76$ which leads to one bound state of energy $\varepsilon_0 = -0.19$ a.u. and several weakly bound states (binding energies of the order of 10^{-2} a.u. and smaller) in an external field of amplitude $E_0 = 0.08$ a.u. and frequency $\omega_L = 0.05$ a.u. This case is very close, apart from the potential shape, to the single-bound-state short-range potential discussed in [55], since in the presence of the external field the excited states are strongly coupled to the continuum. For the parameters stated above, the cutoff predicted by the three-step model is at $\Omega = 45\ \omega_L$.

For this binding potential, a striking agreement between the wavelet transforms for the ground-state-continuum projection and the full acceleration was observed, at the cutoff and for the whole plateau region. Once more, the semiclassical return times predicted by the three-step model have been recovered in the time profiles. These results are in agreement with a computation done by [84] for a three-dimensional long-range single-active-electron model involving ultrashort pulses, at the cutoff harmonics, and also with the results in [54] and Chapter 5. The present results (not shown) for the plateau and cutoff regions are again in agreement with these calculations, showing their generic, potential-independent nature for an effective single-bound-state atom. As in the short-range case addressed in [55], the main wavelet peak corresponds to a return time of about $t = 0.45\ T$, periodic over $0.50\ T$. If the highly-lying excited states are taken into account, we obtain a spurious peak at $E(t) = E_0$ for the bound-continuum wavelet. This feature is also observed in the next subsection (6.2.3). We regard it as unphysical, since a projection onto a field-free bound-state basis is not a good approximation for the weakly bound states.

6.2.3 Deep long-range potential

After discussing harmonic generation for models with just one or two bound states, we now wish to address the question of whether the spectral features observed are present for an atom with more than two strongly bound states.

We consider $\alpha = 0.76$ and $\beta = 1.1$ in the potential (6.10), resulting in a ground state energy of $\varepsilon_0 = -0.501$ a.u. This case differs from the one considered in Sec. 6.2.2 in the sense that also the first and second excited states, of energies respectively $\varepsilon_1 = -0.199$ a.u. and $\varepsilon_2 = -0.108$ a.u. are relatively deeply bound and strongly coupled (the dipole matrix elements between the states are respectively $\langle 0|x|1\rangle = 1.19$ and $\langle 1|x|2\rangle = 3.02$). The cutoff for this potential is, with the field parameters taken as in the previous subsections, at $\Omega = 49\ \omega_L$.

In Fig. 6.4, for the part of the spectrum above the 13th harmonic, we observe a perfect agreement between the spectrum of $\ddot{x}_{bc}(t)$ including the three most deeply bound states (c) and the full acceleration spectrum (a). The inclusion of the higher excited states (b) makes the agreement much worse, indicating the inadequacy of the field-free basis for this intensity regime. The bound-bound transitions involving only the three strongly bound states (d) exhibit a cutoff at a much lower frequency, the term proportional to $E(t)$ in the dipole acceleration expression (4.33) modifying only the background in this case. The harmonic intensities are much lower than those of the full result. The spectrum of $\ddot{x}_{bb}(t)$ involving *all* the bound states (e) (their number is finite within our discretization) yields a smeared out cutoff, which is also observed by [44]. Moreover, we observe that the spectra corresponding to continuum-ground-state transitions are at least two orders of magnitude higher than bound-continuum spectra involving only the excited bound state parts. The harmonic yields from these contributions decrease with increasing bound-state energy. This is shown in Fig. 6.4.f, where the contributions from the transitions involving the continuum and the bound state $|2\rangle$ are presented. The contributions to the b-c spectrum from the first excited state $|1\rangle$ are slightly larger, namely one to two orders of magnitude smaller than those involving the ground state. Similar results were obtained by [85] in a time-dependent computation, in which the initial atomic state was taken as a coherent superposition of ground and lowest metastable excited state. Indeed, in three-step models for high-harmonic generation the excited bound states are usually neglected, which is justified in view of the present results.

The corresponding wavelet analysis in Fig. 6.5 shows that the bound-continuum part which includes only the lowest three bound states and the full acceleration yield almost indistinguishable wavelet transforms for both part a and b. The bound-continuum part including all bound states is also in agreement with the other two sets of results, apart from a spurious peak at maximal field ($t = 0.25\ T$ modulo $0.5\ T$). This spurious (unphysical) peak is due to the contribution of the highly-lying excited states in the time-dependent projections. This peak is not present in the harmonics of energy higher than the cutoff, indicating that it arises only from the high-plateau harmonics. Once more, in part b, the cutoff return time $t \simeq 0.4T$ is recovered for the full acceleration and $\ddot{x}_{bc}(t)$.

For the lower-energy part of the spectra, however, the harmonics appear to be a "mixture" of bound-continuum and bound-bound transitions, and it is difficult to draw conclusions about which mechanism plays the most important role. This is clearly observed in the wavelet transform centered at the 7th harmonic (not shown). In this case, the wavelet transform no longer exhibits the $T/2$ periodicity of the driving field but there are other timescales present, presumably due to resonant processes involving several bound atomic states. Concerning the term in $\ddot{x}_{bb}(t)$ which is proportional to the field: as briefly mentioned in Sec. 6.1 it introduces an over-enhancement of the peak at maximum field ($t = 0.25\ T$ modulo $0.5\ T$) when all the bound states are taken into account. The reason is that the projections on all these states become large for maximal field. If just the three most deeply bound states are taken into account, the term in $E(t)$ plays no important role in the wavelet transforms, the result with and without this term being almost identical. Moreover, even though the excited states $|1\rangle$ and $|2\rangle$ are strongly coupled, the wavelet transforms of $\ddot{x}_{bc}(t)$ for

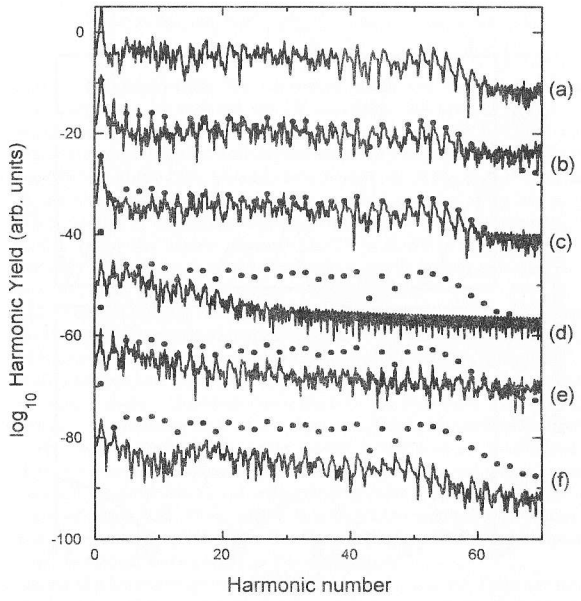

Figure 6.4: Power spectra of the time-dependent dipole acceleration for the deep Coulomb potential. Part (a): full acceleration; Part (b): bound-continuum part; Part (c): bound-continuum part from the three most deeply bound states; Part (d): bound-bound part from the three most deeply bound states; Part (e): bound-bound part ; Part (f): bound-continuum part for the second excited state only. All subsequent curves have been shifted by -15 y-axis units from their respective upper neighbors. The harmonic peak heights from curve (a) have been repeated as the filled circles for all other five curves, as a point of reference.

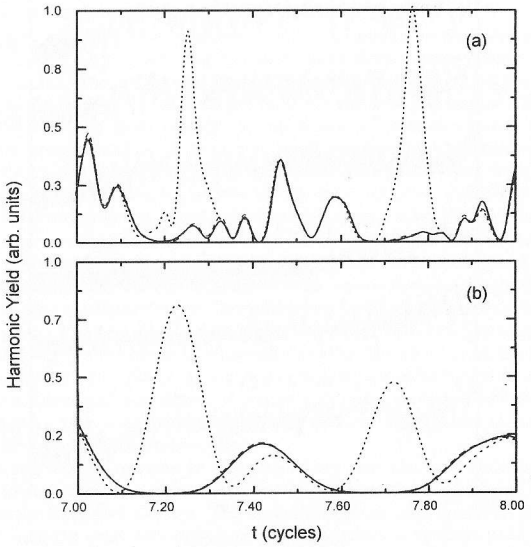

Figure 6.5: Wavelet analysis of the time-dependent dipole acceleration over one cycle of the driving laser field for the deep Coulomb potential. Part (a): Plateau harmonics, $\Omega = 37\omega_L$, $\sigma = 0.027\,T$. Part (b): Cutoff harmonics, $\Omega = 51\omega_L$, $\sigma = 0.108\,T$. Solid line: full dipole acceleration. Dashed line: bound-continuum contributions from the three most deeply bound states. Dotted line: bound-continuum contributions.

only the two or only the three most deeply bound states present no significant difference.

6.2.4 Effects of the Coulomb Tail

In order to investigate quantitatively the effects of the long-range Coulomb tails in the deep Coulomb potential of the previous subsection, we now discuss and compare results obtained with the same potential, where the Coulomb tails have been cut off,

$$V_T(x) = V_C(x) \begin{cases} 1 & , \quad |x| < a_0 \\ \cos^n\left[\frac{\pi}{L-a_0}(x-a_0)\right], & a_0 < |x| < L \\ 0 & , \quad L < |x|\,. \end{cases} \tag{6.11}$$

For regions close to the atomic core, this expression yields the deep Coulomb potential V_C from Subsec. 6.2.3. For $|x| > a_0$, its tails are cut off smoothly. We take $a_0 = 5$, $n = 6$ and $L = 2\alpha_0$, α_0 being the excursion amplitude of the electron ($\alpha_0 = E_0/\omega^2 = 32.$). Thus, within its excursion amplitude, the electronic wave packet will experience a very different potential tail between V_C and V_T. For the parameters above, the ground state energy ε_0 of V_T is the same as the one for V_C (Subsec. 6.2.3), while the first and second excited states' energies of V_T are at $\varepsilon_1 = -0.192$ and $\varepsilon_2 = -0.063$. The energies of the higher excited bound states are of course quite different between the two potentials. (Also the matrix element $\langle 1|x|2\rangle = 0.499$ is very different.) The truncated potential V_T has only a finite number of bound states, seven within our discretization. We apply exactly the same field pulse as for the previous results shown.

The effects of Coulomb tails on harmonic generation spectra have been discussed in several papers before [86]. Mainly, however, these discussions were concerned with elliptically polarized driving fields, investigating harmonic energies close to the ionization energy ("threshold" harmonics). Unusual ellipticity dependence was observed, whose origin was usually surmised to lie in the dominant effect of excited bound states. Coulomb corrections to the free wave packet evolution within the context of multiphoton ionization and above-threshold (high photoelectron energy) multiphoton ionization have also been addressed [87], again mainly in the context of elliptical polarization and thus concerned with wave-packet spreading transverse to its principal excursion amplitude. In the present study, we are uniquely concerned with the *longitudinal* spreading of our (1D) wave packet in a linearly polarized laser field. Even within this restricted context, one should expect quantitative differences in the harmonic yield, since the Coulomb tails affect atomic ionization [87] and the propagation of the electronic wave packet in the continuum.

When comparing the harmonic generation spectra from V_C and V_T, there are no major differences visible on the scale of Fig. 6.4 (the results for V_T are not shown in the figure). However, there are quantitative differences of about one order of magnitude. The V_T harmonics at the cutoff are slightly (a factor 2-3) lower than the V_C harmonics. On the other hand, there are a few groups of harmonics, in the plateau (around the 35th) and at threshold (around the 11th) where the V_T harmonics are about one to two orders of magnitude higher than the V_C harmonics. Again, there is perfect agreement between the full and the $\ddot{x}_{bc}(t)$ high-energy spectra for V_T, where only the lowest three bound states are taken.

We now consider the wavelet transforms for the two sets of results. For the low harmonics, for $\Omega = 7\omega_L$ and $\sigma = 0.108\ T$, we observe that the results for V_T are much less structured than the results for V_C. The results for V_T are dominated by a single smooth peak, near $0.25T$, periodic modulo $T/2$, as was the case for the short-range Gaussian potential, discussed in Fig. 6.3. This suggests that the non-periodic wavelet yield of V_C for the low harmonics is inherent to the long-range tail of (6.10). However, for the potential (6.11) it is not clear whether the low harmonics are originated by the bound-bound or bound-continuum transitions, since both contributions present well-defined maxima at peak-field times.

For the plateau region, for $\Omega = 37\ \omega_L$ and $\sigma = 0.027\ T$, V_T exhibits much less structured temporal profiles than V_C, this time dominated by a peak near $0.50\ T$. At the cutoff, finally, very similar wavelet yields are obtained for V_T and V_C, once more indicating the potential-independent nature of the cutoff harmonics. The cutoff return time is slightly shifted between the different sets of results: V_C yields $0.42\ T$, V_T yields $0.47\ T$, while V_G gave $0.45\ T$ [55] for the (single) peak of the temporal signal. The width of the peak, however, is much larger than these differences, and thus the wavelet cannot really (neither in practice nor in principle) resolve such a small difference.

According to our analysis, the long-range tail of the Coulomb potential influences mainly low- and threshold harmonics, and, depending on the potential in question, might affect particular groups of plateau harmonics. The effect of truncating or not the long-range potential, even quantitatively, does not have a significant influence on the cutoff harmonics.

6.2.5 Gauge dependence

As discussed in Sec. 6.1, the time-dependent projections in a field-free bound-state basis are gauge-dependent and one has to be careful about the choice of gauge. In the present low-frequency region, the projections make sense only when taken in the length gauge, as has also been argued in [81] and [82]. In this subsection, we present misleading results obtained in the velocity gauge as an example. We take the short-range potential from Subsec. 6.2.1, which has two deeply bound states, and calculate the time-dependent projections in the velocity gauge. In this case, the plateau- and cutoff-structure is recovered also for the $\ddot{x}_{bb}(t)$ spectrum. This can be seen in Fig. 6.6, where the spectra for $\ddot{x}_{bb}(t)$, $\ddot{x}_{bc}(t)$ and $\ddot{x}(t)$ in the velocity gauge are presented. The full line gives the "exact" result, the same as the dashed line in Fig. 6.1. The key point of the present figure is that the various projection contributions (bound-bound and bound-continuum) are much larger than those of the full result (the continuum-continuum contribution is roughly of the order of magnitude of the full result). This indicates that the projections in the velocity gauge cannot be expected to yield much physical information individually, since they cancel each other to a large extent when summed to give the full result.

Moreover, performing the wavelet analysis for the present case, shown in figure 6.7.a for the plateau harmonics, one observes that the $\ddot{x}_{bb}(t)$ contribution is similar to the full $\ddot{x}(t)$, whereas the $\ddot{x}_{bc}(t)$ wavelet is completely out of phase with the full result. This appears to lead to the conclusion that, for atoms with strongly coupled bound states, the bound-bound transitions play a very important role in the generation of plateau harmonics. However, it must be noted that, as shown in part 6.7.b, all the contributions (although most prominently the bound-free contribution) reproduce the return time $t \simeq 0.5\ T$ at the cutoff.

Considering the ground-state and excited-state populations obtained by projecting the velocity-gauge wavefunction, shown as the thin lines in Fig. 6.2, the former presents maxima for times $t = 0.25\ T$ modulo $0.5\ T$, corresponding to maximum field strength $E(t) = E_0$. These results are obviously unphysical, when viewed in a quasi-static field picture. This justifies the gauge transformation introduced in the present analysis. Studies concerning the gauge dependence of time-dependent projections were also performed by [81] within the context of population transfer.

6.3 Discussion

We wish to draw the following qualitative conclusions on high-harmonic generation, based on the results within our projection method:

There is no significant qualitative influence on either low- or high-harmonic generation from the long-range shape of the potential. In other words, for long-range potentials, the highly excited bound

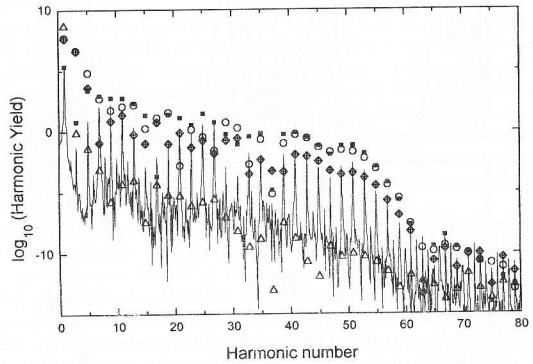

Figure 6.6: Power spectra of the dipole acceleration for the Gaussian potential. All projections (but one, see below) are performed in the velocity gauge. Solid line: spectrum of the full acceleration (same as in Fig. 6.1). Filled squares: bound-bound contribution. Circles: bound-continuum contribution. Crossed diamonds: continuum-continuum contribution. Triangles: continuum-continuum contribution from length-gauge projection.

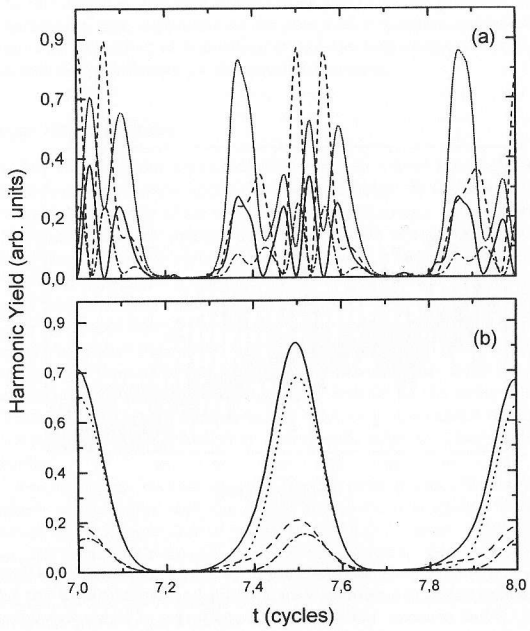

Figure 6.7: Wavelet transform of the time-dependent dipole acceleration for the Gaussian potential. The projections are performed in the velocity gauge. Part (a): Plateau harmonics, $\Omega = 37\omega_L$, $\sigma = 0.024\,T$. Part (b): Cutoff harmonics, $\Omega = 49\omega_L$, $\sigma = 0.1\,T$. Solid line: full dipole acceleration. Dashed line: bound-continuum contributions. Dotted line: bound-bound contributions. Dotted-dashed line: continuum-continuum contributions.

states do not play a significant role. When observing 3-D effects, however, as for example in the ellipticity dependence of harmonic generation [86], the potential tails may become important.

For atoms with more than one bound state, both the bound-bound and the continuum-bound transitions play a role in the harmonic generation process. The generation of high harmonics corresponds to a three-step physical picture, in which the main contributions within a field cycle correspond to the semiclassical return times, even for long-range potentials. For all the potentials studied, only the bound-free transitions originate a cutoff at the semiclassical energy $|\varepsilon_0| + 3.17\,U_p$. Both spectral and time-frequency analysis demonstrate that the main contributions to high-harmonic generation come from transitions involving the ground state. This shows that the electronic wave packet not only rescatters with the atomic potential, but really recombines to the ground state.

On the other hand, the low harmonics appear to be the result of several mechanisms, depending very much on the potential in question. Our analysis shows that indeed the excited bound states play a significant role in the properties of these lower harmonics, in agreement with the interpretation of some of the results in [86, 87].

Specifically, for an atom with only two deeply bound states, the bound-bound transitions play the dominant role in the generation of harmonics at the low-energy side of the plateau. Similar results were also obtained by [45]. However, the plateau and cutoff at $\omega_{10} + 3\,U_P$ reported in this publication are absent in our computation. It should be noted that we do take recombination into account for the amplitudes $C_n(t)$. Only in the velocity gauge, for which the time-dependence of the ground- and excited state populations yields unphysical results, a plateau and a cutoff within this frequency regime is observed. The mechanism of harmonic generation in a two-level atom leads to a temporal structure in the low-harmonic generation which is completely out of phase with the main process of harmonic generation in a spatially extended atom.

In the low-frequency regime we observe strikingly different bound-bound and two-level atom spectra and wavelet transforms. The spectra can be made to appear more similar if one chooses much higher ionization rates in the two-level atom model. This indicates that the high-frequency components in the amplitudes $C_n(t)$ of the bound states from the full solution are very different from the corresponding components in the amplitudes from the two-level atom model, due to the contribution of the continuum states in the dynamics of the driven atom, even though the dynamics involves primarily only a charge oscillation between the lowest two bound states. A critical influence of the bound-state population transfers on harmonic generation was also observed by [88], as well as ionization-related effects in the bound-state population dynamics.

For the particular case of an atom with only two strongly coupled bound states, we conclude that the low harmonics are not well represented by a two-level atom. Even the insertion of effective ionization rates yields a completely inappropriate model for the low-energy spectral region. As the harmonic frequency increases, the three-step model becomes the appropriate picture for the high-harmonic generation process.

Chapter 7

High-harmonic generation with bichromatic driving fields

For HHG with monochromatic driving fields, the existence of a simple cutoff law for the atomic emission spectra is an established fact. Moreover, the mechanisms responsible for HHG in this case are the bound-free transitions of the three-step model. However, for nonmonochromatic fields there are still several open questions concerning an explicit cutoff law and the validity of the rescattering picture. The existence or absence of a simple cutoff law of the form $|\varepsilon_0|+\alpha U_p$ in the bichromatic case has been extensively discussed [28, 67, 89], but no general expression exists. Moreover, the harmonic output has a more complex structure in the nonmonochromatic case, depending on the shape of the driving field. The more parameters the latter has the more knobs can be turned. For instance, a linearly polarized bichromatic field already provides two additional parameters in comparison to the monochromatic case, viz. the ratio of the two field strengths and the respective phase. Thus, the possibility of controlling the length of the plateau or to enhance or suppress a selected group of harmonics by adjusting the parameters of the coherent fields has attracted the attention of several groups, originating several experimental [62, 94, 95] and theoretical [28, 61, 67, 89, 90, 91, 92] studies on the subject. Special features of harmonic generation with bichromatic fields, such as the enhancement of the plateau harmonics in at least one order of magnitude with respect to the monochromatic case [92, 95], the extension of the plateau towards higher energies [28, 89, 96] and the production of attosecond pulses [61, 62] have been identified and investigated within the past few years.

With the same motivation as these groups, i.e., to gain useful information for high-intensity-coherent control, we performed the investigations presented in this Chapter. We restrict ourselves to a-one dimensional atom model, for which qualitative features concerning two-color HHG with linearly polarized light are present. We solve the TDSE for a one-bound state atom with the same short-range gaussian potential (5.1) as in Chapter 5, subject to a bichromatic field of the form

$$E(t) = E_{01}\sin(\omega_1 t) + E_{02}\sin(\omega_2 t + \phi)\,. \tag{7.1}$$

The frequencies are taken to be commensurate, $\omega_2 = n\omega_1$, with n being an integer, so that the phase ϕ has physical significance. For this field, the ponderomotive energy is given by

$$U_p = E_{01}^2/4\omega_1^2 + E_{02}^2/4\omega_2^2. \tag{7.2}$$

We take the driving field (7.1) with $n=2$, i.e. one of the driving waves as the second harmonic of the other. However, one should keep in mind that the formalism used in our investigations can in

principle be applied to *any* nonmonochromatic field. Clearly, for our field choice there are also even harmonics in the emission spectra. The chapter is divided in two main parts, with emphasis on two different aspects of two-color HHG:

In Sec. 7.1, the reliability of simple semiclassical (three-step) pictures for bichromatic driving fields is investigated. We use spectral and time-frequency analysis to determine the main contribution to high-harmonic generation within a field cycle for bichromatic fields, extracting the semiclassical return times from the TDSE computation.

In Sec. 7.2, we concentrate on how the relative phase and the relative intensities of both driving waves affect the maximal-energy trajectories of the returning electron and, consequently, the harmonic spectra, for bichromatic driving fields. We also address the question of whether there is an analog of the simple cutoff law pertinent to the monochromatic case. Within the two-color framework, it is clear that the relative field strengths E_{01}, E_{02}, the frequency ratio n and the relative phase ϕ are the important parameters determining the extremal-energy emission and return times (t_0, t_1).

Concerning these maximal- (and sometimes minimal-) energy trajectories, there is an important difference between the monochromatic and bichromatic cases. In the monochromatic case, it so happens that the start time t_0 of the maximal energy solution with shortest travel time is very close to the time where the electric field is maximal, so that, in the tunneling regime, injection of the electron into the field is most likely[1]. This is not necessarily so in the bichromatic case. There are solutions (t_0, t_1) that lead to extremal return energies, but for whom the field $E(t_0)$ is comparatively weak. Hence, within the tunneling regime, the corresponding cutoff frequencies may not be prominent in the spectrum.

In both parts, when investigating phase-related effects, we take fields of equal amplitude, for which these should be most pronounced. High-harmonic generation with comparable bichromatic driving fields was addressed experimentally in [94]. We consider excursion times $t_1 - t_0$ for the electron in the continuum up to two periods $T = 2\pi/\omega_1$ of the low-frequency field. There are infinitely many return times for which the excursion time $t_1 - t_0$ is longer than two periods. However, due to wave packet spreading, even in 1D, these longer return times are of minor importance in the harmonic generation spectra. For Sec. 7.1 we impose the additional condition $t_1 \leq 2T$, since we did not observe significant contributions for the wavelet yield from longer return times.

7.1 Time-frequency analysis of two-color HHG

For the studies performed in this section, we take $E_{01} = E_{02} = E_0 = 0.04$ a.u., and $\omega_1 = 0.05$ a.u. in Eq. (7.1). This field has a ponderomotive energy of $U_p = 0.2$ a.u., which gives a Keldysh parameter $\gamma = \sqrt{|\varepsilon_0|/2U_p} = 1$. We present results for $\phi = 0$ and $\phi = \pi/2$.

7.1.1 Classical return times

In Figs. 7.1 and 7.2 we present the complete picture of the emission and return times obtained from a numerical solution of the time-dependent classical equations of motion of an electron in the field, for $\phi = 0$ and $\phi = \pi/2$, respectively, using the fourth-order Runge-Kutta method (a discussion of this method can be found in Appendix D). It is worth noting that the introduction of a second driving field results in a much more complex pattern for the semiclassical trajectories (for a comparison, see for instance the same diagram for monochromatic driving fields, presented in Sec. 4.1.2 and [54]). The figures have been obtained as follows: we cover the interval $0 \leq t_0 \leq T$ (with $T = 2\pi/\omega_1$ the

[1] This can be clearly seen in Figs. 4.3.(a) and 4.4 in this thesis. In Fig. 4.3.(a), the graphical method explained in Chapter 4 shows that the field at the emission time corresponding to the cutoff ε_{max}, given in Fig. 4.4, is close to its maximum.

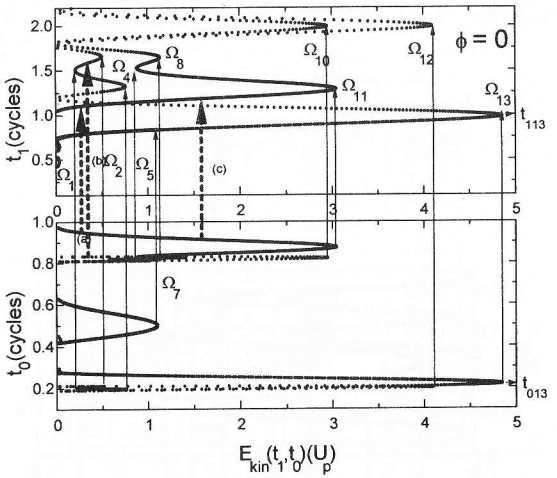

Figure 7.1: Classical emission and return times as a function of return energy for an electron in a field as in Eq. (7.1), with $E_{01} = E_{02} = E_0$, for $\phi = 0$. Lower part: emission times; upper part: return times. The solid arrows connecting both parts indicate the extremal energy trajectories, in accordance with Table I. The dashed arrows indicate non-extremal trajectories which give rise to peaks in the wavelet yield of Fig. 7.4.

period of the low-frequency driving field) of the start times with a closely spaced uniform grid. For each t_0 we calculate the associated return time t_1 and kinetic energy $E_{\rm kin}(t_1, t_0)$. In general, there will be more than one solution for each t_0. Each triplet $(t_0, t_1, E_{\rm kin}(t_0, t_1))$ provides one entry for Fig. 7.1 or 7.2.

Occasionally, we will refer to a triplet $(t_0, t_1, E_{\rm kin}(t_0, t_1))$ as a "trajectory". Indeed, a classical electron trajectory starting with zero velocity from the ionic core ($x = 0$) and returning to it is uniquely specified by t_0 and t_1. Extremal values of the return energies (mostly maxima, sometimes minima) in the curves of Figs. 7.1 and 7.2 specify the cutoff energies and the corresponding emission and return times. In this case, we will cavalierly speak of "extremal trajectories". All others will be referred to as "nonextremal trajectories". The density of t_1-points in the figures allows to draw conclusions about the relevance of the corresponding trajectories to the harmonic response. Both figures 7.1 and 7.2 show the return times only for returns during a time shorter than $2T$.

For $0 \leq t_0 \leq T$ and $t_1 - t_0 < 2T$, extremal energies, Ω_j with their associated emission times t_{0j} and return times t_{1j} are given in Table I (for $\phi = 0$) and Table II (for $\phi = \pi/2$), the subscript j labeling the solutions in increasing order of Ω_j. The corresponding harmonic number is obtained as $\Omega_j/\omega_1 + 8$, since it results from a recombination energy of $E_{kin}(t_1, t_0) + |\varepsilon_0|$(where $|\varepsilon_0| = 8\hbar\omega_1$). The fifth column gives the kinetic energy of the returning electron in units of the ponderomotive

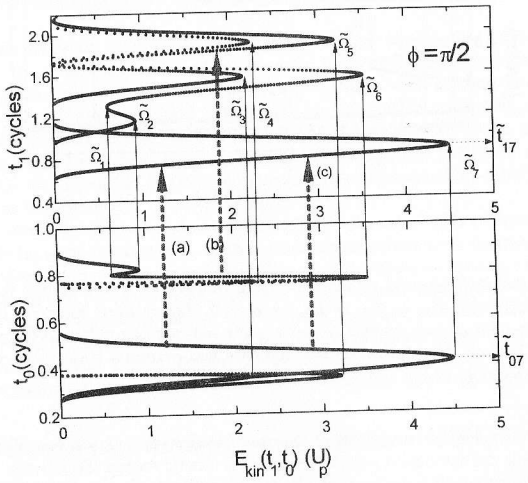

Figure 7.2: Same as Fig. 7.1, but for $\phi = \pi/2$. The relevant extremal energy trajectories are listed in Table II.

energy. In the next subsections, only trajectories with return times $0 \leq t_1 \leq 2T$ will be taken into account, since only these contribute to the harmonic yield. The longer return times in Table I, as well as the respective cutoff frequencies, corresponding to $j = 3, 6$ and 9, will be only necessary in the discussions of Sec. 7.2.

Table I: cutoff emission and return times, and the respective harmonic frequencies, for $\phi = 0$.

j	t_{0j}/T	t_{1j}/T	$(\Omega_j + \lvert\varepsilon_0\rvert)/\omega_1$	Ω_j/U_p
1	0.20	1.50	9.04	0.22
2	0.21	1.67	10.0	0.50
3	0.85	2.51	10.4	0.59
4	0.20	1.32	10.7	0.67
5	0.83	1.53	11.5	0.88
6	0.85	2.60	12.1	1.02
7	0.50	0.85	12.5	1.13
8	0.82	1.65	12.6	1.14
9	0.85	2.30	13.7	1.43
10	0.81	1.99	19.9	2.98
11	0.88	1.29	20.2	3.05
12	0.20	1.99	24.4	4.12
13	0.22	0.98	27.4	4.86

Table II: cutoff emission and return times, and the respective harmonic frequencies, for $\phi = \pi/2$.

j	$\tilde{t}_{0j}/T$	$\tilde{t}_{1j}/T$	$(\tilde{\Omega}_j + \lvert\varepsilon_0\rvert)/\omega_1$	$\tilde{\Omega}_j/U_p$
1	0.80	1.30	10.5	0.62
2	0.82	1.18	11.7	0.92
3	0.36	1.57	16.3	2.16
4	0.76	1.90	17.0	2.24
5	0.30	1.86	20.7	3.20
6	0.77	1.56	22.0	3.54
7	0.42	0.88	25.9	4.48

The cutoff energies fall into two categories, the high-harmonic peaks, above harmonic 16, and the low harmonic peaks, below harmonic 16; this dividing line is indicated in the tables. Tables I and II show that there are regions of the harmonic spectrum without any extremal energies Ω_j, so that in the classical picture harmonics in these regions can only be due to "nonextremal" trajectories. In fact, Figs. 7.1 and 7.2 show that a given return energy can be accomplished by several start and return times t_0 and t_1 such that the return energy is *not* extremal. The corresponding times t_0 and t_1 satisfy the return condition (4.6), but not the extremal energy condition (4.7). Whenever possible, we shall discuss the results in Subsec. 7.1.2 and 7.1.3 in terms of *extremal* return times. However, in several situations one must refer to non-extremal trajectories for the returning electron (cf. Subsec. 7.1.3). Dashed arrows in Figs. 7.1 and 7.2 mark those nonextremal trajectories whose return times are observed in the time-frequency yields presented in Subsec. 7.1.3. We shall refer to them by $(t_{0(\mu)}, t_{1(\mu)})$, where the index μ increases in alphabetical order with the energy.

The radically different patterns in Figs. 7.1 and 7.2, where not only the cutoff energies, but also the number of extremal-energy trajectories (for Fig. 7.1, ten cutoff frequencies are present within

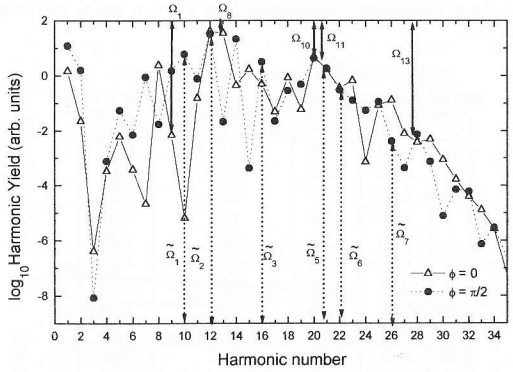

Figure 7.3: Harmonic spectra for a field (7.1) with $E_{01} = E_{02} = 0.04$ and phases $\phi = 0$ (triangles) and $\phi = \pi/2$ (filled circles). The cutoffs for which an abrupt intensity decrease is present are indicated. Only the harmonic peak heights are shown, connected by a thin line to guide the eye. The solid and dashed lines relate, respectively, to $\phi = 0$ and $\phi = \pi/2$.

the additional restriction $t_1 < 2T$) vary dramatically with respect to the phase, already suggest the inexistence of a simple cutoff law of the form $\epsilon_{\max} = |\epsilon_0| + \alpha(\phi)U_p$. The cutoff frequencies are connected in an intrincated way, which will be discussed in Subsec. 7.2.2.

7.1.2 Harmonic spectra

In Fig. 7.3 we show the harmonics' power spectrum for the two cases, $\phi = 0$ and $\phi = \pi/2$, obtained through the numerical solution of the time-dependent Schrödinger equation. Some of the maximal-energy cutoffs of Table I ($\phi = 0$) can be clearly seen: around the frequencies Ω_1, Ω_8, Ω_{11} and Ω_{13} maxima are observed with subsequent abrupt decreases in the harmonic intensities. Similar results are obtained for the case $\phi = \pi/2$ (filled circles in Fig. 7.3). Near most of the cutoff energies of Table II (except $\widetilde{\Omega}_4$), again significant decreases of the harmonic intensities in the power spectrum are observed. The fact that only some cutoffs are followed by abrupt intensity decreases in the harmonic yield is not surprising, since there are several semiclassical interfering cutoff trajectories within a very close energy range. Moreover, this interference pattern is also strongly affected by the intensity of the *entire* field (7.1). This might seem strange at first sight, since the start and return times presented in Figs. 7.1 and 7.2 are unaffected if the entire field (7.1) is multiplied by a constant factor. The kinetic energy upon return just scales with the square of this factor. The harmonic spectrum does not fully reflect this scaling property of the classical equations of motion. The reason is that the first step of the three-step model, viz. the probability that an electron is emitted into the field, scales exponentially with the field in the form $\exp(-C/|E(t)|)$, which favors start times where the field is strong. This dependence of the harmonics on the field at the emission time t_0 is also shown by the variation of the harmonic yield with the relative phase ϕ. An example is presented

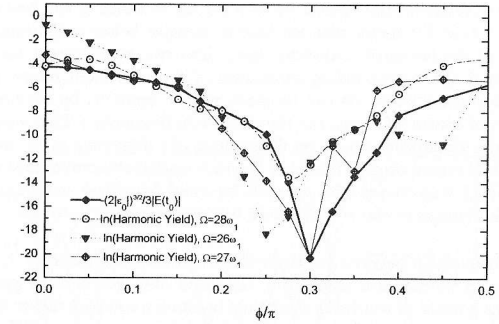

Figure 7.4: Harmonic yield as function of the relative phase ϕ, for $\Omega = 26\omega_1$(solid triangles), $\Omega = 27\omega_1$(cross-centered diamonds) and $\Omega = 28\omega_1$(dot-centered circles), connected by thin lines, compared to the quasi-static ionization rate (solid diamonds connected by a thick line).

in Fig. 7.4, where the intensities of the harmonics $\Omega = 26\omega_1$, $\Omega = 27\omega_1$ and $\Omega = 28\omega_1$, given as functions of ϕ, are compared to the quasi-static tunneling rate, $\exp[-C/|E(t_0)|]$. Both $E(t_0)$ and t_0 depend on ϕ. Particularly for $\phi \simeq 0.35\pi$ the emission time jumps from $t_0 \simeq 0.2T$ to $t_0 \simeq 0.4$ due to the merging of two semiclassical cutoff trajectories. This is discussed in more detail in the next section. The global behavior of the harmonic yield and the predictions of the quasi-static rate are strikingly similar, showing a pronounced dip near $\phi = 0.3\pi$.

Another feature of the spectrum for $\phi = 0$ appears noteworthy. Figure 7.1 shows there is a significant range of energies – between Ω_8 and Ω_{10} – without any extremal energy[2]. A glance at the spectrum of Fig. 7.3 draws attention to a suppression of harmonic intensities within this range.

7.1.3 Time-frequency analysis

A detailed analysis of the harmonic response in a certain frequency range with regard to the corresponding emission and return times can be performed through the wavelet analysis. Since we are mainly interested in the cutoff trajectories, we center the window function approximately at a cutoff frequency. Figure 7.5 gives the corresponding wavelet yields. The width of the analyzing wavelet is chosen as $\sigma = 0.1\ T$. The corresponding window in frequency is $2/\sigma$, covering about two harmonics on either side of the center (or $0.8\ U_p$ on the scale of Figs. 7.1 and 7.2). The temporal structures in Fig. 7.5 which are quasi-periodic in the field cycle T represent the main contributions to the generation of this group of harmonics. One should note that for monochromatic driving fields this

[2] In Table I, there is still the cutoff Ω_9, with slightly larger energy than Ω_8. However, no contribution to the harmonic yield is given by the return time in question.

periodicity is reduced to $T/2$[3]. The fact that the temporal patterns of Figs.7.5(a) and 7.5(b) are only approximately periodic in T is due to the turn-on of the field and to ionization which is inherent in the TDSE wave function.

We will now try to interpret the wavelet pattern mainly in terms of the "extremal trajectories". Inspection of Figs. 7.1 or 7.2 shows that for kinetic energies below a maximal energy (or above a minimal energy) Ω the extremal trajectory splits into two nonextremal energies. As long as $E_{\rm kin}$ is still close to Ω the corresponding separation of the associated return times is small and will not show in the wavelet yield. (It can be made visible, however, by narrowing the window in time at the expense, of course, of increasing the window in frequency.) This separation is, however, responsible for a slight disagreement between the position of a maximum in the wavelet yield and the corresponding maximal return time of Table I or II which we will observe in some cases. Occasionally we observe the effect of trajectories with energies far away from their extremal values Ω. In such cases, we will ascribe bumps in the wavelet yield to nonextremal trajectories, or rather to sets of these.

There is a close connection between our trajectories and those identified in the Lewenstein model [41, 54]. In addition to the classical kinematics, the latter also incorporates the initial (tunneling) ionization process, as a result of which the start time becomes a complex rather than a real quantity. As a consequence, the trajectories of the Lewenstein model are much more difficult to calculate. In the preceding paragraph, we described the splitting of an extremal trajectory into two nonextremal trajectories when the energy decreases below a cutoff energy. This is a feature that is shared by both models.

Let us now discuss in detail the correspondence between the peaks in Fig. 7.5 and the return times of Tables I and II and of Figs. 7.1 and 7.2. We first consider, for $\phi = 0$, the time-dependent wavelet yield for the window centered at $\omega = 20\omega_1$ (Fig. 7.5(a), dashed line). We observe two bumps, at $t_1 = 0.27\ T \pmod T$ and $t_1 = 0.97\ T \pmod T$, which are very close to the extremal return times t_{111} and $t_{113} \approx t_{112}$ of Table I. The energy Ω_{111} is at the center of the frequency window, hence it makes the largest contribution. Another very noticeable feature is the absence of any significant yield between $t_1 \approx 0.5\ T \pmod T$ and $t_1 \approx 0.8\ T \pmod T$. Indeed, Fig. 7.1 confirms there are no return times (extremal or other) contributing within this frequency window.

A very similar situation occurs for the frequency window centered at $\omega = 27\omega_1$, the position of the highest cutoff energy (Fig. 7.5(a), dotted line). Bumps are observed at nearly the same positions as before, but their magnitudes have been exchanged. This is expected from the simple graphical method, since now the dominant contribution ought to come from the return at t_{113}. A quite noticeable contribution is still made by t_{111} even though the corresponding energy is only in the wings of the frequency window. Just as for the window centered at $20\omega_1$, there is again a range of return times which generate no contribution at all, which has expanded to $0.4T \le t_1 \pmod T \le 0.8T$.

The analysis of the results for the frequency window centered at $\omega = 12\ \omega_1$ (Fig. 7.5(a), solid line) is more involved. This is in the low-energy range, and a glance at the region around $E_{\rm kin} = U_p$ in Fig. 7.1shows that due to the large amount of structure at low energies a detailed interpretation of the wavelet yield will be difficult and ambiguous. The most conspicuous feature of the wavelet yield is the absence of any contribution from return times $t_1 \pmod T$ around $0.9\ T$. This is in good agreement with Fig. 7.1 which does not exhibit any trajectories returning around this time with an energy near the frequency window. The frequency window includes the extremal return energies from Ω_2 to Ω_8 (given in table I, with the associated return times). These times can be

[3]Recall that for a monochromatic field $E(t)$ we have $E(t+T/2) = -E(t)$ and $A(t+T/2) = -A(t)$. For bichromatic fields this condition holds for odd frequency ratio $n = \omega_2/\omega_1$, but not for even n. The different periodicity is already observed for E_{02} two orders of magnitude smaller than E_{01}. This is not explained by the classical model which does not hold when one of the two fields is too weak.

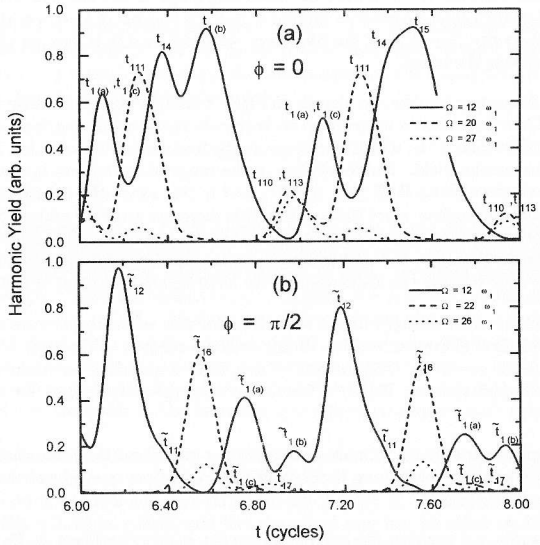

Figure 7.5: Part (a): wavelet transforms for $\phi = 0$. Solid line: window function centered at $\Omega = 12\omega_1$, dashed line: window function centered at $\Omega = 20\omega_1$; dotted line: window function centered at $\Omega = 27\omega_1$. Part (b): wavelet transforms for $\phi = \pi/2$. Solid line: window function centered at $\Omega = 12\omega_1$, dashed line: window function centered at $\Omega = 22\omega_1$, dotted line: window function centered at $\Omega = 26\omega_1$. In all the plots, $\sigma = 0.1T$.

found represented in the wavelet yield, with the notable exception of t_{17} to be discussed below. They interfere in complicated ways which cannot be inferred from Fig. 7.1, but the fact that they do is evident from the quite different wavelet yields within the two periods of the driving field which are covered by Fig. 7.5(a): the physical situation within these two periods only differs by the amount of ionization reached. Hence the fact that the wavelet yields are so different must be traced to interference mechanisms.

The conspicuous bump near $t_1 = 0.1T \pmod T$ (Fig. 7.5(a), solid line) cannot be explained by any extremal trajectory in Table I. This is an example of the importance of nonextremal trajectories as defined and explained in Sec. 7.1.1. Within the frequency range of concern, Fig. 7.1 shows a very well developed set of nonextremal trajectories around $t_1 = 1.1\,T$ (as part of the curve that ultimately reaches the extremal energy Ω_{11} outside the frequency window), and it is this set of nonextremal trajectories that generates the bump.

Within the same frequency window, we identify in Fig. 7.1 another very marked set of trajectories near $t_1 = 0.85\,T$. These trajectories correspond to harmonic energies varying from the ionization threshold to the cutoff frequency Ω_7, which is *well inside* the frequency window. This, however, does not show at all in the wavelet yield. The reason lies in the range of start times t_0 corresponding to this trajectory. It comprises about $0.4T \le t_0 \le 0.6T$, and in this range the driving electric field is very weak. In the tunneling regime, start times within this range are strongly underrepresented, and consequently, their contributions do not show in the harmonic response. This argument suggests that they might become visible in the multiphoton regime (that is, for lower driving intensities) where all start times have roughly the same weight. We have checked that this is indeed the case.

Information about the field strength at the start time for this set of trajectories can be gained using the graphical method discussed in 4.1.1. If one draws a tangent to the $F(t) = \int A(t)$ curve, such that the rescattering condition (4.6) for $0.4T \le t_0 \le 0.6T$ is satisfied, one clearly notices that $F(t)$ in this region is approximately linear. This means that the electric field for these times is approximately zero.

In general, we expect a trajectory to make the stronger a contribution to the wavelet yield, the higher the density of relevant return times, the shorter the travel time $t_1 - t_0$, and the stronger the electric field is at the start time t_0.

As a further example, we perform the same analysis for $\phi = \pi/2$, shown in Fig.7.5(b). The classical trajectories' start and return times are depicted in Fig. 7.3.

Again we obtain a complete explanation of all spectral features in terms of the classical return times. Concentrating on the wavelet yields in the high-energy part of the spectrum, $\omega = 22\omega_1$ and $\omega = 26\omega_1$. We observe bumps at $t_1 = \tilde{t}_{16}$ and $\tilde{t}_{17}$ as expected. However, the bump at $\tilde{t}_{16}$ is dominant even for the frequency window centered at the higher energy of $26\omega_1$. Since the cutoff energy $\widetilde{\Omega}_7 = 25.9\omega_1$ is just at that point, one would have expected the bump at $\tilde{t}_{17} = 0.88T$ to be the strongest, which is not the case. The explanation can be found again in the value of the electric field at the start time t_0. At the start time corresponding to $\tilde{t}_{17}$ the field is near its weak maximum while at the start time corresponding to $\tilde{t}_{16}$ it is near its overall maximum, and the latter exceeds the former by a factor of two. In fact, as we decrease the field strength E_0, the peak at $\tilde{t}_{16}$ decreases much faster than the one at $\tilde{t}_{17}$. Finally, we notice a small shoulder in the $22\omega_1$-wavelet near $t_1 = 0.75T \pmod T$. This can be traced to a nonextremal trajectory (returning in this time range with a culminating point at the extremal frequency $\tilde{\Omega}_7$ in Fig. 7.2). Also for $\omega = 12\omega_1$, we recover the extremal semiclassical return times $\tilde{t}_{11}$ and $\tilde{t}_{12}$, and some groups of non-extremal return times, which are indicated in Figs. 7.2 and 7.5(b).

7.2 Phase- and intensity-dependence of the cutoffs

In this section, we investigate the dependence of the cutoff energies and their associated start and return times on the relative phase and intensity of the two driving waves and we discuss the consequences for the resulting harmonic spectra. We try to match features of the calculated spectrum to the properties of the semiclassical cut-off trajectories. While keeping the total ponderomotive energy of the field (7.1) constant we vary either the intensity ratio of the high-frequency over the low-frequency component for constant phase or vary the phase for equal and fixed field components.

7.2.1 Variation of the relative intensities

With the objective of investigating how the ratio $\eta = E_{02}/\,E_{01}$ influences the cutoff energies, we keep the ponderomotive energy and the phase ϕ fixed and equal, respectively, to $U_p = 0.31$ and $\phi = 0$. With $\varepsilon_0 = -0.4$ a.u. this yields a Keldysh parameter $\gamma = \sqrt{|\varepsilon_0|\,/2U_p} = 0.8$. For a given η, the amplitudes are, for a ω-2ω bichromatic field,

$$E_{01} = 4\omega\sqrt{\frac{U_p}{4+\eta^2}} \tag{7.3}$$

and $E_{02} = \eta E_{01}$.

Figure 7.6 shows some of the cutoff energies as functions of the field strength ratio η. First, let us consider the monochromatic case $\eta = 0$. Apart from the well-known maximal cutoff energy $\varepsilon_{\max} = |\varepsilon_0| + 3.17U_p$, additional cutoffs which correspond to longer excursion times of the electron in the continuum also exist. With the restriction $t_1 - t_0 \le 2T$, the next two cutoffs are at $\varepsilon_{1\max} = |\varepsilon_0| + 1.54U_p$ and $\varepsilon_{2\max} = |\varepsilon_0| + 2.4U_p$. All three cutoffs have almost identical start times near $t_0 = 0.3T$, while the return times are $t_1 = 0.95T$, $1.5T$ and $2.0T$, respectively. In the monochromatic case, not much attention is paid to these additional cutoffs since, due to the spreading of the electronic wave packet and rescattering effects, their contribution to harmonic generation is insignificant. However, for two-color fields, their role in the harmonic generation process is much more prominent, as we will see next.

For a monochromatic driving field proportional to $\sin 2\pi t/T$ all temporal patterns relevant to harmonic generation have a period of $T/2$. That is, if t_0 and t_1 form a pair of start and return times, then so do $t_0 + nT/2$ and $t_1 + nT/2$ for any integer n. This symmetry arises because the field satisfies $E(t + T/2) = -E(t)$, and the change of sign has no effect on harmonic generation. This is also evident from Eqs. (4.6) and (4.7) which determine the start and return times. The addition of the second field in Eq. (7.1) destroys this symmetry. As a consequence, start times t_0 and $t_0 + T/2$ no longer lead to return times t_1 and $t_1 + T/2$. Trajectories starting at t_0 and $t_0 + T/2$ are independent and lead to different kinetic energies upon return.

The consequences can be observed in Fig. 7.6 which depicts the cutoff energies as a function of the field-strength ratio η. With the addition of the second driving field, $\varepsilon_{\max}$, $\varepsilon_{1\max}$ and $\varepsilon_{2\max}$ each split into two branches. The upper branch of $\varepsilon_{\max}$ provides the highest cutoff for all values of the ratio η. The lower branch of $\varepsilon_{\max}$ almost merges with the upper branch of $\varepsilon_{1\max}$ when the ratio η approaches unity. The growth of the most energetic cutoff towards higher energies (roughly 5 U_p) is in agreement with the extension of the plateau in the bichromatic case which has been reported by several groups [89, 28, 96]. The effect is already visible with the superposition of a very weak second driving wave. In addition, a group of lower-energy cutoffs appears for values of η exceeding 0.6. Remarkably, most of them also split for increasing η.

Table III lists the expected harmonic frequencies for the cutoff at $\varepsilon_{\max}$ for several values of η, along with the respective values of the two field components. The harmonic number results from $E_{\rm kin}(t_1, t_0)/\omega_1$ with the addition of $|\varepsilon_0| = 8\hbar\omega_1$.

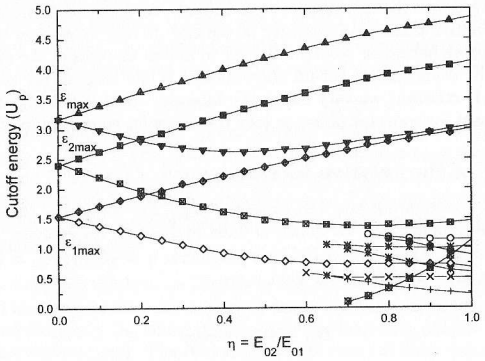

Figure 7.6: Cutoff energies as functions of the field-strength ratio η, for a ω-2ω driving field and $\phi = 0$, calculated from the semiclassical three-step model.

Table III: Field strength ratio, the respective amplitudes, and approximate harmonic frequencies for the cutoff trajectories corresponding to $\varepsilon_{\max}$.The relative phase is $\phi = 0$.

η	$E_{01} \times 10^2$	$E_{02} \times 10^2$	$(\varepsilon_{\max} + \lvert\varepsilon_0\rvert)/\omega_1$	
0	5.59	0	27.8	
0.2	5.56	1.11	30.6	25.7
0.4	5.48	2.19	33.0	24.4
0.6	5.35	3.21	35.1	24.6
0.8	5.19	4.15	36.9	25.8
1.0	5.0	5.0	38.4	27.1

In Fig. 7.7 we present the power spectra of the dipole acceleration from the solution of the TDSE, for several values of η. We observe the increase of the cutoff with $\varepsilon_{\max}$ for increasing η. The most dramatic feature is the extreme sensitivity of the power spectra against small variations in η. Extreme examples are $\Omega = 20\omega_1$ and $\Omega = 14\omega_1$, which, from $\eta = 0$ to $\eta = 0.2$ suffer a variation of roughly 5 orders of magnitude. For $\eta \neq 0$, also even harmonics are present, as expected. In part (b) we show the cutoff region in order to illustrate the splitting of the most energetic cutoff, for $\eta = 0$, 0.4 and 0.8. The corresponding cutoff energies (namely the two branches of $\varepsilon_{\max}$, as well as the upper branch of $\varepsilon_{2\max}$) are marked with arrows. In each case, the very highest cutoff $\varepsilon_{\max}$ accurately identifies the onset of the final dropoff of the plateau. The other two cutoffs are typically followed by decreasing harmonic intensities as well. Moreover, the lower one of these two cutoffs marks the position of the absolute intensity maximum of the plateau. One should bear in mind, however, that the one-dimensional calculation overemphasizes the contribution of the longer return

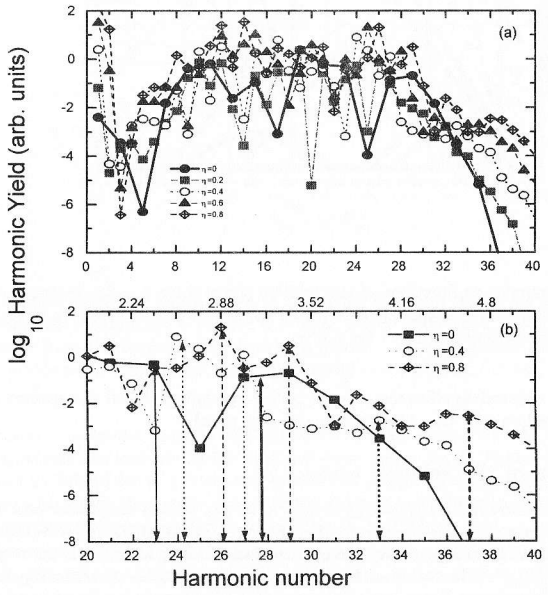

Figure 7.7: Harmonic yields calculated from the TDSE for $U_p/\omega_1 = 6.2$ and $|\epsilon_0|/\omega_1 = 8$, for different field-strength ratios η and $\phi = 0$. Part (a): complete power spectra, for all values of η displayed in Table I; part (b): high-energy part, for $\eta = 0$, $\eta = 0.4$ and $\eta = 0.8$. The three most energetic cutoffs, for respectively $\eta = 0$, $\eta = 0.4$ and $\eta = 0.8$ are indicated as solid, dashed and dotted arrows. The thickest arrows show the most energetic cutoff. The numbers on the upper edge of part (b) specify the kinetic energy upon return in multiples of U_p for the 22nd, 26th, 30th, 34th, and 38th harmonic.

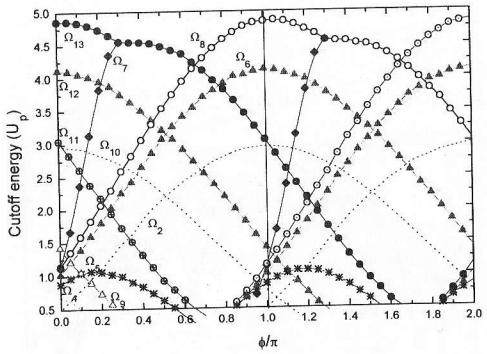

Figure 7.8: Cutoff energies as functions of the relative phase ϕ for a ω-2ω driving field with both driving waves of equal field strength, calculated from the semiclassical three-step model. The cutoff energies are labeled according to Table I for $\phi < \pi$.

times, owing to the reduced significance of wave packet spreading. In all the spectra one sees the plateau extension predicted by the three-step model very clearly.

7.2.2 Variation of the relative phase

Next we consider field strengths $E_{01} = E_{02} = 0.05$ a.u. ($\omega_1 = 0.05$ a.u.) and vary the phase ϕ. We take the field to have the same ponderomotive energy as in the previous subsection. The cutoff energies Ω_j at $\phi = 0$, in increasing order, are displayed in Table I, along with the respective start and return times (t_{0j}, t_{1j})[4]. The two branches of $\varepsilon_{\max}$, for example, are given by Ω_{13} and Ω_{11}.

Figure 7.8 exhibits the cutoff frequencies Ω_j as functions of the phase ϕ. For $\phi = 0$, the cutoff energies listed in Table I can be read off. Even though the curves merge or cross, we will keep the notation of Table I throughout. We display an entire period of 2π for the phase ϕ although the trajectories actually obey the smaller period of π: the reason lies in the symmetry $E(t, \phi + \pi) = -E(t - T/2, \phi)$ of the field (7.1) for our case $n = 2$. The change of sign has no effect on harmonic generation, and the shift by half a period just resets the clock. The labelling of the trajectories is determined within the interval $0 \leq \phi \leq \pi$. Figure 7.8 shows that due to the periodicity the trajectories $\Omega_6, \Omega_9, \Omega_{12}$ are connected. This is also the case for $\Omega_8, \Omega_{11}, \Omega_{13}$ and for $\Omega_2, \Omega_4, \Omega_{10}$. The start and return times also vary as functions of the phase, but this variation is much less dramatic than that of the corresponding kinetic energies. This can be understood by inspecting Eq.(4.6): it is the function $F(t)$ that governs the return condition (4.6) whose solutions yield pairs of start and return times. Since $F_{02} = F_{01}/4$, the return condition is not very strongly affected by the addition of the high-frequency field (and thus neither by its phase with respect to the low-frequency field).

[4]The harmonic numbers given in the 4th column of this table, however, do not apply in this subsection, since these are calculated for $\gamma = 1$. The harmonic numbers for $\gamma = 0.8$ are indicated in the lower axis of Figs. 7.7 and 7.10.

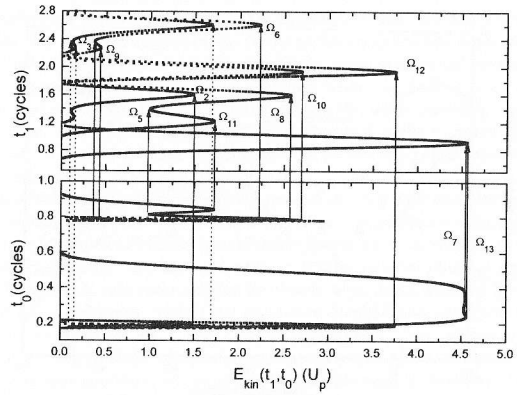

Figure 7.9: Classical start and return times as a function of return energy for an electron in a field $E(t) = 0.05[\sin(0.05t) + \sin(0.10t + \phi)]$, for $\phi = \pi/3$. Lower part: start times; upper part: return times, calculated from the semiclassical three-step model. The solid arrows connecting both parts show the extremal-energy trajectories, labeled in accordance with Fig. 7.8 and Table I.

On the other hand, the kinetic energies exhibit a much stronger influence of the high-frequency field, due to their quadratic dependence on the field and since $A_{02} = A_{01}/2$. Hence, the start and return times displayed in Table I for $\phi = 0$ can still be used as points of reference for $\phi \neq 0$. We consider only trajectories for which the kinetic energy of the electron is of the order of or larger than $0.5U_p$, so that we consider cutoff energies higher or equal to Ω_2 in Table I.

The most energetic cutoff is given by the two trajectories Ω_{13} and Ω_8 which intersect at roughly $\phi = 0.67\pi$ (modulo π). Its absolute maximum of $4.86U_p$, occurs at $\phi = 0.05\pi$. The enveloping pattern as a function of the phase ϕ for this most energetic cutoff agrees with the curve given in Ref. [28]. Interestingly, a third trajectory (Ω_7, diamonds) merges with Ω_{13} at $\phi = 0.3\pi$ (modulo π). More information about this merging can be inferred from Fig. 7.9, where the start and return times as functions of the kinetic energy of the returning electron are displayed for $\phi = 0.3\pi$ As a function of the kinetic energy $E_{\text{kin}}(t_0, t_1)$ upon return, the upper and lower parts of the figure display, respectively, the start and return times t_0 and t_1. The cutoff energies are easily identified, and we will refer to the corresponding electron trajectories as "extremal trajectories". They are marked by arrows and labeled according to the notation of Fig. 7.8. For the merging trajectories, there is an extended range of start times between $0.2T$ and $0.4T$ all of which correspond to return times near $t_1 \simeq 0.93T$, and energies near Ω_{13}.

The results stated above are in general confirmed by the numerical solution of the TDSE. We restrict ourselves to the upper part of the plateau where only few cutoff trajectories are present. In Fig. 7.10 we plot the high-energy part of the power spectra for several values of the phase in the interval $0.05\pi \leq \phi \leq 0.25\pi$. The power spectra show an overall intensity decrease of the harmonics near the cutoff by several orders of magnitude. Partly, this illustrates the decrease of the highest cutoff from $4.86U_p$ to $4.65U_p$ shown in Fig. 7.8. However, the very pronounced decrease of the

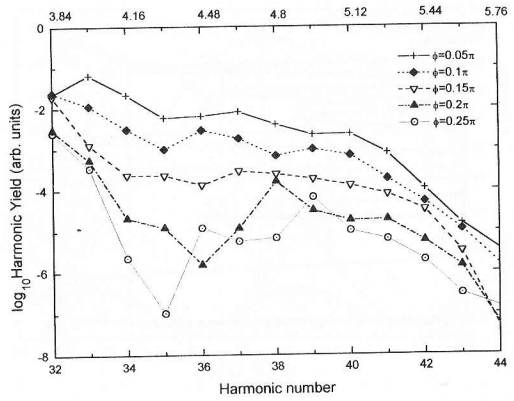

Figure 7.10: High-energy part of the harmonic yield of a ω-2ω bichromatic field with equally strong driving waves, for various relative phases $0.05\pi \leq \phi \leq 0.25\pi$, calculated from the TDSE for $E_{01} = E_{02} = 0.05$ a.u., $\omega_1 = 0.05$ a.u., and $|\epsilon_0| = 8\omega_1$ The numbers on the upper edge of the figure give the kinetic energy upon return in multiples of U_p for the respective harmonics.

harmonics around the 36th is surprising. As shown in Fig. 7.9, electrons starting at any time within $0.2T \leq t_0 \leq 0.4T$ return within a narrow range about $t_1 = 0.93T$ with an energy close to $36\omega_1$. Yet the 36th harmonic is not only not in any way enhanced (nor does a calculation of the wavelet yield show any particular concentration at this time), it is in fact strongly suppressed. The reason can be found in the fact that the electric field within this entire range of emission times is quite weak which prevents significant injection of electrons at these times. This can be inferred by inspection of the field (7.1), but is, in fact, a general consequence of the return condition (4.6). In order to have a situation like the one we consider – electrons from a whole range of start times $t_{01} \leq t_0 \leq t_{02}$ all returning at about the same time – the function $F(t_0)$ must be approximately linear within this range. Then, however, $E(t_0)$ is essentially zero, and very few electrons are set free within this range of start times. A similar situation occurs for the cutoff Ω_7 in Sec. 7.1.3.

7.3 Discussion

We have investigated harmonic production in the simplest and, possibly, practically most relevant case of a two-color driving field, namely, for two parallel linearly polarized fields with frequencies ω and 2ω. This field provides two additional parameters as compared to the standard monochromatic field: the relative phase between the two components of frequency ω and 2ω and their intensity ratio. Also for such fields, the semiclassical three-step model describes high-harmonic generation very well, in terms of its spectral and temporal profiles, and can be employed as a useful guide to the interesting regions of the parameter space with high predictive power. For instance, the cutoff structure in the spectra obtained with the TDSE results corresponds well with the extremal

energies predicted by the semiclassical three-step picture. Moreover, the main contributions to high-harmonic generation come from the classical extremal return times obtained from the classical trajectory analysis. The relative heights of the peaks in the temporal harmonic generation profile can be explained by invoking the first and second steps in the three-step model, namely emission through tunneling, which is exponentially improbable at times when the field is weak and the time delay between emission and return to the origin, which allows the wave packet to disperse the more the longer this delay time. It is surprising that *all* peaks observed in the temporal profile can be traced back to classical return times and that furthermore all prominent peaks have a simple explanation in terms of short-delay classical returns.

However, even within this simple picture, the second driving field introduces a lot of complexity. It distorts the semiclassical trajectories of the electron in the continuum, such that, in general, the number of extremal- energy trajectories considerably increases with respect to the monochromatic case, their number and energy varying with respect to the relative phase ϕ and the field-strength ratio η. In Figs. 7.6 and 7.8, this variation can be clearly seen. Each point in the figures represents a semiclassical orbit for the electron, within the three-step model framework, which yields maximal or minimal kinetic energy upon return. These "cutoff trajectories" split, merge or cross each other in a complicated way, as each of these two parameters are changed. As a consequence there are several "cutoffs" in the harmonic spectrum whose individual significance is, however, hard to predict. The question of the existence and form of the cutoff of the harmonic spectrum in the two-color case has been repeatedly discussed in the literature, that is, the question of whether there is a simple bichromatic analog of the well known $3.17U_p$ cutoff law of the monochromatic case. The results of this chapter indicate there is no simple answer. For any value of the phase ϕ and the ratio η of the two components of the field, there is, of course, a highest cutoff trajectory, but the resulting cutoff $\alpha(\eta, \phi)U_p$ is a complicated function of these two parameters. Moreover, the highest cutoff may be not the most important cutoff: a cutoff which has a lower energy may dominate the spectrum, and the higher one while visible in the spectrum just shows as a minor bump sitting on the shoulder of the former. The existence of the two additional parameters provides options of coherent control of the harmonic output. For example, we confirmed an extension of the plateau due to the addition of the high-frequency component of the driving field. Experimental confirmation of these predictions depends on efficient and reliable control of the relative phase between the two components of the driving field.

Part II

Atomic Stabilization

Chapter 8

Generalities

8.1 Introduction

For many decades, Fermi's golden rule has been successfully applied for the computation of ionization rates or probabilities of atoms in external radiation fields. In fact, until the late eighties, all external field strengths involved in such processes were much weaker than the atomic binding fields. Thus, an approach based on perturbation theory around the solution of the Schrödinger equation without the presence of the laser fields [97] is actually expected to yield reasonable results. With the advance of laser technology, however, nowadays intensities higher than $10^{21} W/cm^2$ are possible and pulses may be reduced to a duration of $\tau \sim 10^{-15} s$[1]. Such intensities are no longer in the region of validity of conventional perturbation theory - and consequently of Fermi's golden rule. This new regime is tackled by expansions around the Gordon-Volkov solution [98] of the Schrödinger equation [65, 99, 100, 101, 104, 105], fully numerical solutions of the Schrödinger equation [34, 47, 48, 50, 106, 107, 108, 109, 110, 111, 112, 113, 114], Floquet solution [115, 116, 117], high frequency approximations [19, 118, 119] or analogies to classical [120, 121, 122, 123] and semi-classical [124] dynamical systems. Some of these methods suggested there may be physical mechanisms which suppress ionization, leading to so-called "atomic stabilization". This theoretical prediction has become one of the most controversial effects related to the interaction between atoms and strong laser fields, not only concerning its definition, but even its very existence altogether. For reviews on the subject we refer to [125, 126, 127, 128].

Also the conditions for which stabilization might occur, as well as the physical mechanisms originating this phenomenon, have raised considerable debate. According to the physical mechanisms which lead to the suppression of ionization, stabilization is usually classified as:

1. *"Interference Stabilization":* In the late eighties, Parker and Stroud [129], and Fedorov and Movsesian [130] suggested that the ionization amplitudes of closely-spaced atomic Rydberg states may interfere destructively, such that ionization is suppressed. Concretely, this corresponds to a reduction of the ionization rate below Fermi's golden rule. These mechanisms are expected to be destroyed at intensities higher than $10^{14} W/cm^2$, resulting in the total ionization of the atom.

2. *"Adiabatic Stabilization":* For very high frequencies and intensities, the atom is distorted in such a way that the electron gets trapped in a dichotomous effective potential, such that ionization is suppressed. This was first suggested by Gavrila et al. [19], using the high-frequency approach. In the limit of infinite frequencies, the eigenstates of this potential are

[1] For a review and the experimental realization of such pulses see for instance [103].

orthogonal to the continuum, with no resulting ionization [118]. For finite, but high frequencies, this trapping mechanism is associated to the decrease of the ionization rate with field strength, after a critical field intensity above $10^{17} W/cm^2$ [119]. The atomic Hamiltonian was taken in the Kramers-Henneberger frame, and the dichotomous potential is the first term of the Fourier expansion of the shifted atomic potential $V(\vec{x} - \vec{c}(t))$. The other terms are negligible for very high intensities and frequencies[2]. Within this picture, stabilization has a stationary character, in the sense that it does not depend on how the field is switched on and off. In fact, criticisms concerning this theory are mainly related to its applicability to a realistic pulse, i.e., with a turn-on and off and therefore a finite bandwidth. This is an important issue, since the intensities for which stabilization is supposed to occur can only be achieved using pulsed lasers. It is commonly accepted, however, that this physical picture should be valid for pulses which are switched on adiabatically, i.e., in a time scale much longer than the field period, without suffering 100% ionization in the process [110, 126]. Some classical arguments are also used in this case, referring to a "quasi-free" electronic wave packet, which can not absorb enough photons from the field (note that a free particle does not emit or absorb photons), but is not in a continuum state.

3. *"Dynamic Stabilization"*: Computations based on the fully numerical solution of the Schrödinger equation also observed a decrease in the ionization yield after a critical field intensity of more than 1 a.u. for ultrashort pulses [109].The argument is in principle the same as above, but in this case stabilization is not regarded as a steady-state phenomenon: the electron, initially in the ground state, evolves to one or more field-dressed states. The trapping state must be achieved through an appropriate turn-on of the field [112, 122].

One should keep in mind that this classification is not completely agreed upon within the scientific community. For instance, several authors regard definition 1 as "dynamic stabilization" [50, 125], and sometimes computations using pulses with a short turn-on are related to "adiabatic stabilization", as long as the concept of an effective dichotomous potential is applicable [125]. Moreover, "interference stabilization" is sometimes only regarded as "suppression of ionization", whose physical implications are not so dramatic as those of definitions 2 and 3. In fact, the two latter subdivisions are much more counterintuitive and controversial: as stated in [126], in case such predictions are experimentally confirmed, *"a dramatic shift in viewpoint is required to explain the physics of atoms in very strong laser fields"*.

Experimentally, strong deviations from Fermi's golden rule have been observed, but the fields involved in these experiments are below the ultra-intense regime concerning the theoretical studies [20, 21]. In Fig. 8.1, we present results obtained recently by the Amsterdam group concerning the surviving population of a circular 5g Rydberg state of neon [21], in comparison with the predictions of Fermi's golden rule. In their measurement, the ionization probability seems to saturate towards a finite value, such that 70% of the bound-state population survives a field of roughly $200 TW/cm^2$. To our knowledge, this is the strongest experimental support so far for the existence of stabilization[3].

In this thesis, we will neither be concerned with the mechanisms sketched in 1-3, nor with the methods used by most groups in the investigation of stabilization. Instead, we will perform a non-orthodox analysis of this phenomenon, providing rigorous mathematical arguments for its existence or absence. Analytical methods will be used whenever possible. This is a complementary approach

[2] Mathematical conditions for this neglect were derived in [119], one of these being known as the "high-frequency condition". According to it, stabilization only occurs if the frequency of the driving field is much higher than the binding energy of the electron. For existing laser frequencies, this condition is more easily fulfilled for *highly excited states*.

[3] There is a numerical computation which presents quantitative agreement with the results of this experiment, using Floquet and the TDSE methods [131].

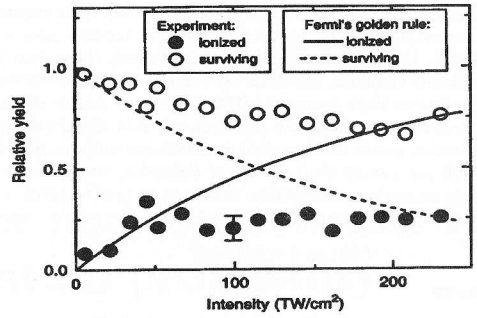

Figure 8.1: Ionized and surviving fractions of the 5g population as functions of the main pulse intensity, measured by N.J. van Druten et al [21]. The experimental results are given by the solid and open circles, and the predictions of Fermi's golden rule by the solid and dashed lines.

to most of the studies concerning stabilization, which are based on numerical treatments. Analytical arguments are desirable, since a high degree of numerical analysis may sometimes be detrimental to the interpretation of the physical conditions responsible for stabilization. Furthermore, several results have been disputed (last ref. in [109]) with regard to numerical convergence problems [105] and the possibility to allow distortions of the electron trajectory, which is believed to be necessary for the occurrence of stabilization [34].

Moreover, most discussions of stabilization refer to the physical picture of an electron trapped in a dressed atomic potential. Therefore, alternative views of the problem, presenting other physical arguments, would certainly contribute to a more complete understanding of this phenomenon.

In particular, we concentrate on the influence of the pulse shape on ionization probability. Some authors [104, 109] put forward the claim that in order to observe atomic stabilization one requires pulses which are switched on, sometimes also off, smoothly. It further appears that, among these authors, it is not commonly agreed upon, whether one should associate these pulse shapes to the laser field or to the associated vector potential. Even though there are detailed studies concerning the turn-on and off [112, 122], and even discussions of which turn-on would be most efficient, we did not find any rigorous explanation why such pulses should produce so surprising effects. Geltman [105] and also Chen and Bernstein [34] do not find evidence for stabilization for these types of pulses with smooth and turn on (and off) of the laser field. As it will become clear in this work, the existence or absence of stabilization involves deeper physical considerations, beyond the smooth switch-on and -off.

8.2 Definition

Even though the rough idea behind stabilization is the same, i.e., that atoms may survive ultra-intense laser fields, there is no agreement upon a rigorous definition of it. For some authors, "stabilization" means that the probability of ionization by a pulse of laser radiation, which for low intensities increases with increasing intensities reaches some sort of maximum at high intensities

and commences to decrease until ionization is considerably suppressed [34, 101, 105, 109, 122, 128]. Others adopt the same definition in terms of the ionization rate. Their main argument is that, since this physical quantity decreases, the average atomic lifetime must increase after a critical intensity [18, 19, 99, 102, 112, 114, 116, 118, 119]. Furthermore, some authors claim that, concerning ultrashort and adiabatically switched-on pulses, one must use respectively the ionization probability and the rate, without a justification for their statements [117, 123]. Some doubts about the rate being a well-defined concept in this intensity regime have also been raised in the literature [101, 105, 128].

Therefore, since stabilization means different things to different authors, we will precisely state our definition of it. We will not discuss the behavior of ionization rates as some authors do, but we shall consider exclusively ionization probabilities. Denoting by $\|\psi\|^2 = \langle\psi|\psi\rangle = \int |\psi(\vec{x})|^2 d^3x$ the usual Hilbert space norm, the ionization probability is defined as

$$\mathcal{P}(\psi) \;=\; 1 - \|P_+ S\psi\|^2 \quad . \tag{8.1}$$

We used the scattering matrix

$$S = \lim_{t_\pm \to \pm\infty} \exp(it_+ H_+) \cdot U(t_+, t_-) \cdot \exp(-it_- H_-) \,, \tag{8.2}$$

where $H_\pm = \lim_{t\to\pm\infty} H(t)$, ψ is a normalized bound state of H_-, $P_\pm$ is the projector onto the bound state space of $H_\pm$ and $U(t,t')$ is the time evolution operator from time t' to t associated[4] to $H(t)$. The time evolution operators may be transformed from one gauge to another by

$$U_i^a(t,t') = \mathcal{A}_{j\leftarrow i}(t) U_j^a(t,t') \mathcal{A}_{j\leftarrow i}^{-1}(t'). \tag{8.3}$$

The ionization probability $\mathcal{P}(\psi)$ is a gauge invariant quantity [134]. Note that for the gauge equivalent Hamiltonians quoted in Chapter 2 we have in general

$$\lim_{t\to\pm\infty} H_l^S(t) \neq \lim_{t\to\pm\infty} H_v^S(t) \neq \lim_{t\to\pm\infty} H_{KH}^S(t). \tag{8.4}$$

However, (recall that $b(0) = c(0) = 0$), equality in the first case holds whenever we have $b(\tau) = 0$ and in both cases when in addition $c(\tau) = 0$. We will encounter this condition of a particularly switched on and off pulse below once more as the necessary condition for the presence of what we refer to as asymptotically weak stabilization[5]. We would like to point out that this condition does not coincide necessarily with the notion of adiabatically switched on and off pulses, because we may achieve $b(\tau) = 0$ and $c(\tau) = 0$ of course also with a very rapid switch on and off. Since we are interested in the behavior of the atomic bound states $|\psi(t=0)\rangle = |\psi\rangle$ of the Hamiltonian H_l^A we should commence the discussion in (8.1) in the length gauge (in this case we have $\lim_{t\to\pm\infty} H_l^S(t) = H_l^A$) such that in our situation

$$\mathcal{P}(\psi) = 1 - \left\| P_+ U_l^S(\tau, 0)\, \psi \right\|^2 \quad . \tag{8.5}$$

Regarding the ionization probability as a function of the field amplitude E_0, stabilization means that

$$\frac{d\mathcal{P}(\psi)}{dE_0} \leq 0 \qquad \text{for} \quad \mathcal{P}(\psi) \neq 1 \tag{8.6}$$

for $E_0 \in [0, \infty)$ on a finite interval. Hence the occurrence of a saddle point does not qualify as stabilization. Also we would like to introduce some terminology in order to distinguish in (8.6) between the case of equality and strict inequality. If the former sign holds we call this behavior *"weak stabilization"* and in the latter case *"strong stabilization"*. In case weak stabilization only occurs in the limit $E_0 \to \infty$, we shall refer to it as *"asymptotically weak stabilization"*.

[4] "Associated" is to be understood in the sense that the time evolution operator obeys the Schrödinger equation $i\partial_t U(t,t') = H(t)U(t,t')$.

[5] There are doubts expressed by experimentalists about the possibility to realise pulses having simultaneously $b(\tau) = 0$ and $c(\tau) = 0$ [152].

Chapter 9

Upper and lower bonds for the ionization probability

Concerning bound-state stabilization through short-pulsed laser radiation, the standard analytical and semi-analytical methods present several limitations and drawbacks. For instance, the Volkov solution requires the binding potential to be much smaller than the external field, such that its applicability to the turn-on and off regions, where both parameters are comparable, is questionable [101, 105, 128]. Floquet computations [115, 116, 117] should work well for strictly periodic fields or very smoothly switched on and -off pulses, but are expected to get worse as these pulses get shorter. Also the high-frequency approximation [19, 118, 119], as its name says, is applicable only within a certain frequency range. These limitations, together with the fact that fully numerical computations suggested that the turn-on and off regions are important to the occurrence of stabilization, motivated the development of the method discussed in this chapter. One of the main virtues of this approach is that it may be carried out purely analytically. Moreover, it is valid for arbitrary frequency and pulse shape, including the turn-on and off regions. In different contexts it has turned out to be extremely fruitful, for instance in the proof of the stability of matter [132] and the stability of matter in a magnetic field [133]. The essence of the method consists in treating bounds which restrict a physical quantity rather than looking at its actual value.

We will provide rigorous analytic expressions for the upper and lower bound, $P_u(\psi)$ and $P_l(\psi)$, respectively, for the ionization probability in the sense that

$$P_l(\psi) \leq P(\psi) \leq P_u(\psi) \,. \tag{9.1}$$

Surely one should treat these expressions with care and be aware of their limitations in the sense that about the actual shape of $P(\psi)$ no decisive conclusion can be drawn whenever $P_l(\psi)$ differs strongly from $P_u(\psi)$. However, it seems a reasonable assumption that the analytic expression of the bounds reflect qualitatively the behavior of the precise ionization probability. Nonetheless, there exist certain type of questions in the present context which can be answered decisively with this method. Concerning the question of stabilization we may consider the bounds as functions of the field amplitude and can conclude that stabilization exists or does not exist once we find that $P_u(\psi)$ for increasing field amplitude tends to zero and $P_l(\psi)$ tends to one, respectively. Unfortunately, one does not always succeed in deriving analytic expressions which are of this restrictive form.

We would like the reader to keep in mind that the outcome of every theoretical investigation will attach some sort of error to any physical quantity. In the minority of cases this error can be precisely stated, since it may either be the consequence of various qualitative assumptions based on some physical reasoning which are difficult to quantify or it may be of a more technical nature

originating in the method used. Examples concerning analytical methods were already given in this chapter. Also concerning the fully numerical solution of the Schrödinger equation, one is forced to, for instance, discretize $H(t)$, insert the atom into a finite box, obtaining a "discrete continuum", and introduce absorbing mask functions at the boundary (we refer to Sec. 4.3 in Chapter 4 and Appendix D of this thesis for more details on this method). Even the main physical framework (i.e. non-relativity, dipole approximation, classical treatment of the external field, neglect of the magnetic field) introduces some error, which may lead to incorrect results for relativistic intensities and ultra-high frequencies. Therefore, one is *always* dealing with some form of bounds.

9.1 General expressions

We shall now briefly recall the general expressions for these bounds, derived by Fring, Kostrykin and Schrader using methods of functional analysis [134]. These expressions are valid for any bound state, arbitrary external fields and a wide range of binding potentials[1]. In order to give an idea of the estimations involved, one of these derivations is briefly sketched. We refer to [134] for more details and further derivations. In this reference, the lower bound

$$P_l(\psi) = 1 - \left\{ \int_0^\tau \|(V(\vec{\mathbf{r}} - c(t)\hat{e}_x) - V(\vec{\mathbf{r}}))\psi\| dt \right.$$
$$\left. + \frac{2}{2\varepsilon_n + b(\tau)^2}\|(V(\vec{\mathbf{r}} - c(\tau)\hat{e}_x) - V(\vec{\mathbf{r}}))\psi\| + \frac{2|b(\tau)|}{2\varepsilon_n + b(\tau)^2}\|\mathbf{p}_x\psi\| \right\}^2 \tag{9.2}$$

was obtained. This bound is valid when the classical energy transfer is larger than the ionization energy of the bound state, i.e.,$|\varepsilon_n| < b(\tau)^2/2$. Here, ε_n, $b(\tau)$ and $c(\tau)$ denote, respectively the binding energy, the momentum transfer and the classical displacement caused on the electron by the field. The wave function ψ refers to a normalized bound state of the atomic Hamiltonian H_l^A. The restriction upon $b(\tau)$ appears as a technical requirement in the computation, but in fact has a deeper physical meaning. In order to prove Eq. (9.2), one must start from Eq. (8.5), which gives the ionization probability. A lower bound for this equation corresponds to an upper bound on $\|PU_l^S(\tau,0)\psi\|$. First we write

$$\begin{aligned} \|PU_1(\tau,0)\psi\| &= \|P\mathcal{A}_{l\leftarrow KH}(t)U_{KH}^S(\tau,0)\psi\| \\ &= \|P\exp -ib(\tau)\mathbf{x}\cdot\exp ic(\tau)\mathbf{p}_x\cdot U_{KH}^S(\tau,0)\psi\| \\ &\leq \|P\exp -ib(\tau)\mathbf{x}\cdot\exp ic(\tau)\mathbf{p}_x\cdot (U_{KH}^S(\tau,0) - \exp -i\tau H_{KH}^A)\psi\| \\ &\quad + \|P\exp -ib(\tau)\mathbf{x}\cdot\exp ic(\tau)\mathbf{p}_x\cdot\psi\|. \end{aligned} \tag{9.3}$$

The first term on the r.h.s. is estimated using Du Hamel formula. This important expression gives a relation between two time evolution operators $U_i^a(t,t')$ and $U_j^b(t,t')$ associated to two different Hamiltonians $H_i^a(t)$ and $H_j^b(t)$, respectively

$$U_i^a(t,t') = U_j^b(t,t') - i\int_{t'}^{t} ds\; U_i^a(t,s)\, H_{i,j}^{a,b}(s) U_j^b(s,t'). \tag{9.4}$$

[1] The only restriction upon these is that they are "Kato potentials". This means that, if each a with $0 < a < 1$ there is a constant $b < \infty$, such that $\|V\psi\| \leq a\|-\Delta\psi\| + b\|\psi\|$ holds for all ψ in the domain $\mathcal{D}(H_0)$ of $H_0 = -\Delta/2$, see for instance [32, 137]. This guarantees that each term in the inequalities (9.2), (9.11) and (9.12) is finite. In particular the Coulomb potential and its modifications, which are very often employed in numerical computations, such as smoothed or screened Coulomb potentials, belong to this category. However, the delta-potential, which is widely used in toy-model computations, is not a Kato potential.

Here we use the notation $H_{i,j}^{a,b}(s) = H_i^a(s) - H_j^b(s)$. We take now $U_i^a(t,t') = U_{KH}^S(\tau,0)$ and $U_j^b(t,t') = \exp -i\tau H_{KH}^A$, such that $\|(U_{KH}^S(\tau,0) - \exp -i\tau H_{KH}^A)\psi\|$ is rewritten as

$$\left\| \int_0^\tau U_{KH}^S(\tau,t)[V(\vec{\mathbf{r}} - c(t)\hat{e}_x) - V(\vec{\mathbf{r}})]\exp -i(\tau - t)H_{KH}^A\cdot\psi\, dt \right\|. \tag{9.5}$$

Now, using the unitarity of $U_{KH}^S(\tau,t)$, one finds an upper bound for Eq. (9.5), given by

$$\int_0^\tau \|(V(\vec{\mathbf{r}} - c(t)\hat{e}_x) - V(\vec{\mathbf{r}}))\psi\| dt, \tag{9.6}$$

achieving the first term of the lower bound (9.2).

The second term in (9.3) is treated as follows. By assumption $PH_{KH}^A \leq 0$. Let $\delta > 0$ be arbitrary. Then $P(H_{KH}^A - \delta)^{-1}$ is a well defined operator with operator norm $\leq 1/\delta$. Hence

$$\begin{aligned} &\|P\exp -ib(\tau)\mathbf{x}\cdot\exp ic(\tau)\mathbf{p}_x\cdot\psi\| \\ =\; &\|P(H_{KH}^A - \delta)^{-1}(H_{KH}^A - \delta)\exp -ib(\tau)\mathbf{x}\cdot\exp ic(\tau)\mathbf{p}_x\cdot\psi\| \\ \leq\; &\frac{1}{\delta}\|(H_{KH}^A - \delta)\exp -ib(\tau)\mathbf{x}\cdot\exp ic(\tau)\mathbf{p}_x\cdot\psi\|. \end{aligned} \tag{9.7}$$

We now use the fact that

$$\begin{aligned} &\exp -ic(\tau)\mathbf{p}_x\cdot\exp\; ib(\tau)\mathbf{x}\cdot H_{KH}^A\cdot\exp -ib(\tau)\mathbf{x}\cdot\exp ic(\tau)\mathbf{p}_x \\ =\; &\frac{1}{2}(-i\nabla - b(\tau)\hat{e}_x)^2 + V(\vec{\mathbf{r}} - c(\tau)\hat{e}_x) \\ =\; &H_{HK}^A - b(\tau)\mathbf{p}_x + \frac{1}{2}b(\tau)^2 + V(\vec{\mathbf{r}} - c(\tau)\hat{e}_x) - V(\vec{\mathbf{r}}). \end{aligned} \tag{9.8}$$

Inserting this into (9.7) we obtain

$$\begin{aligned} \|P\exp -ib(\tau)\mathbf{x}\cdot\exp ic(\tau)\mathbf{p}_x\psi\| \;\leq\; &\frac{1}{\delta}\|(V(\vec{\mathbf{r}} - c(\tau)\hat{e}_x) - V(\vec{\mathbf{r}}))\cdot\psi\| \\ &+\frac{1}{\delta}\|(\varepsilon_n - b(\tau)\mathbf{p}_x + \frac{1}{2}b(\tau)^2 - \delta)\psi\| \end{aligned} \tag{9.9}$$

We now make the choice

$$\delta = \varepsilon_n + \frac{1}{2}b(\tau)^2 \tag{9.10}$$

which by assumption on $b(\tau)$ is > 0 and when inserted into (9.8) immediately yields the remaining two terms in the bracket of (9.7), thus concluding the proof of the lower limit.

Using similar methods, it is also possible to derive the upper bounds

$$\begin{aligned} P_u(\psi) \;=\; &\left\{ \int_0^\tau \|(V(\vec{\mathbf{r}} - c(t)\hat{e}_x) - V(\vec{\mathbf{r}}))\psi\| dt \right. \\ &\left. +|c(\tau)|\;\|\mathbf{p}_x\psi\| + \frac{2|b(\tau)|}{2\varepsilon_n + b(\tau)^2}\|\mathbf{p}_x\psi\| \right\}^2. \end{aligned} \tag{9.11}$$

and

$$\begin{aligned} P_u(\psi) \;=\; &\left\{ \int_0^\tau \|(V(\vec{\mathbf{r}} - c(t)\hat{e}_x) - V(\vec{\mathbf{r}}))\psi\| dt \right. \\ &\left. +|c(\tau)|\;\|\mathbf{p}_x\psi\| + |b(\tau)|\;\|\mathbf{x}\psi\| \right\}^2. \end{aligned} \tag{9.12}$$

The upper bound (9.11) was obtained within the restriction $|\varepsilon_n| > b(\tau)^2/2$, whereas no conditions upon the energy were needed in the derivation of (9.12).

9.2 Upper and lower bounds for the Hydrogen atom

In the following (see also [135]) we will consider a realistic example and take the potential V to be the Coulomb potential, concentrating our discussion on the Hydrogen atom. In [134], the upper and lower bounds were calculated for its ground state ψ_{100}. For increasing intensities, the lower bound increases and the existence of atomic stabilization can be excluded in the sense that the ionization probability tends to one. The shortcoming of the analysis in [134] is that definite conclusions concerning the above question may only be reached for extremely short pulses ($\tau < 1$ a.u.), which are experimentally unrealistic. In this Section, these bounds are analyzed in further detail, and we demonstrate that atomic stabilization can also be excluded for longer pulses. In this case it is well known that the binding energy for a state ψ_{nlm} is $\varepsilon_n = -\frac{1}{2n^2}$, $\|\mathbf{p}_x\psi_{n00}\|^2 = \frac{1}{3n^2}$ and $\|\mathbf{x}\psi_{n00}\|^2 = \frac{1}{3}\langle\psi_{n00}|\mathbf{r}^2|\psi_{n00}\rangle = \frac{n^2}{6}(5n^2+1)$ (see for instance [66, 138]). We will employ these relations below. In [134] it was shown, that the Hilbert space norm of the difference of the potential in the Kramers-Henneberger frame [31] and in the laboratory frame applied to the state ψ

$$N(\vec{\zeta},\psi) := \|(V(\vec{r}-\vec{\zeta}) - V(\vec{r}))\psi\| \tag{9.13}$$

is bounded by 2 when $\psi = \psi_{100}$ for arbitrary $\vec{\zeta} = c\hat{e}_x$. We shall now investigate in more detail how this function depends on c. In order to simplify notations we ignore in the following the explicit mentioning of $\hat{e}_x$. In Appendix E we present a detailed computation, where we obtain

$$N^2(c,\psi_{100}) = 2 + (1+|c|^{-1})e^{-|c|}Ei(|c|) + (1-|c|^{-1})e^{|c|}Ei(-|c|) + \frac{2}{|c|}\left(e^{-2|c|}-1\right). \tag{9.14}$$

Here $Ei(x)$ denotes the exponential integral function, given by the principal value of the integral

$$Ei(x) = -\int_{-x}^{\infty}\frac{e^{-t}}{t}\,dt \qquad \text{for} \quad x>0\ . \tag{9.15}$$

Considering now the asymptotic behavior of N, we obtain as expected $\lim_{c\to 0} N = 0$ and $\lim_{c\to\infty} N = \sqrt{2}$. Noting further that N is a monotonically increasing function of c, (one may easily compute its derivatives w.r.t. c, but we refer here only to the plot of this function in Fig. 9.1), it follows that the [134] estimate may in fact be improved to $N(c,\psi_{100}) \le \sqrt{2}$. The important thing to notice is, that since $N(c,\psi_{100})$ is an overall increasing function of c, it therefore also increases as a function of the field strength. The last term in the bracket of the lower bound $P_l(\psi)$ is a decreasing function of the field strength, while the second term does not have an obvious behavior. Hence if the first term dominates the whole expression in the bracket, thus leading to a decrease of $P_l(\psi)$, one has in principle the possibility of stabilization. We now investigate several pulse shapes for the possibility of such a behavior and analyze the expressions

$$P_l(\psi_{100}) = 1 - \left\{\int_0^\tau N(c(t),\psi_{100})dt + \frac{2N(c(\tau),\psi_{100})}{b(\tau)^2-1} + \frac{2}{\sqrt{3}}\frac{|b(\tau)|}{b(\tau)^2-1}\right\}^2 \tag{9.16}$$

$$P_u(\psi_{100}) = \left\{\int_0^\tau N(c(t),\psi_{100})dt + \frac{|c(\tau)|}{\sqrt{3}} + |b(\tau)|\right\}^2 . \tag{9.17}$$

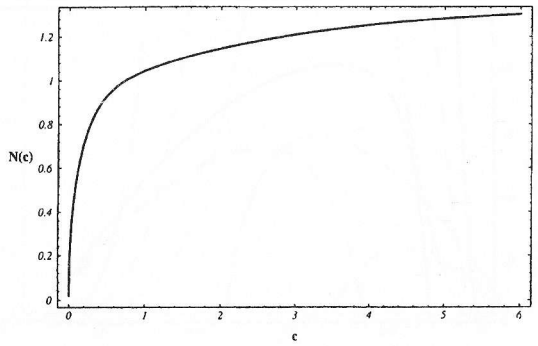

Figure 9.1: The Hilbert space norm of the difference of the potential in the Kramers-Henneberger frame and in the laboratory frame applied to the state ψ_{100} as a function of the classical displacement c.

Here we have simply inserted the explicit values for ε_1, $\|\mathbf{x}\psi_{100}\|$ and $\|\mathbf{p}_x\psi_{100}\|$ into (9.11) and (9.2), and understand $N(c,\psi_{100})$ to be given by the analytical expression (9.14). The formulae presented in Appendix E allow in principle also the computation of $N(c,\psi_{nlm})$ for different values of n, l and m. However, for $l \neq 0$ the sum over the Clebsch-Gordan coefficients becomes more complicated and due to the presence of the Laguerre polynomial of degree n in the radial wave function R_{nl} this becomes a rather complex analytical computation. We will therefore be content with a cruder analytical estimate here. In fact, we have

$$N^2(c(t),\psi_{n00}) \le 2\langle\psi_{n00}, V(\vec{\mathbf{r}})^2\psi_{n00}\rangle = \frac{4}{n^3}\ . \tag{9.18}$$

In the appendix of [134] this statement was proven for $n = 1$. The general proof for arbitrary n may be carried out along the same line. Therefore, we obtain the following new upper and lower bounds

$$P_{lw}(\psi_{n00}) = 1 - \left\{\frac{2}{n^{3/2}}\tau + \frac{4}{b(\tau)^2-1/n^2}\frac{1}{n^{3/2}} + \frac{1}{n\sqrt{3}}\frac{2|b(\tau)|}{b(\tau)^2-1/n^2}\right\}^2 \tag{9.19}$$

$$P_{uw}(\psi_{n00}) = \left\{\frac{2}{n^{3/2}}\tau + \frac{|c(\tau)|}{n\sqrt{3}} + n\sqrt{\frac{5n^2+1}{6}}|b(\tau)|\right\}^2, \tag{9.20}$$

which are "weaker" than (9.17) and (9.16), in the sense that

$$P_{lw}(\psi_{n00}) \le P_l(\psi_{n00}) \le P(\psi_{n00}) \le P_u(\psi_{n00}) \le P_{uw}(\psi_{n00})\ . \tag{9.21}$$

In order for (9.19) to be valid we must have $b(\tau)^2 > \frac{1}{n^2}$. We will now turn to a detailed analysis of these bounds by looking at different pulses. The main purpose for considering states of the type ψ_{nlm} with $n \neq 1$ is to extend our discussion to pulses with longer duration. The reason that longer pulse durations are accessible for states with higher n is the n-dependence in estimate (9.18) and its effect in (9.20) and (9.19).

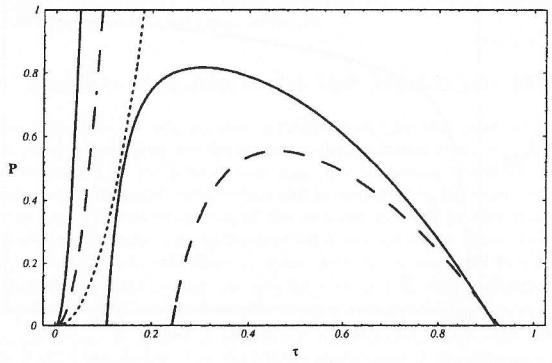

Figure 9.2: Upper (three curves on the left) and lower bound (P_u and P_l) for the ionization probability of the $\psi_{1\ 00}$ state through a static laser field E_0 as functions of the pulse length τ. The dotted, dashed and solid curves corresponds, respectively, to $E_0 = 5$ a.u., $E_0 = 10$ a.u. and $E_0 = 20$ a.u.

9.2.1 Static Field

This is the simplest case, but still instructive to investigate since it already contains the general feature which we will observe for more complicated pulses. It is furthermore important to study, because it may be viewed as the background which is present in most experimental setups, before more complicated pulses can be generated. For a static field of intensity $I = E_0^2$ we have

$$E(t) = E_0 \qquad b(t) = E_0 t \qquad c(t) = \frac{E_0 t^2}{2} \tag{9.22}$$

for $0 \leq t \leq \tau$. Inserting these functions into (9.16) we may easily compute the upper and lower bound. Here the one dimensional integrals over time, appearing in (9.17) and (9.16) were carried out numerically. The result is presented in Fig. 9.2, which shows that a bound for higher intensities always corresponds to a higher ionization probability. The overall qualitative behavior clearly indicates that for increasing field strength the ionization probability also increases and tends to one. In particular lines for different intensities never cross each other. Surely the shown pulse lengths are too short to be realistic and we will indicate below how to obtain situations in which conclusive statements may be drawn concerning longer pulse durations. In the following we will always encounter the same qualitative behavior.

9.2.2 Linearly polarized monochromatic light (LPML)

Now we have

$$E(t) = E_0 \sin(\omega t) \qquad b(t) = \frac{2E_0}{\omega} \sin^2\left(\frac{\omega t}{2}\right) \qquad c(t) = \frac{E_0}{\omega^2}\left(\omega t - \sin(\omega t)\right) \tag{9.23}$$

for $0 \leq t \leq \tau$. The result of the computation which employs these functions in order to compute (9.16) and (9.17) is illustrated in Fig. 9.3. Once again our bounds indicate that for increasing

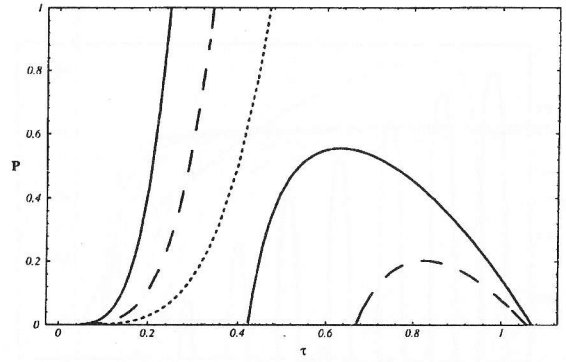

Figure 9.3: Upper (three curves on the left) and lower bound (P_u and P_l) for the ionization probability of the $\psi_{1\ 00}$ state through a linearly polarized monochromatic laser field $E(t) = E_0 \sin(\omega t)$, with $\omega = 1.5$ a.u. as functions of the pulse length τ. The dotted, dashed and solid curves correspond, respectively, to $E_0 = 5$ a.u., $E_0 = 10$ a.u. and $E_0 = 20$ a.u.

field strength the ionization probability also increases. Keeping the field strength fixed at $E_0 = 2$ a.u., a comparison between the case for $\omega = 0.4$ and $\omega = 4$ shows (Fig. 9.4), as expected, the lower bounds for the ionization probability to be decreasing functions of the frequency. The peak on the left, which seems to contradict this statement for that region, is only due to the fact that the expression for the lower bound is not valid for $\omega = 0.4$ in that regime. Clearly, this is not meant by stabilization, since for this to happen we require fixed frequencies and we have to analyze the behaviour for varying field strength. The claim [19, 109, 118, 119] is that in general very high frequencies are required for this phenomenon to emerge. Our analysis does not support stabilization for any frequency. As mentioned above, the shortcoming of the analysis of the bounds $P_u(\psi_{100})$ and $P_l(\psi_{100})$ is that we only see an effect for times smaller than one atomic unit. Figs. 9.4 and 9.5 also show that by considering $P(\psi_{n00})$ for higher values of n our expressions allow also conclusions for longer pulse durations. For the reasons mentioned above, in this analysis we employed the slightly weaker bounds (9.20) and (9.19).

9.2.3 LPML with a trapezoidal enveloping function

We now turn to the simplest case of a pulse which is adiabatically switched on and off. These types of pulses are of special interest since many authors observed (see, e.g., [109, 110, 112, 104]) that stabilization only occurs in these cases. We consider a pulse of duration τ_0 which has linear turn-on and turn-off ramps of length T. Then

$$E(t) = E_0 \sin(\omega t) \begin{cases} \frac{t}{T} & \text{for} \quad 0 \leq t \leq T \\ 1 & \text{for} \quad T < t < (\tau_0 - T) \\ \frac{(\tau_0 - t)}{T} & \text{for} \quad (\tau_0 - T) \leq t \leq \tau_0 \end{cases} \tag{9.24}$$

$$b(\tau_0) = \frac{E_0}{\omega^2 T}\left\{\sin(\omega T) - \sin(\omega\tau_0) + \sin(\omega(\tau_0 - T))\right\} \tag{9.25}$$

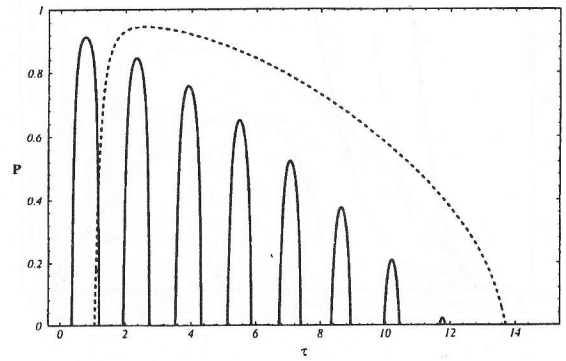

Figure 9.4: Lower bound (P_{lw}) for the ionization probability of the $\psi_{10\ 00}$state through a linearly polarized laser field $E(t) = E_0 \sin(\omega t)$, with $E_0 = 2$ a.u. as a function of the pulse length τ. The dotted and solid curves correspond, respectively, to $\omega = 0.4$ a.u. and $\omega = 4$ a.u.

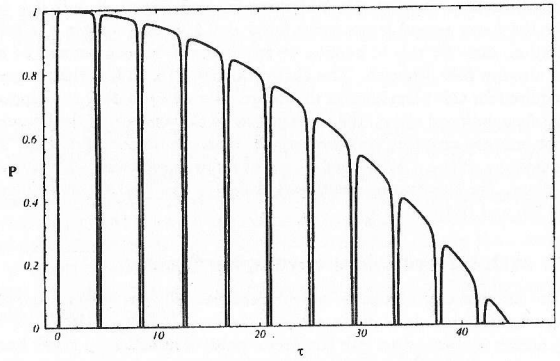

Figure 9.5: Lower bound (P_{lw}) for the ionization probability of the $\psi_{20\ 00}$state through a linearly polarized laser field $E(t) = E_0 \sin(\omega t)$, with $E_0 = 20$ a.u. and $\omega = 1.5$ a.u. as a function of the pulse length τ.

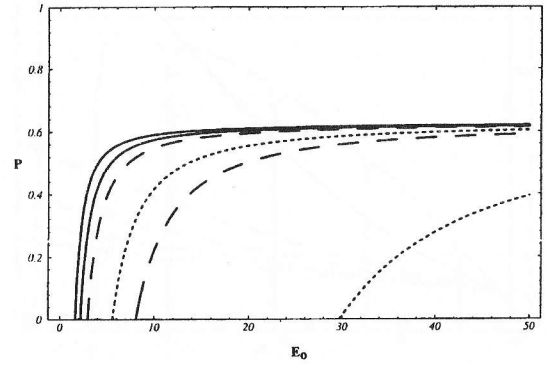

Figure 9.6: Lower bound for the ionization probability of the $\psi_{34\ 00}$-state through a linearly polarized monochromatic laser field with a trapezoidal (upper curves of different line types) and a sine-squared (lower curves) turn-on and off enveloping function, with frequency $\omega = 1.5$ a.u. Solid lines: $\frac{5}{4} - 12 - \frac{5}{4}$ pulse; dashed line: $\frac{9}{4} - 10 - \frac{9}{4}$ pulse; dotted line: $\frac{17}{4} - 6 - \frac{17}{4}$ pulse.

$$c(\tau_0) = \frac{E_0}{\omega^3 T}\Big(2 - 2\cos(\omega T) + 2\cos(\omega\tau_0) - 2\cos(\omega(\tau_0 - T)) - \omega T\sin(\omega T) + \omega\tau_0\sin(\omega T) + \omega T\sin(\omega(\tau_0 - T))\Big) \quad (9.26)$$

The expressions for $b(t)$ and $c(t)$ are rather messy and will not be reported here since we only analyze the weaker bounds. Notice that now, in contrast to the previous cases, both $b(\tau_0)$ and $c(\tau_0)$ may become zero for certain pulse durations and ramps. We choose the ramps to be of the form $T = \left(m + \frac{1}{4}\right)\frac{2\pi}{\omega}$ (m being an integer) for the lower and $T = \left(m + \frac{1}{2}\right)\frac{2\pi}{\omega}$ for the upper bound[2]. Our lower bound does not permit the analysis of half cycles since then $b(\tau_0) = 0$. The results are shown in Figs. 9.6 and 9.7, which both do not show any evidence for stabilization. They further indicate that a decrease in the slopes of the ramps with fixed pulse duration, leads to a smaller ionization probability. Once more (we do not present a figure for this, since one may also see this from the analytical expressions), an increase in the frequency leads to a decrease in the lower bound of the ionization probability for fixed field strength.

9.2.4 LPML with a sine-squared enveloping function

Here we consider a sinus squared enveloping function for the laser field, of frequency $\Omega \ll \omega$.

$$E(t) = E_0 \sin^2(\Omega t)\sin(\omega t) \quad (9.27)$$

[2] Concerning the figures of this and the next subsection, we sometimes adopt a specific terminology to this field of research, referring to a $c_1 - m - c_2$ pulse, where c_i are rational numbers and m an integer. This should be understood as a pulse which is switched on and off smoothly within respectively c_1 and c_2 field cycles, its amplitude being kept constant over m cycles.

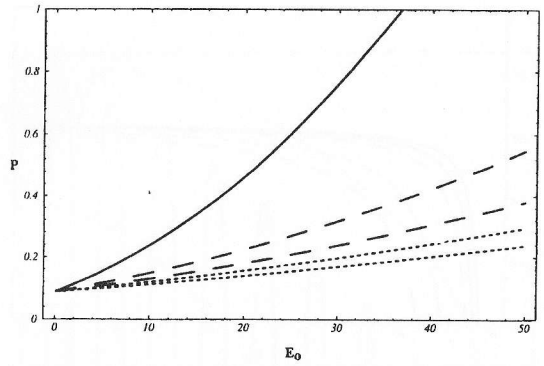

Figure 9.7: Upper bound P_{uw} for the ionization probability of the $\psi_{34\ 00}$-state through a linearly polarized monochromatic laser field with a trapezoidal (upper curves of the same line type) and a sine-squared (lower curves) turn-on and off enveloping function, with frequency $\omega = 1.5$ a.u. Solid lines: $\frac{1}{2} - 6 - \frac{1}{2}$ pulse; dashed line: $\frac{3}{2} - 4 - \frac{3}{2}$ pulse; dotted line: $\frac{5}{2} - 2 - \frac{5}{2}$ pulse.

$$
\begin{aligned}
b(t) &= \frac{E_0}{16\,\omega\,\Omega^2 - 4\,\omega^3}\Big(8\,\Omega^2 + 2\omega^2\,\cos(\omega\,t) - 8\,\Omega^2\,\cos(\omega\,t) \\
&\quad -\omega^2\,\cos((\omega - 2\,\Omega)\,t) - 2\,\omega\,\Omega\,\cos((\omega - 2\,\Omega)\,t) \\
&\quad -\omega^2\,\cos((\omega + 2\,\Omega)\,t) + 2\,\omega\,\Omega\,\cos((\omega + 2\,\Omega)\,t)\Big) \qquad (9.28)\\
c(t) &= \frac{E_0}{4\omega^2\,(\omega - 2\,\Omega)^2\,(\omega + 2\,\Omega)^2}\Big(-8\omega^3\,\Omega^2\,t + 32\omega\,\Omega^4\,t - 2\omega^4\,\sin(\omega\,t) \\
&\quad +16\omega^2\,\Omega^2\,\sin(\omega\,t) - 32\,\Omega^4\,\sin(\omega\,t) - \omega^4\,\sin((2\,\Omega - \omega)\,t) \\
&\quad -4\omega^3\,\Omega\,\sin((2\,\Omega - \omega)\,t) - 4\omega^2\,\Omega^2\,\sin((2\,\Omega - \omega)\,t) \\
&\quad +\omega^4\,\sin((\omega + 2\,\Omega)\,t) - 4\omega^3\,\Omega\,\sin((\omega + 2\,\Omega)\,t) \\
&\quad +4\omega^2\,\Omega^2\,\sin((\omega + 2\,\Omega)\,t)\Big) \qquad (9.29)
\end{aligned}
$$

for $0 \le t \le \tau$. At first sight it appears that both $b(t)$ and $c(t)$ are singular at $\omega = \pm 2\Omega$, which of course is not the case since both functions are bounded as one may easily derive. With the help of the Schwarz inequality applied on (9.28) and (9.29), it follows that always $|b(t)| \le t^{\frac{1}{2}}\,\|E_0\|$ and $|c(t)| \le \frac{1}{2}t^{\frac{3}{2}}\,\|E_0\|$. We first investigate the situation in which this pulse is switched on smoothly but turned off abruptly. Figure 9.8 shows that the bounds become nontrivial for times larger than one atomic unit in the same fashion as in the previous cases by considering $P_i(\psi_{n00})$ for higher values of n. Figure 9.9 shows that also in this case the ionization probability tends to one and no sign for stabilization is found. Figure 9.10 shows the lower bound in which the pulse length is taken to be a

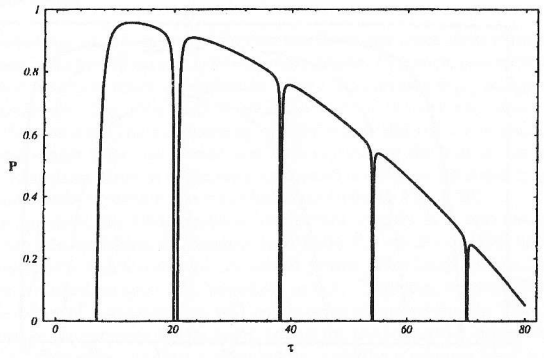

Figure 9.8: Lower bound for the ionization probability of the $\psi_{30\ 00}$-state through a linearly polarized monochromatic laser field with a trapezoidal (upper curves of different line types) and a sine-squared (lower curves) turn-on and off enveloping function, with frequency $\omega = 1.5$ a.u. Solid lines: $\frac{5}{4} - 12 - \frac{5}{4}$ pulse; dashed line: $\frac{9}{4} - 10 - \frac{9}{4}$ pulse; dotted line: $\frac{17}{4} - 6 - \frac{17}{4}$ pulse.

half cycle of the enveloping function. Once more it indicates increasing ionization probability with increasing field strength and also for increasing values for n. Following now Geltman [105] and Su et al. [109] we employ the sine-square only for the turn-on and off and include a plateau region into the pulse shape. Then

$$
E(t) = E_0 \sin(\omega t)\begin{cases} \sin^2\left(\frac{\pi t}{2T}\right) & \text{for} \quad 0 \le t \le T \\ 1 & \text{for} \quad T < t < (\tau_0 - T) \\ \sin^2\left(\frac{\pi(\tau_0 - t)}{2T}\right) & \text{for} \quad (\tau_0 - T) \le t \le \tau_0 \end{cases} \qquad (9.30)
$$

$$
b(\tau_0) = \frac{E_0\,\pi^2\,(1 + \cos(\omega\,T) - \cos(\omega\,(T - \tau_0)) - \cos(\omega\,\tau_0))}{2\,\omega\,\pi^2 - 2\,\omega^3\,T^2} \qquad (9.31)
$$

$$
\begin{aligned}
c(\tau_0) &= \frac{E_0\,\pi^2 2\omega^2}{(\pi^2 - \omega^2\,T^2)^2}\,(\omega\,\pi^2\,\tau_0 - \omega^3\,T^2\,\tau_0 - \omega\,\pi^2\,T\,\cos(\omega\,T) + \omega^3\,T^3\,\cos(\omega\,T) \\
&\quad + \omega\,\pi^2\,\tau_0\,\cos(\omega\,T) - \omega^3\,T^2\,\tau_0\,\cos(\omega\,T) - \omega\,\pi^2\,T\,\cos(\omega\,(T - \tau_0)) \\
&\quad + \omega^3\,T^3\,\cos(\omega\,(T - \tau_0)) + \pi^2\,\sin(\omega\,T) - 3\omega^2\,T^2\,\sin(\omega\,T) \\
&\quad + \pi^2\,\sin(\omega\,(T - \tau_0)) - 3\omega^2\,T^2\,\sin(\omega\,(T - \tau_0)) - \pi^2\,\sin(\omega\,\tau_0) \\
&\quad + 3\omega^2\,T^2\,\sin(\omega\,\tau_0))\ . \qquad (9.32)
\end{aligned}
$$

(Also in these cases the apparent poles in $b(\tau_0)$ and $c(\tau_0)$ for $\omega = \pm\frac{\pi}{T}$ are accompanied by zeros.) The results of this computations are shown in Figs. 9.6 and 9.7, once more with no evidence for bound-state stabilization. A comparison with the linear switch on and off shows that the ionization probability for sine-squared turn-on and offs is lower. The effect is larger for longer ramps.

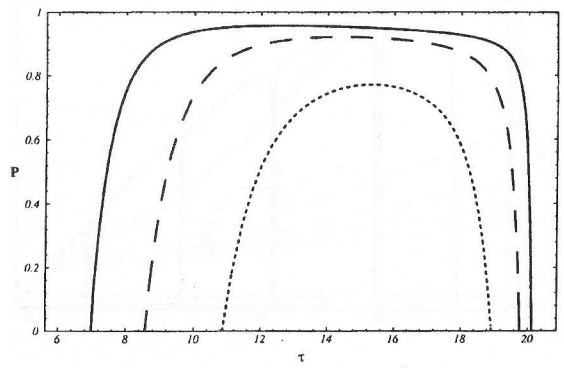

Figure 9.9: Lower bound (P_{lw}) for the ionization probability of the $\psi_{30\ 00}$state through a linearly polarized monochromatic laser field with a sine-squared enveloping function, $E(t) = E_0 \sin(\omega t)\sin^2(\Omega t)$, $\omega = 0.2$ a.u., $\Omega = 0.01$ a.u. The dotted curve corresponds to $E_0 = 5$ a.u., the dashed curve to $E_0 = 10$ a.u. and the solid curve to $E_0 = 20$ a.u.

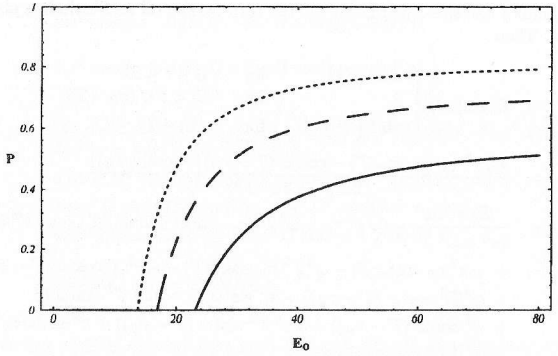

Figure 9.10: Lower bound (P_{lw}) for the ionization probability of the $\psi_{n\ 00}$state through a linearly polarized monochromatic laser field with a sine-squared enveloping function, $E(t) = E_0 \sin(\omega t)\sin^2(\Omega t)$, $\omega = 0.8$ a.u., $\Omega = \omega/13.5$. The dotted curve corresponds to $n = 40$, the dashed curve to $n = 35$ and the solid curve to $n = 30$.

9.3 Discussion

We have investigated the ionization probability for the Hydrogen atom when exposed to ultra-intense shortly pulsed laser radiation of various types of pulse shapes. In comparison with [134], we extended our analysis to the situation which is applicable to any bound-state ψ_{nlm} and in particular for the ψ_{100}-state we carried out the computation until the end for the stronger upper (9.17) and lower (9.16) bounds. We overcome the shortcoming of [134] which did not allow definite statements for pulses of durations longer than one atomic unit by investigating the bounds for higher values of n. As our computations show, there is of course a quantitative different behavior for different values of n. However, qualitatively we obtain the same behavior (refer to Fig. 9.10).

For the situation when the total classical momentum transfer $b(\tau)$ and the total classical displacement $c(\tau)$ are non-vanishing we confirm once more the results of [134] and do not find any evidence for bound-state stabilization for ultrashort pulses. This holds for various types of pulses, whether they are switched on (and off), smoothly or not. Therefore, smooth pulses in general will only prolong the onset of ionization but will not provide a mechanism for stabilization. Another interesting feature is the increase of the lower bound for the ionization probability with principal quantum number. This is in apparent contradiction with the statement that stabilization should occur more easily for Rydberg states.

We would like now to comment on pulses with vanishing momentum transfer. Even though our lower bound is not applicable under this condition (in the sense that then the condition $\frac{1}{2}b^2(\tau) > |\varepsilon_n|$ is not fulfilled), we are still able to draw some conclusions.

For pulses switched on and off such that $b(\tau) = 0$, but $c(\tau) \neq 0$, our bounds do not allow any definite statement, since the lower bound is not applicable and the upper bound gives for typical values of the frequency and field strength ionization probabilities larger than one. These types of pulses are extensively used in the literature (for instance in [104, 109, 111]). Therefore, it would be very interesting to find alternative expressions for the upper and lower bound which allow conclusions on this case.

For the case $b(\tau) = c(\tau) = 0$ the upper bound P_u remains an increasing function of the field strength due to the properties of the Hilbert space norm of the difference of the potential in the Kramers-Henneberger frame and in the laboratory frame applied to the state ψ_{100}. The weaker upper bound takes on the value $P_{uw}(\psi_{n00}) = \frac{4\tau^2}{n^3}$, which implies that the upper bound *decreases* with increasing n, i.e. for states close to the ionization threshold, and fixed τ[3]. Classically, this apparently counterintuitive behavior can be intuitively understood. For closed Kepler orbits, i.e. ellipses, with energies sufficiently close to zero (depending on τ), for any pulse with small $b(\tau)$ and $c(\tau)$, these quantities will be very close to the actual changes, caused by the pulse, of the momentum and the coordinate, respectively. So in this case ionization, i.e. the transition to a hyperbolic or parabolic orbit will therefore be very unlikely. These results are in perfect accordance with the findings that precisely the highly excited states should stabilize, and suggest that the momentum transfer delimits regions of different physical behavior. In fact, vanishing momentum transfer at the end of the pulse was pointed out in [121] as a necessary condition for the occurrence of stabilization using classical arguments. Also in the investigations in [136] stabilization is found for this case, however with the additional condition $c(\tau) = 0$. A detailed analysis allowing for all possible values of $b(\tau)$ and $c(\tau)$ using entirely different methods will be presented in Chapter 10.

In principle, it is possible to carry out our analysis further and also investigate the influence of varying the quantum numbers l and m on the ionization probability, in order to compare with existing results in the literature [111, 139]. However, due to the sum in (E.6) the explicit expressions will be rather messy and we will therefore omit them here.

[3] The same dependence with the principal number was observed in [111] in a three-dimensional TDSE computation for Hydrogen.

Chapter 10

Momentum transfer, classical displacement and stabilization

In the previous chapter, we confirmed the results of [134] that stabilization is always absent for non-vanishing momentum transfer at the end of the pulse. These features neither depend on the pulse shape nor on its frequency. For the case $b(\tau) = 0$, the method used did not allow any decisive conclusion concerning stabilization. However, the results in Chapter 9 already indicate that the momentum transfer and the classical displacement delimit regions of different physical behavior concerning ionization. In particular, a suppression of ionization was observed when these two quantities vanish at the end of the pulse. In fact, investigations of the ionization probability in the ultra-extreme limit, i.e., when the field strength is taken to infinity, found, under the condition $b(\tau) = c(\tau) = 0$, what we call "asymptotically weak stabilization" [136]. Despite the fact that in this regime one should commence with a relativistic treatment, our physical framework, that is the Schrödinger equation (2.1) remains self-consistent, and should represent the overall behavior. Moreover, it suggests that for finite, but high enough intensities for which (2.1) can still be applied, the ionization probability may in practice saturate with the external field strength towards a finite value smaller than one. This extremely counterintuitive behavior, which also qualitatively corresponds to the experimental findings of N.J. van Druten et al., [21], motivated the investigation in this chapter.

We took a concrete example in order to investigate whether the same features might be recovered. We consider one-dimensional atomic models with attractive delta potentials in the presence of intense very shortly pulsed laser radiation. Both independent general non-perturbative as well as perturbative arguments and the analysis of the explicit analytic expressions demonstrate that weak stabilization occurs when both the total classical momentum transfer and the total classical displacement vanish simultaneously. The effect is relatively stable towards small variations of the displacement, but more sensitive towards changes of the momentum transfer away from zero.

10.1 The Gordon-Volkov (GV) perturbation theory

In the high intensity regime for the radiation fields, the basic assumption for the validity of conventional perturbation theory breaks down, i.e. that the absolute value of the potential is large in comparison with the absolute value of the field. However, there is a replacement for this, the so-called Gordon-Volkov (GV) perturbation theory [98]. Since the basic idea is simple, it makes this approach very attractive. Instead of constructing the power series, either for the fields or for the time evolution operator, out of the solution for the Schrödinger equation involving the field-free

atomic Hamiltonian H_l^A and regarding $\mathbf{x}E(t)$ as the perturbation, one constructs the series out of solutions involving the Hamiltonian H_l^{GV} of an unbound particle in the field and treats the potential V as the perturbation.

The starting point in this analysis is the Du Hamel formula (9.4), whose formal iteration yields the perturbative series

$$U_i^a(t,t') = \sum_{n=0}^{\infty} U_{i,j}^{a,b}(n|t,t') \quad . \tag{10.1}$$

We introduced the quantity $U_{i,j}^{a,b}(n|t,t')$ relating to the time evolution operator order by order in perturbation theory, i.e. $U_{i,j}^{a,b}(0|t,t') = U_j^b(t,t')$, $U_{i,j}^{a,b}(1|t,t') = i\int_{t'}^t ds\, U_j^b(t,s)\, H_{i,j}^{a,b}(s) U_j^b(s,t')$. Taking therefore $i=j$ and in addition $a=S$ and $b=GV$ we obtain

$$U_i^S(t,t') = U_i^{GV}(t,t') + U_{i,i}^{S,GV}(1|t,t') + \ldots \tag{10.2}$$

In this case we need $H_{l,l}^{S,GV}(t) = H_{v,v}^{S,GV}(t) = V(\vec{\mathbf{r}})$, $H_{KH,KH}^{S,GV}(t) = V(\vec{\mathbf{r}} - c(t)\hat{e}_x)$ and the Gordon-Volkov time evolution operator, which in the KH-frame equals the free-particle evolution operator in the length gauge

$$U_{KH}^{GV}(t,t') = U_l^0(t,t') = e^{-i(t-t')\frac{\mathbf{p}^2}{2}}. \tag{10.3}$$

The expressions for the Gordon-Volkov time evolution operator in the length and velocity gauge may then simply be obtained from (10.3) by the application of the gauge transformations (2.7)-(2.8) discussed in Chapter 2 according to the transformation (8.3) concerning the time-evolution operator. The choice $i=j$ together with $a=S$ and $b=A$ in the Du Hamel formula (9.4) yields the usual perturbation series, which is well known from the low intensity regime. Surely, care has to be taken concerning the question of convergence the Gordon-Volkov series. In particular if one has oscillating laser fields, there will always be regions in which the potential in absolute value is still larger than the fields. Also for instance the Coulomb potential may be larger in absolute value than the electrical field near the origin. A systematic analysis of this problem does not yet exist, but there are some partial results, see for instance [100].

There are some results which may be derived from the perturbative expression, one concerning the ultra-extreme intensity limit $E_0 \to \infty$ used in [136] and the other the ultra-extreme high frequency limit $\omega \to \infty$ (a slightly milder assumption was used in the seminal paper [19] which formulates the high frequency approach). Both results are simple consequences of the Riemann-Lebesgue theorem[1], which is applicable if the laser field is of frequency ω modulated with an arbitrary enveloping function (we only demand that $g(t)$ is integrable)

$$E(t) = E_0 \sin(\omega t) g(t). \tag{10.4}$$

For infinite frequencies we obtain

$$\lim_{\omega\to\infty} \mathcal{A}_{l\leftarrow KH}(t) = \lim_{\omega\to\infty} \mathcal{A}_{v\leftarrow KH}(t) = 1 \tag{10.5}$$

such that with (10.3)

$$\lim_{\omega\to\infty} U_l^{GV}(t,t') = \lim_{\omega\to\infty} U_v^{GV}(t,t') = U_l^0(t,t') = e^{-i(t-t')H_l^0}. \tag{10.6}$$

Since the atomic potential is independent of E_0 we obtain with (10.6) that the entire Gordon-Volkov series (10.1) is independent of the field amplitude as well, such that

$$\frac{d}{dE_0}\left(\lim_{\omega\to\infty} \mathcal{P}(\psi)\right) = 0 \quad . \tag{10.7}$$

[1] If $g(x) \in L_1(-\infty,\infty)$ (i.e. $|g(x)|$ is integrable) then $\lim_{t\to\pm\infty} \int_{-\infty}^{\infty} g(x) e^{-itx} dx = 0$.

We have therefore weak stabilization in this ultra-extreme high frequency limit for all systems for which (10.1) makes sense and for which the laser field is of the form (10.4). One should keep in mind that the use of the Stark Hamiltonian in (2.1) assumes the validity of the dipole approximation, such that the limit $\omega \to \infty$ only makes formally sense. In order to describe real physics in this frequency regime one should actually also take multipole terms into account.

Concerning the ultra-extreme intensity limit, we consider the transition amplitude between two bound states $\psi_i(\vec{x})$, $\psi_j(\vec{x})$ of the Hamiltonian H_l^A perturbatively

$$\begin{aligned} &\langle\psi_i|U_l^S(\tau,0)|\psi_j\rangle = \langle\psi_i|A_{KH\leftarrow l}(\tau)U_{KH}^S(\tau,0)|\psi_j\rangle \\ &= \langle\psi_i|A_{KH\leftarrow l}(\tau)U_{KH}^{GV}(\tau,0)|\psi_j\rangle + \left\langle\psi_i|A_{KH\leftarrow l}(\tau)U_{KH,KH}^{S,GV}(1|\tau,0)|\psi_j\right\rangle + \ldots \end{aligned} \tag{10.8}$$

Recall that $a(0) = b(0) = c(0) = 0$, such that $A_{l\leftarrow KH}(0) = 1$. Using now (10.3) it is clear that to zeroth order we obtain

$$\left\langle\psi_i(\vec{x})|e^{-i\tau H_l^0}|\psi_j(\vec{x})\right\rangle \quad , \tag{10.9}$$

when $b(\tau) = c(\tau) = 0$. In all other cases we may bring this term into a form suitable for the application of the Riemann-Lebesgue theorem, such that the zeroth order matrix element always vanishes in the ultra-extreme intensity limit. For the higher order terms the argument is analogous with the difference that the condition $b(\tau) = c(\tau) = 0$ does not have the consequence that these expressions become independent of E_0, since also terms like $b(t), c(t)$ for $0 < t < \tau$ appear. Hence by the application of the Riemann-Lebesgue theorem all higher order terms vanish in the limit $E_0 \to \infty$. If we now sum over all bound states i in (10.8) we obtain the results of [136].

We shall now use the Gordon-Volkov approach in more specific problems. We take the Gordon Volkov and Schrödinger Hamiltonians in the length gauge, and write the Du Hamel formula (9.4) as

$$U_l^S(t,t') = U_l^{GV}(t,t') - i\int_{t'}^{t} ds\, U_l^{GV}(t,s)\, V U_l^S(s,t') \quad . \tag{10.10}$$

The operator equation (10.10) may of course be used in both configuration and momentum space, as well as (10.1). It will turn out below that for our purposes the explicit computations are in general easier to perform in momentum space. Acting now with (10.10) upon a solution $\langle\vec{p}|\psi(t)\rangle = \psi(\vec{p},t)$ of the Schrödinger equation (2.1) in the momentum representation, we obtain the following integral equation for $\psi(\vec{p},t)$

$$\psi(\vec{p},t) = \psi_{GV}(\vec{p},t) - i\int_0^t ds \int d\vec{p}_1 \int d\vec{p}_2 U_l^{GV}(\vec{p},t;\vec{p}_2,s)\, V(\vec{p}_1,\vec{p}_2)\psi(\vec{p}_2,s) \ . \tag{10.11}$$

With the help of the transformation $U_l^{GV}(t,t') = \mathcal{A}_{l\leftarrow KH}(t)e^{-i(t-t')\frac{\mathbf{p}^2}{2}}\mathcal{A}_{l\leftarrow KH}^{-1}(t')$, the Gordon-Volkov time evolution operator in the momentum representation acquires the well-known form

$$\begin{aligned} U_{GV}(\vec{p},t;\vec{p}_1,s) &= \langle\vec{p}\,|A(t)U_0(t,s)A(s)^{-1}|\,\vec{p}_1\rangle \\ &= e^{ia_{st}}e^{ic_{ts}(p_x-b(t))}e^{-\frac{i}{2}(\vec{p}-b(t)\hat{e}_x)^2(t-s)}\delta(\vec{p}-\vec{p}_1-b_{ts}\hat{e}_x). \end{aligned} \tag{10.12}$$

For convenience we introduced the notation $a_{ts} = a(t) - a(s)$, which we employ throughout and analogously for b and c. The Gordon-Volkov wave function is chosen in such a way, that it takes on the value of the bound state $\psi(\vec{p},t=0)$ of the Hamiltonian H_l^A as the initial value

$$\begin{aligned} \psi_{GV}(\vec{p},t) &= \int d\vec{p}_1 U_{GV}(\vec{p},t;\vec{p}_1,0)\,\psi(\vec{p}_1) \\ &= e^{-ia(t)}e^{ic(t)(p_x-b(t))}e^{-\frac{i}{2}t(\vec{p}-b(t)\hat{e}_x)^2}\psi(\vec{p}-b(t)\hat{e}_x). \end{aligned} \tag{10.13}$$

Notice that sometimes the $\vec{p}_1$ and $\vec{p}_2$ integration in (10.11) may be carried out analytically, such that, upon integrating the remaining equation once more with respect to $\vec{p}$, the original equation is reduced to a purely time dependent Volterra type integral equation. Depending on the explicit form of the kernel of the remaining equation this problem is more easily solvable. This is the approach we are going to follow in our explicit application. A similar method has been pursued in configuration space in [144, 145].

10.2 The one-dimensional delta potential

We commence the discussion by considering a one-dimensional set up, where we take the potential to be the one-dimensional attractive $\delta-$potential

$$V(\mathbf{x}) = -\alpha\,\delta(\mathbf{x}) \quad . \tag{10.14}$$

α is positive and real. This is a very popular example [42, 101, 141, 142, 143, 144, 146, 147, 148, 149, 150], since it has the virtue to possess only one bound state, with bound-state energy $-\frac{\alpha^2}{2}$. Its normalized wave function in both configuration and momentum space representation is well-known to be

$$\psi(x, t=0) = \sqrt{\alpha}e^{-\alpha|x|} \qquad \text{and} \qquad \psi(p, t=0) = \sqrt{\frac{2}{\pi}}\frac{\alpha^{\frac{3}{2}}}{\alpha^2+p^2} \quad . \tag{10.15}$$

The projector in (8.5) becomes $P = |\psi\rangle\langle\psi|$, and therefore the ionization probability reads

$$\mathcal{P}(\psi) = 1 - |\langle\psi, U_1(\tau,0)\,\psi\rangle|^2 = 1 - |q(\tau)|^2 \quad . \tag{10.16}$$

This equation also serves to define the survival probability $|q(\tau)|^2$. The problem of convergence of the GV series mentioned in Sec. 10.1 is expected not to occur in this case, since apart from $x=0$, the potential is always smaller than the field. However, despite the apparent simplicity of the model it still seems a hopeless task to sum up the whole perturbative series even for potentials with only one bound state and to determine the time evolution operator $U_I^S(\tau,0)$ exactly. For the case of the $\delta-$potential the problem may be reduced to a far easier equation in the following way:

Since the potential in the momentum representation becomes simply

$$V(p,p') = \langle p|V|p'\rangle = -\frac{\alpha}{2\pi}, \tag{10.17}$$

equation (10.11) together with (10.12) becomes

$$\begin{aligned}\psi(p,t) &= \psi_{GV}(p,t) + i\frac{\alpha}{2\pi}\int_0^t ds e^{-ia(t)}e^{ic_{ts}(p-b(t))}e^{-\frac{i}{2}(p-b(t))^2(t-s)}\psi_I(s)\\ &= \psi_{GV}(p,t) + \Psi(p,t)\,,\end{aligned} \tag{10.18}$$

where we introduced the function

$$\psi_I(t) = e^{ia(t)}\int_{-\infty}^{\infty} dp\,\psi(p,t) \quad . \tag{10.19}$$

Integrating now (10.18) with respect to p one may reduce it to a Volterra equation of the second kind in t

$$\psi_I(t) = \int_{-\infty}^{\infty} dp\,\psi_{GV}(p,t) + \alpha\sqrt{\frac{i}{2\pi}}\int_0^t ds\psi_I(s)\frac{e^{i\frac{c_{ts}^2}{2(t-s)}}}{\sqrt{t-s}}, \tag{10.20}$$

which serves to determine $\psi_I(t)$. Appendix F provides a detailed discussion of this equation. Leaving now $\psi_I(t)$ as the only unknown quantity, we may compute the survival probability of the bound state $|\psi\rangle$ by means of (10.18) in a closed analytic form

$$|q(\tau)|^2 = |\langle\psi, \psi_{GV}(\tau)\rangle + \langle\psi, \Psi(\tau)\rangle|^2 \quad . \tag{10.21}$$

We obtain upon using (10.13) and (10.15)

$$\langle\psi, \psi_{GV}(\tau)\rangle = \frac{2}{\pi}\alpha^3 e^{-ia(\tau)}\int_{-\infty}^{\infty} dp \frac{\exp\left(-i\tau\frac{p^2}{2} - ic(\tau)\,p\right)}{\left(\alpha^2 + (p+b(\tau))^2\right)(\alpha^2+p^2)} \tag{10.22}$$

and together with (10.18)

$$\langle\psi, \Psi(\tau)\rangle = ie^{-ia(\tau)}\sqrt{\frac{\alpha^5}{2\pi^3}}\int_0^{\tau} ds\psi_I(s)\int_{-\infty}^{\infty} dp\frac{e^{ic_{\tau s}(p-b(\tau))}e^{-\frac{i}{2}(p-b(\tau))^2(\tau-s)}}{(\alpha^2+p^2)}. \tag{10.23}$$

Before we turn to the evaluation of these expressions it is instructive to carry out a quick consistency check. Naturally we have to have

$$\lim_{E_0\to 0}|q(\tau)|^2 = 1. \tag{10.24}$$

First of all we may carry out the limit $E_0 \to 0$ for (10.19)

$$\lim_{E_0\to 0}\psi_I(t) = \int_{-\infty}^{\infty} dp\sqrt{\frac{2}{\pi}}\frac{\alpha^{\frac{3}{2}}}{\alpha^2+p^2}\exp i\frac{\alpha^2}{2}t = \sqrt{2\alpha\pi}\exp i\frac{\alpha^2}{2}t \quad . \tag{10.25}$$

Performing the same limit for the Volterra equation (10.20) yields[2]

$$\psi_I(t) = \sqrt{2\alpha}U_{\frac{1}{2},\frac{1}{2}}\left(\frac{it\alpha^2}{2}\right) + \alpha\sqrt{\frac{i}{2\pi}}\int_0^t ds\frac{\psi_I(s)}{\sqrt{t-s}}, \tag{10.26}$$

which is indeed solved by (10.25) as one may easily verify. Using on the other hand expression (10.25) in equation (10.23) it is straightforward to obtain together with (10.21), (10.22) and (10.23) the limit (10.24), which supports the validity of the above expressions.

Taking the extreme limit $E_0 \to \infty$ as a further check, one may easily see that the survival probability tends to zero, except when $b(\tau) = c(\tau) = 0$, in which case it tends to the zeroth order of the Gordon-Volkov perturbation theory

$$\lim_{E_0\to\infty}|q(\tau)|^2 = \begin{cases}|\langle\psi, \psi_{GV}(\tau)\rangle|^2 & \text{for } b(\tau)=c(\tau)=0\\ 0 & \text{otherwise}\end{cases}. \tag{10.27}$$

[2] Relation (10.26) (also e.g. (10.28) and (F.1)) follows upon using the integral representation for the confluent hypergeometric function $U_{a,b}(z) = \frac{1}{\Gamma(a)}\int_0^{\infty} dt\,e^{-zt}t^{a-1}(1+t)^{b-a-1}$, (not to be confused with the time evolution operator). Properties of this function may be found for instance in [140]. Alternatively one may also employ error functions which are known to be related to the particular confluent hypergeometric function via $w(iz) = \frac{1}{\pi}\int_{-\infty}^{\infty}\frac{e^{-p^2}}{z+ip}dp = \frac{1}{\sqrt{\pi}}U_{\frac{1}{2},\frac{1}{2}}(z^2)$. In what follows, it will be important to keep in mind that in the defining domain for the integral representations of $U_{a,b}(z)$, the complex z-plane, there are branch cuts along the real axis. For the validity of the present integral representation one demands therefore $\mathrm{Re}(z) > 0$.

This follows directly from an inspection of equations (10.22) and (10.23), together with the Riemann-Lebesgue theorem, which is in agreement with the general result in [136]. Hence once one is in a regime in which the higher order contributions are negligible one may think of this phenomenon as asymptotically weak stabilization for the case $b(\tau) = c(\tau) = 0$, according to the discussion in Secs. 8.2 and 10.1.

10.2.1 Lowest Order GV perturbation Theory

We shall commence by discussing first the effects resulting from taking solely $\langle \psi, \psi_{GV}(\tau) \rangle$ into consideration, which corresponds to the lowest order in the GV-perturbation theory. Similarly as in [101], one might expect that the key features will already be present at this order. However, we will demonstrate that care has to be taken concerning the convergence of the GV series which depends sensitively on the choice of the parameters, i.e. τ, α and E_0, involved (see Appendix F). As we already observed, a different physical behavior is obtained depending on the values of $b(\tau)$ and $c(\tau)$ and it is therefore instructive to treat several cases separately:

$b(\tau) = 0$ **and** $c(\tau) = 0$

One readily observes from (10.22), that the case $b(\tau) = c(\tau) = 0$ is very special, since then the dependence on the field amplitude E_0 drops out entirely and one simply obtains

$$\mathcal{P}^{(0)}(\psi) = 1 - \frac{4}{\pi} \left| U_{\frac{1}{2},-\frac{1}{2}} \left(i\tau \frac{\alpha^2}{2} \right) \right|^2 \quad . \tag{10.28}$$

We will use $\mathcal{P}^{(n)}$ for the ionization probability in the n^{th} order of GV-perturbation theory throughout.

The fact that, up to a phase, $\mathcal{A}_{l \leftarrow KH}(\tau) = 1$ for the case $b(\tau) = c(\tau) = 0$ is responsible for the disappearance of the explicit dependence on the field amplitude. Hence, in this order of GV-perturbation theory the ionization probability simply becomes proportional to the pulse length τ. As we already stated in (10.27), equation (10.28) precisely coincides with the expression for the ionization probability which one obtains in the extreme limit $E_0 \to \infty$, that is example 2 in [136] (in [136] only the case of the three-dimensional $\delta-$potential was presented) applied to the one dimensional δ-potential. Therefore, in this limit, the zeroth order GV-perturbation theory is exact. However, since we have to have $\mathcal{P}(\psi) = 0$ for $E_0 \to 0$, we also observe that for small and intermediate field strength this is in general in poor agreement with the correct answer.

We would also like to comment on the dependence of $\mathcal{P}^{(0)}(\psi)$ on the coupling α, i.e. essentially the energy, for this case. Since $\left| U_{\frac{1}{2},-\frac{1}{2}}(z) \right|$ is a monotonically decreasing function of z we conclude, assuming that this order is dominant, that more deeply bound states are more likely to ionize. Intuitively this is clear, states with larger α are more localized, such that the overlap between two wave functions vanishes relatively quickly if one of the wave functions evolves with the free time evolution operator. Hence tunneling effects play no role in this case. This is in qualitative agreement with previously obtained results for the Hydrogen atom concerning these types of pulses (see discussion in the previous chapter and [135]).

$b(\tau) = 0$ **and** $c(\tau) \neq 0$

We will now consider the case in which the pulse is switched on and off but subject to the condition $b(\tau) = 0$. As we remarked above, in this case the limit $E_0 \to \infty$, when $c_0(\tau)$ is kept fixed, yields $\mathcal{P}(\psi) = 1$ for all $E_0 \geq 0$. For the generic case we consider the derivative

$$\frac{d\mathcal{P}^{(0)}(\psi)}{dE_0} = -\langle \psi, \psi_{GV}(\tau) \rangle \frac{d}{dE_0} \langle \psi, \psi_{GV}(\tau) \rangle^* - c.c. \quad . \tag{10.29}$$

Since we know $\mathcal{P}^{(0)}(\psi)|_{E_0=0}$ and $\mathcal{P}^{(0)}(\psi)|_{E_0=\infty}$ from the preceding discussion, the occurrence of strong stabilization up to this order implies that $\mathcal{P}^{(0)}(\psi)$ has at least one minimum and one maximum as a function of E_0. Therefore, in order to show the absence of strong and weak stabilization, it is now sufficient to prove that $\frac{d\mathcal{P}^{(0)}(\psi)}{dE_0}$ never vanishes. Since $\langle \psi, \psi_{GV}(\tau) \rangle$ is in general also non zero, otherwise we would have $\mathcal{P}^{(0)}(\psi) = 1$, it suffices to demonstrate that

$$\frac{d}{dE_0} \langle \psi, \psi_{GV}(\tau) \rangle = -\frac{2\alpha}{\pi E_0} c(\tau) \int_0^\infty dp \frac{p \exp\left(-i\tau \frac{p^2 \alpha^2}{2} \right) \sin\left(c(\tau) \alpha p \right)}{\left(1 + p^2 \right)^2} \neq 0 \,. \tag{10.30}$$

A quick investigation of the integral (10.30) shows that neither the real nor the imaginary part may vanish. There is of course still the possibility that $\langle \psi, \psi_{GV}(\tau) \rangle \frac{d}{dE_0} \langle \psi, \psi_{GV}(\tau) \rangle^*$ is purely imaginary. To exclude this possibility on general grounds is more complicated and we will consult the explicit expressions for this purpose below. With this restriction still to be settled, our conclusion for the situation in which $b(\tau) = 0$, is that weak stabilization to lowest order GV-perturbation theory may only occur under the additional condition $c(\tau) = 0$. Strong stabilization is always absent.

Concerning the question of the presence or absence of stabilization the above argument is almost sufficient. Besides completing the proof, it is instructive to consider also the explicit analytic expression for $\mathcal{P}^{(0)}(\psi)$, since it will reveal the sensitivity of this effect towards small deviations from the weak stabilization condition $b(\tau) = c(\tau) = 0$. We present here a solution in form of elementary functions, which to our knowledge was not known hitherto.

Taking now $b(\tau) = 0$ the integral (10.22) can be conveniently split into four integrals by using partial fractions. Then each of the integrals may be computed by means of the integral representation of the error or confluent hypergeometric functions. We note that the integral representations of these function only hold for $\mathrm{Re}(z) > 0$. This condition may be expressed with the help of Keldysh-like parameters (see below), which usually separate regions of different physical behaviour. Surely one may analytically continue these functions in the standard way by rotation of the path of integration [140]. Introducing the quantities

$$\varphi_\pm = \frac{1}{2} \left(1 \pm \alpha c(\tau) - i\tau\alpha^2 \right) \quad \text{and} \quad \Phi_\pm = \tau\alpha^2 \left(\pm\vartheta + \frac{i}{2} \left(1 - \vartheta^2 \right) \right) \tag{10.31}$$

some algebra leads for the amplitude of the survival probability for the bound state

$$q(\tau) = \varphi_- U_{\frac{1}{2},\frac{1}{2}}(\Phi_+) + \varphi_+ U_{\frac{1}{2},\frac{1}{2}}(\Phi_-) + i\tau\alpha^2 U_{\frac{1}{2},\frac{3}{2}} \left(\frac{i\tau\alpha^2}{2} \right) . \tag{10.32}$$

For a given binding energy E of the bound state we introduced here the parameter

$$\vartheta := \frac{c(\tau)}{\tau \sqrt{2|\varepsilon_0|}} \quad , \tag{10.33}$$

which characterizes the validity of the preceding expressions. In our particular example the binding energy is $\varepsilon_0 = -\frac{\alpha^2}{2}$. Notice that, when taking a pulse of the type (10.4), this parameter is closely related to the inverse of the Keldysh parameter $\gamma = \omega\sqrt{2|\varepsilon_0|}/E_0$ [65], which separates the multiphoton ionization region from the tunneling region

$$\vartheta = \frac{\omega\, c(\tau)}{E_0 \tau\, \gamma} \,. \tag{10.34}$$

Note that many pulses have the property $\lim_{\tau \to 0} \frac{c(\tau)}{E_0 \tau} = \omega^{-1}$ (e.g. (10.42)), such that in these cases $\lim_{\tau \to 0} \vartheta^{-1} = \gamma$. The restriction

$$|\vartheta| < 1 \tag{10.35}$$

guarantees convergence, uniqueness and avoids transversion through the branch cut concerning the above integral representations for the confluent hypergeometric functions. So we have to keep in mind that (10.32) is only applicable under the condition (10.35).

Once more we may check for consistency and verify whether anything went wrong during the computation. Taking the limit $c(\tau) \to 0$ we should recover the result (10.28) of the preceding subsection. Indeed

$$\begin{aligned} \lim_{c(\tau)\to 0} q(\tau) &= \frac{2}{\sqrt{\pi}}\left(\left(\frac{1}{2}-\frac{i\tau\alpha^2}{2}\right)U_{\frac{1}{2},\frac{1}{2}}\left(\frac{i\tau\alpha^2}{2}\right)\right)+\alpha(1+i)\sqrt{\frac{\tau}{\pi}} \\ &= \frac{2}{\sqrt{\pi}}U_{\frac{1}{2},-\frac{1}{2}}\left(\frac{i\tau\alpha^2}{2}\right) \quad , \end{aligned} \tag{10.36}$$

where the latter equality follows upon a well-known identity for confluent hypergeometric functions which may be found for instance in [140].

$b(\tau) \neq 0$ and $c(\tau) \neq 0$

Finally we treat the generic case, that is for arbitrary $b(\tau) \neq 0$ and $c(\tau) \neq 0$. Once more we may use a decomposition into partial fractions and reduce the computation of (10.22) to integrals of the type which are directly related to the integral representation of the confluent hypergeometric functions. Introducing the quantities

$$\tilde{\varphi}_\pm = \frac{\alpha^2}{b(\tau)^2 \pm 2ib(\tau)\alpha} \qquad \text{and} \quad \tilde{\Phi}_\pm = \tau\alpha^2\left(\pm\tilde{\vartheta}+\frac{i}{2}\left(1-\tilde{\vartheta}^2\right)\right) \tag{10.37}$$

with $\tilde{\vartheta} = \frac{c(\tau)}{\tau\alpha} + \frac{b(\tau)}{\alpha}$ we obtain for the amplitude of the survival probability

$$q(\tau) = \frac{\tilde{\varphi}_+}{\sqrt{\pi}}\left[U_{\frac{1}{2},\frac{1}{2}}(\Phi_+)+U_{\frac{1}{2},\frac{1}{2}}(\tilde{\Phi}_-)\right]+\frac{\tilde{\varphi}_-}{\sqrt{\pi}}\left[U_{\frac{1}{2},\frac{1}{2}}(\Phi_-)+U_{\frac{1}{2},\frac{1}{2}}(\tilde{\Phi}_+)\right]. \tag{10.38}$$

Due to the same reasons as in the preceding section, i.e. properties of the integral representation of the confluent hypergeometric functions, we obtain now the condition

$$\left|\tilde{\vartheta}\right| = \frac{\omega}{\gamma E_0}\left|\frac{c(\tau)}{\tau}+b(\tau)\right| < 1 \tag{10.39}$$

in addition to (10.35). Once again we may carry out the limit $b(\tau), c(\tau) \to 0$ and try to recover (10.28). Indeed we obtain

$$\lim_{b(\tau),c(\tau)\to 0} q(\tau) = \frac{1}{\sqrt{\pi}}U_{\frac{1}{2},\frac{1}{2}}\left(\frac{i\tau\alpha^2}{2}\right)+\frac{i\tau\alpha^2}{2\sqrt{\pi}}U_{\frac{3}{2},\frac{3}{2}}\left(\frac{i\tau\alpha^2}{2}\right) = \frac{2}{\sqrt{\pi}}U_{\frac{1}{2},-\frac{1}{2}}\left(\frac{i\tau\alpha^2}{2}\right).$$

10.2.2 All higher Order Contributions

We now come to the higher order contributions. For this purpose we have to evaluate (10.23), which, after computations similar to the ones in the preceding section, equals

$$\langle\psi,\Psi(\tau)\rangle = \frac{i\alpha^{\frac{3}{2}}e^{-ia(\tau)}}{2\pi\sqrt{2}}\int_0^\tau ds\psi_I(s)\,e^{\frac{ic_{\tau s}}{2(\tau-s)}}\left(U_{\frac{1}{2},\frac{1}{2}}(\Phi'_-)+U_{\frac{1}{2},\frac{1}{2}}(\Phi'_+)\right), \tag{10.40}$$

with

$$\Phi'_\pm = \pm\alpha\left(c_{ts}-(t-s)\,b(t)\right)+\frac{i}{2}(t-s)\left(\alpha^2-\left(\frac{c_{ts}}{t-s}-b(t)\right)^2\right). \tag{10.41}$$

In principle there is now only a time integration and the unknown $\psi_I(t)$ left.

The general solution to (10.20) may be approximated by an iterative procedure in a similar fashion as we generated (10.1). However, in this case the problem of convergence is taken care of by a well-known theorem concerning integral equations (see for instance [151]). It states, that if the free term in a Volterra equation is absolutely integrable, then successive approximations for this equation converge for *all* values of the constant in front of the integral. Hence, choosing a reasonable pulse, the iterative solution to (F.1) always makes sense. In Appendix F this point is discussed in more detail.

In order to study the explicit dependence of the ionization probability as a function of the intensity of the incoming light, we have to select a concrete pulse. We choose linearly polarized light with a trapezoidal enveloping function. This type of pulse has also been taken as an example in the previous chapter (see Subsec. 9.2.3, Equation 9.24) and is widely used in the literature [109, 150]. We consider a pulse of duration τ which has linear turn-on and turn-off ramps of length T. Choosing the ramps to have the length $T = n\frac{2\pi}{\omega}$, with n being an integer, we have the desired property that $b(\tau) = 0$ for arbitrary τ. The total displacement takes on a particularly simple form in this case

$$c(\tau) = \frac{E_0}{\omega^2}\sin\omega\tau \quad , \tag{10.42}$$

which vanishes with the additional constraint on the pulse duration $\tau = 2n\frac{\pi}{\omega}$. Of course in order to achieve $b(\tau) = 0$ one may also fix the pulse duration $\tau = n\frac{2\pi}{\omega}$, leaving T as the only variable for this family of pulses. In this case we have

$$c(\tau) = \frac{E_0}{\omega^3 T}\left(8\sin^2\left(\frac{\omega T}{2}\right)+(2n\pi-2\omega)\sin\omega T\right). \tag{10.43}$$

10.2.3 First Order GV perturbation Theory

For pulses of the type (9.24) we will now analyze the ionization probability up to first order in the GV expansion. For this purpose we want to approximate the function $\psi_I(t)$ in (10.40) by the free term in the Volterra equation (F.1). In order to select parameters for which this approximation is valid, we consult the expression for the maximal relative error μ computed in Appendix F (F.18). From Fig. 10.1 we observe that $\alpha = 1/8$ and $\tau \sim 1$ should lead to reasonably precise results for the case $b(\tau) = c(\tau) = 0$.

We shall now briefly comment on the convergence of the GV series for some results presented in the literature. For instance, in the last reference of [101] a pulse with instantaneous switch on was used in this context, i.e. $E(t) = E_0\cos(\omega t)$, and an analysis up to the first order GV-perturbation theory was carried out. Typical parameters in [101] were $\alpha = 1/2, E_0 = 5, \omega = 1.5$ and the pulse length was 2 cycles, that is $\tau \sim 8$. For these parameters we obtain $\mu \approx 8.44$, such that we do not expect convergence of the GV-perturbation series up to this order. In fact, as 10.2 shows, relevant contributions are to be expected up to the order 10. The convergence is even worse for the typical parameters used in [150], since as Fig. 10.2 indicates in this case (diamonds) one should go beyond the 40-th order to achieve a reasonable approximation. These arguments also raise doubt on the reliability of statements based on this order of the Volkov series in the context of the Hydrogen atom (third reference in [101]). Of course in order to be quantitatively precise one requires a similar analysis as carried out in Appendix F for the Coulomb potential. Since this is a long range potential one expects intuitively that the GV-series converges even more slowly than in the presented case. The argument presented in there, i.e. that the addition of the next order only changes slightly the result, is not rigorous since this effect is additive and in the worst case one might be in a situation for which the contributions from each higher order are still increasing (as in Fig. 10.2 the curve with diamonds indicates).

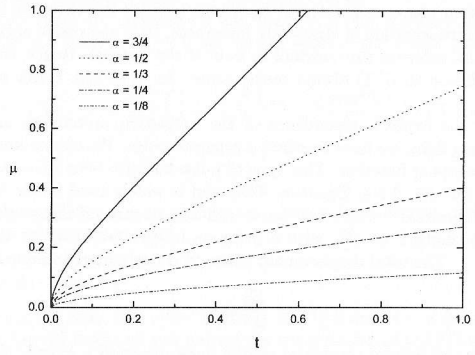

Figure 10.1: Upper bound for the relative error obtained by solving the Volterra equation iteratively, as a function of t, for several values of the coupling constant α.

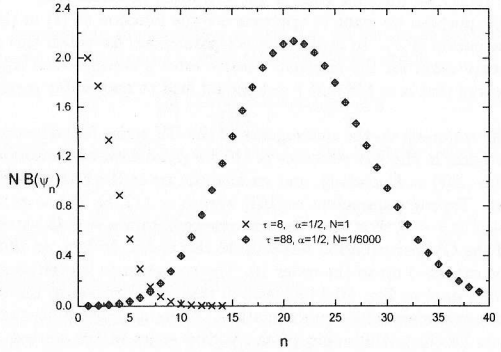

Figure 10.2: Upper bound for $|\psi(t)|$ obtained by iteration of the Volterra equation, as a function of the order n of iteration.The upper bound to n-th order is multiplied by a normalizing constant N , and denoted by $NB(\psi_n)$. The crosses and diamonds refer, respectively, to parameters used by Geltman [101] and by Su et al. [150].

10.3 Discussion

From the results of this chapter, it is clear that the important parameters determining the absence or the presence of stabilization are the momentum transfer and the classical displacement at the end of the pulse. This condition is independent of the frequency and the pulse shape, such that the turn-on and off play only a secondary role.

In the literature, some authors take only the momentum transfer $b(T)$ at the end of the turn-on as an important condition for the existence of stabilization [112, 122]. Some computations do not even fulfill or refer to this condition [125, 117]. In our analysis, this is not a crucial parameter. However, for some pulse shapes, such as a trapezoidal pulse switched on and off in an integer number of cycles, it so happens that $b(T)$ *and* $b(\tau)$ vanish. Since numerical computations are sometimes of difficult interpretation,they would possibly suggest that the former, and not the latter parameter, is of importance. In some computations, the condition $b(\tau) = 0$ is actually fulfilled, in the sense that the vector potential, and not the field, is switched on and off smoothly [114]. For $A(0) = 0$ and $A(t)$ continuous, $A(t)$ and $b(t)$ differ up to a minus sign (see Chapter 2). These authors are in fact aware of the condition upon the momentum transfer, which is discussed in detail in [121]. However, since their studies were mainly based on classical arguments, we present an alternative and more rigorous interpretation of this condition. The condition concerning the classical displacement is usually not mentioned in the literature, and, in some cases, $b(\tau) = 0$ still yields a considerably large classical displacement at the end of the pulse [104, 109, 111]. Recently, however, numerical computations fulfilling also this condition [131] reproduced the experimental results of [21] quantitatively. Qualitatively, our results for vanishing momentum transfer and classical displacement at the end of the pulse also agree with these experiments, in the sense that the ionization probability as a function of the field strength tends asymptotically to a finite value *smaller than one.*

Also the high frequency approach is a way to guarantee that $b(t)$ and $c(t)$ approximately vanish for all times. As a consequence, the transformation from the Kramers Henneberger frame to the velocity or length gauge becomes the identity operator, such that the ionization probability does not depend on the external field.

Our analysis has also shown the inadequacy of the zeroth order Gordon-Volkov solution for describing atomic stabilization. Within this approximation, one can at most identify this phenomenon in its weak asymptotic form, for vanishing $b(\tau)$ and $c(\tau)$. For describing stabilization in its strong form, it is definitely not sufficient. Furthermore, for typical parameters, the Volterra equation (10.20) presents a very slow convergence, such that more orders of the Volkov series are necessary for an appropriate computation of ionization probabilities. Therefore, existing results in the literature concerning this phenomenon based on the Gordon-Volkov solution, as for instance [99, 101, 104, 105] must be seen with extreme care.

Part III

Low-intensity harmonic generation with short pulses

Chapter 11

Amplitude-modulated second harmonic generation as an initial value problem

In the previous parts, we were concerned with high-intensity optical phenomena, in particular ionization and harmonic generation. In this part, we consider the *macroscopic response* of a medium to short-pulsed incident radiation, within the *weak-field* framework. More specifically, we present an analytical solution to second harmonic generation (SHG), taking into account an amplitude-modulated incident pulse of *arbitrary* shape. One should keep in mind that the single-atom response is not the only source of harmonic radiation, but nonlinear optical processes may also occur due to wave-mixing in a medium [6]. In most computations in the high-intensity regime where propagation is included, these effects are neglected [58]. Harmonic generation at low intensities involving single atoms is briefly recalled in Appendix B.

Until the eighties, experiments on nonlinear optics been performed either using cw laser radiation, or relatively long laser pulses. Within this framework, the propagation equations are reducible to coupled first-order ordinary differential equations, which can be solved analytically. As the laser pulses became shorter and shorter, the walk-off of the pulses at fundamental and harmonic frequencies gained considerable importance in the physics of nonlinear optical processes, such that non-stationary effects like group velocity mismatch have become a problem of interest [153, 154]. For such fields, even in a one-dimensional theory, which we have here in mind exclusively, nonlinear partial differential equations must be solved.

In the case of a purely amplitude–modulated fundamental wave, the problem is governed by a second-order equation named after Liouville [155] (which should not be confused with the Liouville equation in Statistical Mechanics). Even though this connection has been known since a quarter of a century [156], to the best of our knowledge no attention has been paid to it in current text books on nonlinear optics, or in articles on SHG. This is rather surprising since the Liouville equation is one of the few examples of nonlinear equations for which the general solution can be derived explicitly. Such a solvable theory is very useful, and even under conditions where the inherent idealizations are only approximately fulfilled could be used as a zeroth–order approximation. Despite of the general solvability it is not quite obvious how to select, among the solutions of the Liouville equation, the physically relevant SHG solutions. Therefore, it is a matter of interest to consider the following two questions, whose answers characterize the purpose of the present chapter.

1. How to solve the initial value problem for an incident pulse of arbitrary shape at the funda-

mental frequency, under the condition that there is no incident harmonic wave?

2. Are there examples for which this problem has a fully analytical solution?

Both problems are of physical relevance and experimental interest [154, 157, 158, 159, 160, 161], and to our knowledge the prescribed initial value problem has never been systematically studied. A particular type of analytical solutions with the initial pulse being of squared Lorentzian shape was found by Akhmanov et al. [162], c.f., Subsec. 11.3.3.
Throughout this work, we will discuss a more general approach and study this problem systematically. We will give several new analytical solutions for experimentally relevant initial pulses.

This chapter is organized as follows: In Sec. 11.1.1 we briefly review the basic equations describing one-dimensional SHG in the slowly varying amplitude approximation and in Sec. 11.1.2 we establish the connection to the Liouville equation. Similarity transformations of evolution equations, which are useful in the subsequent analysis, are discussed in Subsec. 11.1.3. In Subsec. 11.1.4 we define Goursat and Cauchy problems. Subsection 11.2.1 is the main part of the chapter. In there, we show how the physically relevant initial value problem is reduced to a Schrödinger-type equation, where the initial pulse shape plays the role of a repulsive potential. In Section 11.3 several examples are analyzed in detail. Analytical solutions are given for many realistic cases and a broad class of exponentially decaying initial pulses is found with the help of a single numerical integration. In Section 11.4 we state our conclusions.

11.1 Second harmonic generation in one space dimension

11.1.1 General propagation equations for short pulses

The propagation of an electromagnetic wave in a medium of dielectric constant ϵ is given by the wave equation

$$\left(-\nabla^2 + \frac{1}{c^2}\frac{\partial^2}{\partial t^2}\right)\vec{E}(\vec{r},t) = -\frac{1}{\epsilon c^2}\frac{\partial^2}{\partial t^2}\left(\vec{P}^{(1)}(\vec{r},t) + \vec{P}_{NL}(\vec{r},t)\right). \tag{11.1}$$

Here, $\vec{E}(\vec{r},t)$ denotes the electric field and the vectors on the right-hand-side the macroscopic polarization induced in the medium by the field, with $\vec{P}^{(1)}(\vec{r},t)$ and $\vec{P}_{NL}(\vec{r},t)$ corresponding to, respectively, its linear and nonlinear response. As a first simplification, we take the electric field as a quasi-monochromatic wave propagating along an axis x, such that this problem can be reduced to a one-dimensional one[1],

$$\left|\vec{E}(\vec{r},t)\right| = \left|\vec{E}(x,t)\right| = E_0(x,t)\exp[i(kx-\omega t)]. \tag{11.2}$$

We consider now that the enveloping function $E_0(x,t)$ varies much more slowly than the oscillating part of (11.2), such that the second temporal and spatial derivatives in (11.1) are negligible. This is called the slowly-varying amplitude (SVA) approximation. With this further restriction, we exclude for instance half-cycle pulses [163] from our framework. After a few other manipulations, which include the neglect of the dispersion of the nonlinear polarization and of the dielectric constant [6](i.e., $\epsilon(\omega) \simeq 1$), one has

$$\left(-\frac{\partial}{\partial x} + \frac{1}{v_g}\frac{\partial}{\partial t}\right)E_0(x,t) = \frac{i2\omega^2}{kc^2}P_{NL}(x,t)e^{-i(kx-\omega t)}, \tag{11.3}$$

[1] One should note that, in case one is interested in, for instance, describing the propagation of the high-harmonics discussed in the previous chapters, one must take a field of the form $\sum_n E_{0n}(x)\exp[in(kx-\omega t)]$, which corresponds to the output of the single-atom computations performed in Part I.

where $v_g = dk/d\omega$ is the group velocity of the pulse, assumed constant. For strictly monochromatic fields, the second term on the left-hand side is zero. Now we make the assumption that P_{NL} can be expanded in powers of the field. The most general form for this expansion is the tensorial product

$$\vec{P}_{NL}(x,t) = \chi^{(2)} : \vec{E}(x,t)\vec{E}(x,t) + \chi^{(3)} : \vec{E}(x,t)\vec{E}(x,t)\vec{E}(x,t) + ... \tag{11.4}$$

The tensors $\chi^{(n)}$are called "nonlinear susceptibilities", and depend very much on the material in question. For instance, for isotropic materials, such as gases, due to symmetry considerations, the even susceptibilities vanish (see e.g. [164] for a detailed discussion of this issue). Clearly, the expansion above only converges for *weak* fields. In the high-intensity regime, the induced polarization is a complicated function of the intensity of the driving field, such that in this case a numerical treatment is required [22]. Moreover, there is an extra phase involved in the problem, since the harmonics generated in the single-atom response have an intensity-dependent phase. Concerning second harmonic generation, we consider this expansion up to $\chi^{(2)}$.

In a second–order nonlinear medium, the interaction between two quasi– monochromatic plane electromagnetic waves, with slowly–varying complex electric field amplitudes $E_{01}(x,t), E_{02}(x,t)$ and respective frequencies ω_1 and $\omega_2 = 2\omega_1$, is described by the two differential equations [29]

$$(\partial_x + \frac{1}{v_1}\partial_t)E_{01} = -\mathrm{i}\Xi E_{02}E_{01}^* \quad , \quad (\partial_x + \frac{1}{v_2}\partial_t)E_{02} = -\mathrm{i}\Xi E_{01}^2 \, . \tag{11.5}$$

Here we assumed that the wave–numbers of both carrier waves fulfil the phase–matching condition $k_2 = 2k_1$. The star denotes complex conjugation. x,t are laboratory space and time coordinates. The coupling constant Ξ is expressed as

$$\Xi = \frac{2\chi^{(2)}\omega_1^2}{k_1 c^2} \, . \tag{11.6}$$

11.1.2 SHG and the Liouville equation

In order to write the equations of motion in a convenient form we introduce characteristic coordinates

$$\chi = \nu(-t + x/v_2) = -\nu\tau_2 \quad , \quad \tau = \nu(t - x/v_1) = \nu\tau_1 \, , \tag{11.7}$$

where the parameter ν describing the group velocity mismatch is given by

$$\nu = (1/v_2 - 1/v_1)^{-1} \, , \tag{11.8}$$

and introduce new amplitudes q_1, q_2 by taking

$$E_{01} = \sqrt{2}\Xi^{-1}q_1 \quad , \quad E_{02} = 2\mathrm{i}\Xi^{-1}q_2 \, . \tag{11.9}$$

The inverse transformation of (11.7) is

$$x = \chi + \tau \quad , \quad t = \chi/v_1 + \tau/v_2 \, , \tag{11.10}$$

and the derivatives are transformed according to

$$\partial_\chi = \partial_x + \frac{1}{v_1}\partial_t \, , \; \partial_\tau = \partial_x + \frac{1}{v_2}\partial_t \, . \tag{11.11}$$

In this way we arrive at the differential equations

$$(\partial_x + \frac{1}{v_1}\partial_t)q_1 = \partial_\chi q_1 = -2q_2q_1^* \quad , \quad (\partial_x + \frac{1}{v_2}\partial_t)q_2 = \partial_\tau q_2 = q_1^2 : . \tag{11.12}$$

The scaling of the amplitudes is such that, up to a common scaling factor, $|q_1|^2, |q_2|^2$ may be interpreted as photon current densities. The physical conditions included in the present model can be summarized as follows :

1. Applicability of the slowly–varying amplitude approximation (SVA), i.e. the pulses should still be long compared to the wavelengths.

2. One-dimensionality in space, i.e. the transverse structure can be neglected.

3. The phase matching condition $2k_1 = k_2$ for the wave numbers $k_{1,2}$ are fulfilled exactly for the two carrier waves.

4. The group velocities v_1 and v_2 do not coincide, but

5. the dispersion within either of the two pulses at frequencies ω_0 and $2\omega_0$ can be neglected.

According to theoretical estimations [29] and experiments [154] these presumptions are quite realistic. For instance, for 100 fs pulses with intensities above 100 GW/cm^2 and long–focus conditions in KDP or $LiIO_3$ crystals, high conversion efficiencies can be achieved over crystal lengths of several mm. Both pump depletion and group velocity dispersion then become important and a non-stationary approach to the problem is required. One may also think of a realization in a planar optical waveguide.

The basis for applying the inverse scattering transform method to equations (11.12) with complex amplitudes was established by Kaup [165]. Its full development, however, met some particular difficulties which have not yet been solved. Recently, Hamiltonian structures and particular solutions, not reducible to real ones, of (11.12) were established [166]. Here we focus our attention on purely amplitude–modulated signals. Thus the amplitudes q_1 and q_2 are real, and the stars in Eqs.(11.12) can be omitted. Clearly, this further approximation excludes important physical effects due to phase mismatch and related applications [167].

Let us now consider causality. In the 1+1 dimensional world of the present SHG model, propagation occurs only with velocities v_1 and v_2. For definiteness we will assume $v_1 > v_2$, *normal group dispersion*, such that ν defined by (11.8) is positive. One should notice, however, that our results are easily transferred to $v_1 < v_2$, i.e., anomalous group dispersion. The *cone of future* from $x = t = 0$ is given by the region

$$v_2 t < x < v_1 t\,, \quad \text{i.e.}\,, \quad \chi > 0\,, \tau > 0. \tag{11.13}$$

The signs of the characteristic coordinates χ, τ are such that causal action always occurs in the direction of increasing coordinates.

It was found by Bass and Sinitsyn [156] that in the case of real amplitudes, the SHG problem of Eqs. (11.12) is solvable. Actually, it is "C-integrable" [168], which means integrable by change of variables. Indeed, one can see that from Eqs. (11.12) with real waves q_1, q_2 we may eliminate q_2 arriving at the Liouville equation

$$\partial_\chi \partial_\tau \ln(4q_1^2) = -4q_1^2. \tag{11.14}$$

The general solution is well known [155] and it is given by

$$q_1^2 = -\frac{1}{2}\frac{F'(\chi)G'(\tau)}{(F(\chi)+G(\tau))^2}\,. \tag{11.15}$$

In Eq. (11.15) $F(\chi)$ and $G(\tau)$ are arbitrary functions, which depend only on χ and τ respectively. The primes denote differentiations. The solution is completed by substitution of Eq. (11.15) in Eqs. (11.12), leading to

$$q_2 = -\frac{1}{4}\frac{F''(\chi)}{F'(\chi)} + \frac{1}{2}\frac{F'(\chi)}{F(\chi)+G(\tau)}\,. \tag{11.16}$$

11.1.3 Similarity transformations

Given any solution $q_1(\chi,\tau)$, $q_2(\chi,\tau)$ of the equations of motion, a two-parameter manifold of solutions can be found by use of similarity (scale) transformations. Equations (11.12), in fact, are invariant under the two following scale transformations:

i) The conformal transformation

$$\chi = a\tilde{\chi}\,,\ \tau = a\tilde{\tau}\,,\ \tilde{q}_1(\tilde{\chi},\tilde{\tau}) = \frac{1}{a}q_1(a\tilde{\chi},a\tilde{\tau})\,,\ \tilde{q}_2(\tilde{\chi},\tilde{\tau}) = \frac{1}{a}q_2(a\tilde{\chi},a\tilde{\tau})\,:, \tag{11.17}$$

ii) The τ–dilation

$$\tau = b^2\tilde{\tau} \quad,\quad \tilde{q}_1(\tilde{\chi},\tilde{\tau}) = \frac{1}{b}q_1(\tilde{\chi},b^2\tilde{\tau})\,, \tag{11.18}$$

and the general similarity transformation is obtained as a combination of both these types. Here a and b are real numbers. Under conformal transformations all the four quantities

$$\int d\chi\; q_k(\chi,\tau) \quad,\quad \int d\tau\; q_k(\chi,\tau) \quad,\quad k = 1,2\,, \tag{11.19}$$

are invariant while, on the other hand, the τ-dilation does not change the integral

$$\int d\tau\; q_1^2(\chi,\tau)\,. \tag{11.20}$$

In the context of the Cauchy problem discussed below, it will be of interest to use only invariance transformations that map the set of straight lines $x \equiv \chi + \tau = const.$ to themselves. This restriction is fulfilled by the conformal transformation, but not by the τ–dilation. Thus any particular solution of Eqs. (11.12) represents a one–parameter family of solutions.

11.1.4 Goursat and Cauchy problems

One may relate two typical initial value problems to the coupled differential equations (11.12):

i) The *Goursat problem* in which initial values are given at characteristic curves

$$q_1(0,\tau) = q_{10}(\tau)\,,\ \tau > 0 \quad;\quad q_2(\chi,0) = q_{20}(\chi)\,,\ \chi > 0\,. \tag{11.21}$$

After substitution of the general solution (11.15-11.16) in Eqs.(11.21) the functions $F(\chi)$ and $G(\tau)$ can be determined by quadratures.

ii) The *Cauchy problem* in which the initial values are given on some line that is *not* a characteristic curve. This is usually the case, as from the physical point of view, it is natural to give both fields q_1 and q_2 for $x = 0$, i.e., according to Eqs. (11.7) and (11.10), for $\tau = -\chi$ and $t = \chi/\nu$,

$$q_1(-\tau,\tau) = q_{10}(\tau) \quad,\quad q_2(-\tau,\tau) = q_{20}(\tau)\,. \tag{11.22}$$

In a common situation encountered in experiments [169] there is an incident ground wave, q_1, with no incident harmonic wave, q_2. This is the Cauchy problem specified by $q_{20} = 0$. In the following we will be concerned with this problem, and we will refer to it as the *restricted Cauchy problem.*

11.2 The restricted Cauchy problem

11.2.1 Solution

Let us write the restricted Cauchy problem in the form

$$q_1^2(-\tau,\tau) = I_1(\tau)\ , \quad q_2(-\tau,\tau) = 0\ . \tag{11.23}$$

Thus, starting from the general solution of Eqs. (11.15-11.16), we have to determine the functions $F(\chi)$ and $G(\tau)$. Upon defining

$$K(\tau) \equiv F(-\tau) \tag{11.24}$$

we get

$$2I_1(\tau) = \frac{K'(\tau)G'(\tau)}{(K+G)^2} \quad , \quad \varrho(\tau) = \frac{1}{2}\frac{K''}{K'} = \frac{K'}{K+G}\ . \tag{11.25}$$

By elimination of G in (11.25), we find

$$\{K,\tau\} \equiv \frac{K'''}{K'} - \frac{3}{2}\left(\frac{K''}{K'}\right)^2 = -4I_1 \tag{11.26}$$

where the curly bracket denotes the Schwarzian derivative [170]. The function $\varrho(\tau)$, defined in the second of Eqs. (11.25), fulfils the Riccati equation

$$\varrho' = \varrho^2 - 2I_1\ , \tag{11.27}$$

which by taking

$$\varrho = -\phi'/\phi\ , \tag{11.28}$$

is connected to the Schrödinger-type equation

$$\phi'' = 2I_1\phi\ . \tag{11.29}$$

By comparison of Eqs. (11.28) and (11.25) we find

$$\frac{\phi'}{\phi} = -\frac{1}{2}\frac{K''}{K'}\ , \tag{11.30}$$

and, by integration,

$$\phi = \frac{1}{\sqrt{K'}}\ . \tag{11.31}$$

Summarizing we may formulate the following "recipe" for solving the restricted Cauchy problem :

1. Given an initial pulse shape $I_1(\tau)$ one first has to solve the second order differential equation (11.29), which can be viewed as a Schrödinger equation with repulsive potential $2I_1(\tau)$ and eigenvalue 0. This is also known as Hill's equation [171]. We require ϕ to be a real function.

2. By means of Eq. (11.31), the function F can be evaluated as

$$K(\tau) = \int_0^\tau \frac{d\tau'}{\phi^2(\tau')}\ , \quad F(\chi) = K(-\chi)\ . \tag{11.32}$$

3. Upon substitution in Eqs.(11.25) and (11.28) we arrive at the function G ,

$$G(\tau) = -K(\tau) + \frac{2K'^2}{K''} = -F(-\tau) - \frac{1}{\phi(\tau)\phi'(\tau)}\ . \tag{11.33}$$

4. Eventually, the solution $q_1(\chi,\tau)$, $q_2(\chi,\tau)$ is found by substituting $F(\chi)$ and $G(\tau)$ in Eqs. (11.15) and (11.16),

$$q_1^2(\chi,\tau) = \frac{\phi''(\tau)\phi(\tau)}{2\phi^2(-\chi)}\left\{\frac{1}{1+\phi(\tau)\phi'(\tau)\left[F(\tau)-F(-\chi)\right]}\right\}^2 \tag{11.34}$$

$$q_2(\chi,\tau) = -\frac{1}{2\phi(-\chi)}\left[\phi'(-\chi) - \frac{\phi(\tau)\phi'(\tau)}{\phi(-\chi)}\frac{1}{1+\phi(\tau)\phi'(\tau)\left[F(\tau)-F(-\chi)\right]}\right]. \tag{11.35}$$

We also notice that the choice of a symmetrical initial pulse $I_1(\tau)$ results in an even function $\phi(\tau)$. In this case $F(\chi)$ is an odd function, and the general solution in Eqs. (11.34-11.35) can be written in the form

$$q_1^2(\chi,\tau) = \frac{\phi''(\tau)\phi(\tau)}{2\phi^2(\chi)}\left\{\frac{1}{1+\phi(\tau)\phi'(\tau)\left[F(\tau)+F(\chi)\right]}\right\}^2 \tag{11.36}$$

$$q_2(\chi,\tau) = \frac{1}{2\phi(\chi)}\left[\phi'(\chi) + \frac{\phi(\tau)\phi'(\tau)}{\phi(\chi)}\frac{1}{1+\phi(\tau)\phi'(\tau)\left[F(\tau)+F(\chi)\right]}\right]. \tag{11.37}$$

It may be worth noticing that $q_1^2(\chi,\tau)$ and $q_2(\chi,\tau)$ can also be expressed in terms of $\rho(\tau)$ and thus avoiding the wave function ϕ. From (11.25) and (11.33), in fact, we get

$$K(\tau) = \int_0^\tau \left[\exp\left(2\int_0^{\tau'}\varrho(\tau'')d\tau''\right)\right]d\tau'\ ,\ G(\tau) = -K(\tau) + \frac{1}{\rho}\exp\left(2\int_0^\tau \rho(\tau')d\tau'\right)\ . \tag{11.38}$$

The wave amplitudes q_1 and q_2 can be obtained by substitution of $F(\chi) \equiv K(-\chi)$ and $G(\tau)$ into Eqs. (11.15) and (11.16).

11.2.2 About uniqueness

In our procedure the solution of the restricted Cauchy problem is reduced to the solution of a Schrödinger (Hill) equation. The latter is by no means unique, because we did not impose any boundary or asymptotic condition. On the other hand, from physical intuition, we expect that there is a unique solution of the Cauchy problem in our case. How can this apparent discrepancy be resolved ?
Given any particular (real) solution $\phi_1(\chi)$ to Eq. (11.29) the general solution is found as

$$\phi(\chi) = \phi_1(\chi)\left(c_1 + c_2\int_0^\chi \frac{d\chi'}{\phi_1^2(\chi')}\right)\ , \tag{11.39}$$

c_1 and c_2 being real numbers. By taking the integral in Eq. (11.32), we obtain

$$F = c_3 - \frac{1}{c_1 + c_2F_1} = \frac{aF_1+b}{cF_1+d}\ . \tag{11.40}$$

In Eq. (11.40) c_3 is an integration constant, and a,b,c,d are real numbers determined, up to an arbitrary common factor, by c_1,c_2,c_3. Eq. (11.40) tells us that F is determined by ϕ up to an arbitrary linear rational mapping. Indeed, it is known [170] – and could be checked directly – that the Schwarzian derivative is invariant under such a transformation, and thus the potential $I_1(\chi)$ in (11.26) is invariant. Moreover, starting from Eqs. (11.32) and (11.24), it can easily be derived that

$-G$ and $-G_1$ are connected by the same linear rational transformation connecting F and F_1. The proof of uniqueness is completed by noting that the right-hand side of (11.15) is invariant under an arbitrary linear rational transformation simultaneously applied to both F and $-G$. Therefore, any solution of a given Hill equation leads to the same physical solution for the pulse amplitudes q_1, q_2. (Note that q_2 is determined by q_1.)

11.3 Examples

The formalism discussed in the previous sections can be applied to several pulse shapes, leading to fully analytical solutions for the Cauchy problem. Some of these pulses are presented and analyzed in this section. In subsection 11.3.4 we also consider a broad class of solutions, having exponential decay as a distinctive feature, which can be generated by a single numerical integration. In all the following examples we impose the condition that the second harmonic wave is zero at the boundary $x = 0$, corresponding to the natural experimental conditions. In the transformed frame this reads $q_2(\chi = -\tau, \tau) = 0$.

11.3.1 Square Pulse

We first consider an initial square pulse, of intensity I_0, switched on and off at respectively $t = 0$ and $t = t_p$. For this pulse, the boundary condition to the Hill equation is given by

$$I_1(\tau) = I_0 \text{ for } 0 < \tau < \nu t_p \text{ and } = 0 \text{ elsewhere .} \tag{11.41}$$

The solution of this problem requires the definition of several spatio-temporal regions, which are shown in Fig. 11.1, both in the lab frame (x, t) and in the characteristic frame (χ, τ). The "pieces" of the solution in the respective regions are connected by the conditions that q_1 is continuous and differentiable in χ, whereas q_2 is continuous and differentiable in τ. From Eqs. (11.12) we get

$$\begin{array}{ll} q_1 \equiv 0\,, & q_2 \equiv 0 \quad \text{in regions II and VI} \\ q_1 \equiv 0\,, & \partial_\tau q_2 \equiv 0 \quad \text{in regions IV and V} \end{array} \tag{11.42}$$

The dynamics occurs exclusively in regions I and III and the Cauchy problem of Eq. (11.41) reduces to the following problems

i) the Cauchy problem for the triangle I

$$q_1(-\tau, \tau) = I_0 \quad , \quad q_2(-\tau, \tau) = 0\,, \tag{11.43}$$

ii) and the Goursat problem for the strip III

$$q_1(\chi = 0, \tau) = q_{10}(\tau)\ , 0 < \tau < \nu t_p \quad ; \quad q_2(\chi, \tau = 0) = 0\ , 0 < \chi \tag{11.44}$$

where q_{10} is known upon i) has been solved.

The Hill equation for triangle I is easily solved by

$$\phi(\tau) = \cosh(B\tau)\ , \qquad B = \sqrt{2I_0}\,. \tag{11.45}$$

Thus, in region I the solution is given by

$$\begin{aligned} q_1^2(\chi, \tau) &= I_0\ \mathrm{sech}^2[B(\chi + \tau)] = I_0\ \mathrm{sech}^2(Bx) \\ q_2(\chi, \tau) &= \frac{B}{2}\tanh[B(\chi + \tau)] = \frac{B}{2}\tanh(Bx)\,. \end{aligned} \tag{11.46}$$

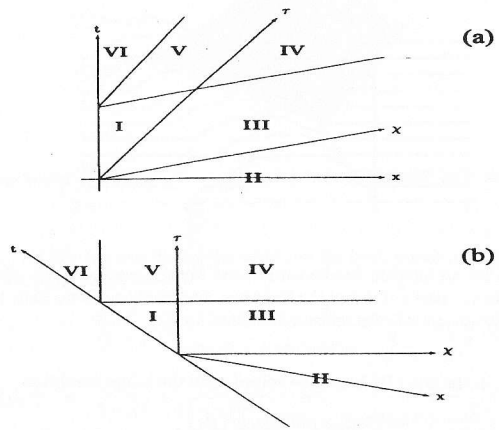

Figure 11.1: Space–time regions I to VI of the solution for an initial square pulse at the fundamental frequency. In part (a) the lab coordinates (x,t) are taken as Cartesian ones while in part (b) the same holds for the characteristic coordinates (χ, τ). The interaction occurs in the regions I and II. There is no field in II and VI while in IV and V there is free propagation of the harmonic wave.

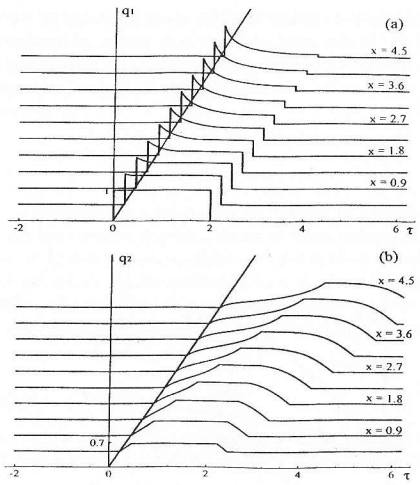

Figure 11.2: Solution for an incident fundamental wave being a square pulse. Part (a) shows the fundamental amplitude q_1 , part (b) shows the harmonic amplitude q_2. Note that, for $x = 0$, it holds $\tau = \nu t$ with ν being the group velocity mismatch defined by Eq. (11.8).

The Goursat problem in the strip III has to be solved with the initial condition

$$q_{10}^2(\tau) = I_0 \mathrm{sech}^2(B\tau) \; , \tag{11.47}$$

thus leading to the solution

$$\begin{aligned} q_1^2(\chi,\tau) &= \frac{I_0}{[\cosh(B\tau) + B\chi \sinh(B\tau)]^2} \\ q_2(\chi,\tau) &= \frac{B}{2[B\chi + \coth(B\tau)]} \; . \end{aligned} \tag{11.48}$$

The complete solution is depicted in Fig.11.2

11.3.2 Lorentzian Pulse

Let us now consider, as a fundamental wave at the boundary $x = 0$, a Lorentzian pulse, that is, a pulse whose intensity is given by

$$I_1(\tau) = \frac{1}{1+\tau^2} \; . \tag{11.49}$$

As one can easily verify, such a pulse corresponds to the following "wave-function"

$$\phi(\tau) = 1 + \tau^2 \; . \tag{11.50}$$

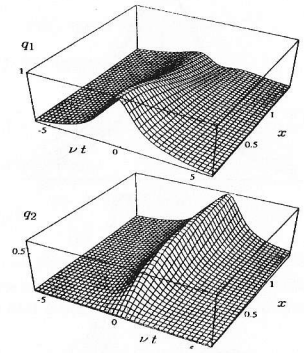

Figure 11.3: Amplitudes q_1 and q_2 for a Lorentzian initial intensity $|q_1|^2$ at the fundamental frequency.

Starting from Eq. (11.50) one can derive the solutions for both waves in an arbitrary cross section of the nonlinear medium, which are

$$\begin{aligned} q_1^2(\chi,\tau) &= \frac{1}{(1+\chi^2)^2} \frac{1}{(\arctan\chi + \arctan\tau + \frac{\chi}{1+\chi^2} + \frac{1}{\tau})^2} \frac{1}{\tau^2(1+\tau^2)} \\ q_2(\chi,\tau) &= \frac{\chi}{1+\chi^2} + \frac{1}{(1+\chi^2)^2} \frac{1}{(\arctan\chi + \arctan\tau + \frac{\chi}{1+\chi^2} + \frac{1}{\tau})} . \end{aligned} \tag{11.51}$$

This solution is depicted in Fig. 11.3

11.3.3 Squared Lorentzian

Here we consider a pulse for which the fundamental wave amplitude, at the boundary, has itself a Lorentzian shape. The intensity is thus a squared Lorentzian given by

$$I_1(\tau) = \frac{I_0}{2(1+\tau^2)^2} . \tag{11.52}$$

This pulse corresponds to the following wave function

$$\phi(\tau) = (1+\tau^2)^{1/2} \begin{cases} \cos[\alpha \arctan(\tau)] & , \; 1 - I_0 = \alpha^2 > 0 \\ 1 & , \; I_0 = 1 \\ \cosh[\beta \arctan(\tau)] & , \; I_0 - 1 = \beta^2 > 0 \end{cases} \tag{11.53}$$

from which we find

$$F(\chi) = \begin{cases} -\frac{1}{\alpha} \tan[\alpha \arctan(\chi)] \\ -\arctan(\chi) \\ -\frac{1}{\beta} \tanh[\beta \arctan(\chi)] \end{cases} \tag{11.54}$$

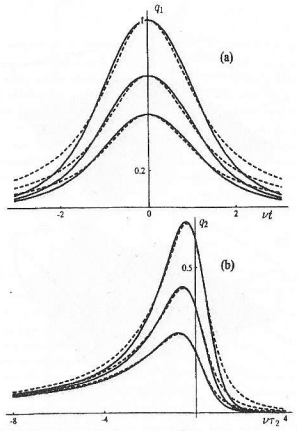

Figure 11.4: Solutions for a squared Lorentzian initial pulse intensity (dashed lines) are compared with solutions where the initial intensity is approximately a sech^2 shape (solid lines). Here, only the initial amplitudes q_1 (part a) and the asymptotic harmonic amplitudes q_2 (part b) are depicted. For the three examples, the initial fundamental pulse shapes differ in their amplitudes, while the half–width is the same for all these pulses.

The outgoing second harmonic wave is strongly dependent on the peak field intensity I_0. Three regions can be distinguished: very low ($I_0 < 1$), intermediate ($I_0 = 1$) and higher (but still perturbative) ($I_0 > 1$) intensities. For the intermediate case the propagated solutions for the two waves in the medium have the particularly simple form

$$\begin{aligned} q_1^2(\chi,\tau) &= \frac{1}{2(1+\chi^2)}\frac{1}{(\arctan(\chi)+\arctan(\tau)+\frac{1}{\tau})^2}\frac{1}{\tau^2(1+\tau^2)} \\ q_2(\chi,\tau) &= \frac{\chi}{2(1+\chi^2)}) + \frac{1}{2(1+\chi^2)}\frac{1}{(\arctan(\chi)+\arctan(\tau)+\frac{1}{\tau})} \end{aligned} \tag{11.55}$$

The solutions for $I_0 > 1$ and for $I_0 < 1$ can be given as well by substitution of (11.53) and (11.54) in (11.36) and (11.37) . The explicit formulas are rather messy, however, and therefore will not be presented here. The problem for $I_0 > 1$ was already solved by Akhmanov et al. [162]. In Fig. 11.4 we show three examples of initial q_1- pulses (upper part), together with the corresponding asymptotic q_2- pulses (lower part), for $I_0 = 2$ (upper curve), $I_0 = 1$ (intermediate curve) and $I_0 = 0.5$ (lower curve) .

11.3.4 Exponentially decaying pulses

In examples treated in previous subsections (as well in the next one) the solutions can be explicitly obtained in analytic form. It seems, however, impossible to do the same for an initial pulse with an

exponentially decaying shape. Here we start from a particular choice of "wave functions"

$$\phi(\tau) = a + \log\left[b + \cosh^2(\tau)\right] , \tag{11.56}$$

which corresponds to an initial pulse shape given by

$$I_1(\tau) = \frac{4\left[1 + (1+2b)\cosh(2\tau)\right]}{\left[1+2+\cosh(2\tau)\right]^2\left[a + \log\left(b+\cosh^2(\tau)\right)\right)\right]} , \tag{11.57}$$

the latter exhibiting the exponential decay

$$I_1(t) \overset{|t|\to\infty}{\simeq} \frac{4(1+2b)}{|t|}\exp(-2|t|) : . \tag{11.58}$$

For this kind of pulse, we have no closed analytical solutions. However, the numerical solution is obtained by means of the quadrature of Eq. (11.32). An interesting application makes use of the fact that the free parameters a and b may be adjusted to approximate sech^2-shaped pulses of the form

$$\tilde{I}_1(\tau) = \tilde{I}_0\,\mathrm{sech}^2(\tau) . \tag{11.59}$$

This pulse shape is obviously of experimental interest, since it represents the output of many laser systems. As an example, by choosing $(a,b) = (3.45, 0.122)$, $(1.36, 0.257)$ and $(0.176, 0.579)$ both maxima and half-widths of $I_1(\tau)$ coincide with those of $\tilde{I}_1$ with $\tilde{I}_0 = 0.25, 0.5, 1$ respectively. In Fig.11.4, the initial pulses and the asymptotic harmonic pulses are depicted, in comparison with the corresponding curves of the squared Lorentzian pulse. It can be seen that the trailing edge of the q_2- pulse is steeper for the sech^2–pulse than for the squared Lorentzian. Apart from that, no striking difference can be seen between these shapes.

11.3.5 An asymmetrical pulse

Here we will give the complete analytical solution for a particular asymmetrical initial pulse

$$I_1(\tau) = \frac{1}{2}\frac{1}{1+\tau^2}\left(1 - \frac{\epsilon\tau}{\sqrt{1+\tau^2}}\right) , \epsilon = \pm 1 . \tag{11.60}$$

For $\epsilon = +1$ the asymptotic behavior is given by

$$I_1 \to (1/4\tau^4) , \tau \to +\infty \quad ; \quad I_1 \to (1/\tau^2) , \tau \to -\infty$$

and vice versa for $\epsilon = -1$. In other words., the two pulses can be obtained one from the other by the transformation $\tau \to -\tau$. The corresponding "wave function" is given by

$$\phi(\tau) = \sqrt{1+\tau^2} + \epsilon\tau , \tag{11.61}$$

and the function F by

$$F(\chi) = \chi(1 + \frac{2}{3}\chi^2) + \frac{2\epsilon}{3}\left[(1+\chi^2)^{3/2} - 1)\right] . \tag{11.62}$$

Through Eqs. (11.15,11.16) we eventually arrive at the complete solution. The asymptotic shape of the harmonic wave is given by the rather simple formulae

$$q_2(\chi, \tau\to\infty) = \frac{1}{2\sqrt{1+\chi^2}} , \epsilon = +1 \tag{11.63}$$

$$q_2(\chi, \tau\to\infty) = \frac{3}{2}\frac{1}{\sqrt{1+\chi^2}-\chi} - \frac{1}{2\sqrt{1+\chi^2}}, \epsilon = -1 . \tag{11.64}$$

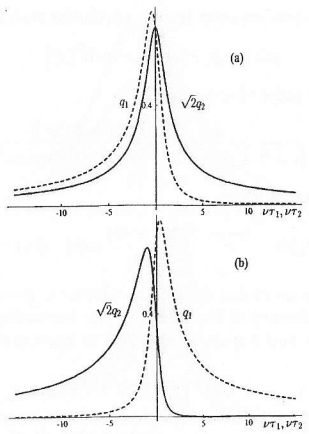

Figure 11.5: For two asymmetric initial pulses (dashed lines), one being the mirror image of the other, the asymptotic harmonic waves (solid lines) are given. Parts (a) and (b) correspond respectively to $\epsilon = +1$ and $\epsilon = -1$. The factor $\sqrt{2}$ was introduced for normalization purposes with respect to the energy (c.f. the text).

It is worth noticing that here two initial pulses, one being the time–reversed image of the other, yield quite different results. In particular the asymptotic pulse is symmetric for $\epsilon = +1$, but asymmetric for $\epsilon = -1$, see Fig. 11.5. For a quantitative comparison of the incident fundamental wave with the asymptotic harmonic wave in one and the same diagram, the respective electric field envelopes E_1, E_2 are more appropriate than our amplitudes q_1, q_2. (We recall that $|q_k|^2 \propto$ photon current densities). Due to the fact that $E_1/E_2 = q_1/\sqrt{2}q_2$ we have introduced the multiplicative factor $\sqrt{2}$ in the figure.

11.4 Conclusion

We have treated second harmonic generation in one dimension with amplitude–modulated pulses where the fundamental wave was the only incident pulse. We have shown how to reduce this problem to that of solving a zero-eigenvalue Schrödinger equation, the initial pulse shape being formally a repulsive potential.

Instead of starting from a specified pulse shape, we took a properly chosen multi-parametric set of "wave functions" $\phi(\tau)$ and easily computed the corresponding set of potentials. The free parameters of these solutions can be used to approximate pulse shapes of interest. To give a complete SHG solution, this method requires at most the single numerical integration of Eq. (11.32).

Using this approach we were able to obtain solutions for initial pulses approximately of a sech^2-shape with very little numerical effort. We also provide fully analytical solutions for several cases of interest, among these the well–known solutions found by Akhmanov et al. [162], initial square pulses, and asymmetrical initial pulses. Using a particular example, we have demonstrated that two

asymmetric initial pulses, differing only in the time orientation, give rise to quite different solutions.

We believe that the method introduced here should be useful for optimizing SHG and achieving suitable pulse–shaping in a broad range of working conditions.

Chapter 12

Summary

This thesis addresses the following optical phenomena: High-harmonic generation (Part I), atomic stabilization (Part II) and second harmonic generation with short pulses (Part III). The phenomena discussed in Parts I and II occur for very intense laser fields. Concerning high-harmonic generation, we compared several existing models, namely the fully numerical solution of the time-dependent Schrödinger equation (TDSE), the three-step model and the two-level atom (all of which are discussed in Chapter 4), using mainly numerical methods, with the following results:

In Chapter 5 we investigate the time profile of high-harmonic generation with monochromatic driving fields for an atom with a single bound state, using the three-step model and the TDSE. We show that the main contributions to harmonic generation within a field cycle correspond to the semiclassical returning times of an electron to its parent ion.

Chapter 6 is an extension of this work to model potentials with more than one bound state. Using a time-dependent projection method, we observe that high-harmonic generation is a result of bound-free transitions, where the transitions involving the ground state play the most important role. The generation of low harmonics, however, is strongly dependent of the atomic internal structure. Particularly concerning an atom with two strongly-coupled bound states, we have shown that these harmonics are a result of transitions involving only bound states. We also find that, even for this case, a two-level atom yields a very poor description of the low harmonics.

In Chapter 7 we address HHG with bichromatic driving fields, investigating the validity of the three-step model and the existence of a simple cutoff law of the form $|\varepsilon_0| + \alpha U_p$. Sec. 7.1 is an extension of Chapter 5, using time-frequency analysis. Therein, we show that the main contributions to HHG within a field cycle corresponds to the predictions of the three-step model also in this case. Furthermore, the harmonic intensities strongly depend on the field at the time the electron left the atom, according to the quasi-static tunneling formula discussed in Appendix C. In Sec. 7.2, we show the absence of a simple cutoff law in the bichromatic case.

In Part II we perform a mathematical analysis of atomic stabilization, providing rigorous criteria for its presence or absence. According to the results of Chapter 9, stabilization is *always* absent if the momentum transfer is non-vanishing at the end of the pulse. These results are totally independent of the pulse shape, of the pulse frequency, or of how smoothly the pulse is switched on or off.

Chapter 10 extends this analysis, showing that stabilization is in fact present when

1. The classical displacement and the momentum transfer are both vanishing at the end of the pulse

2. The frequency of the driving field tends to infinity, recovering the results of [19].

These conclusions follow from simple mathematical arguments, based on the Riemann Lebesgue theorem and the asymptotic behavior of the time evolution operator when $\omega \to \infty$ or $E_0 \to \infty$. Furthermore, we show the inadequacy of the Gordon Volkov solution for calculating ionization probabilities at intensities and frequencies usually considered in the literature, such that statements concerning this phenomenon within the Gordon Volkov framework are questionable.

In Part III, we provide a general analytical solution for second harmonic generation with amplitude-modulated pulses, within the weak-field regime. In particular, we show how propagation affects the pulse shape of the fundamental and harmonic waves, such that an asymmetrical pulse can lead to a symmetrical second harmonic and vice-versa.

Appendix A

Atomic units

In this appendix, we give the atomic units, widely used in this thesis and in high-intensity laser-atom physics.

1. Length: $r_0 = 1$ a.u. $= \hbar^2/me^2 = 0.53 \cdot 10^{-10} m$ (Bohr radius)

2. Charge: $e = 1$ a.u $= 1.602 \cdot 10^{-19} C$ (electron charge)

3. Energy:1 a.u.$= e^2/r_0 = 27.2eV$

4. Intensity: $I_0 = 1$ a.u. $= \epsilon_0 ce^2/2r_0^2 = 3.51 \cdot 10^{16} W/cm^2$

5. Mass(m): 1 a.u $= 9.1 \cdot 10^{-31} kg$ (electron mass)

6. Frequency: $\omega_0 = 1$ a.u.$= 4.13 \cdot 10^{16} s^{-1}$

7. Planck's constant$/2\pi = 6.5 \cdot 10^{-22}\ MeV \cdot\ s$. In atomic units this constant is equal to *one*.

Appendix B

Single-atom response in the weak-field regime

In this appendix, important aspects of ionization and harmonic generation for weak fields are briefly recalled. These conventional approaches are based on the perturbative series (10.1) resulting from the interaction of the Du Hamel formula (9.4). We take the external laser field as the perturbation, in opposition to the procedure used in the derivation of the Volkov series, such that the perturbative series is

$$U_j^S(t,t') = U_j^A(t,t') - i\int_{t'}^{t} ds\, U_j^A(t,s)\, H_j^F(s) U_j^A(s,t') \qquad \text{(B.1)}$$
$$- \int_{t'}^{t} ds \int_{s}^{t} ds'\, U_j^A(t,s')\, H_j^F(s') U_j^A(s',s) H_j^F(s) U_j^A(s,t') + \ldots$$

Here, U_j^A denotes the propagator concerning the field-free atomic Hamiltonian H_j^A and H_j^F the perturbation introduced by the field, which is given, in the length and velocity gauge, respectively by $H_l^F = \vec{\mathbf{r}} \cdot \vec{E}(t)$ and $H_v^F = -\vec{\mathbf{p}}.\vec{\mathbf{A}}(t) + \mathbf{A}^2(t)$. In both cases the n-th order term of the expansion (B.1) is proportional to the n-th power of the field amplitude, $(E_0)^n$. For weak fields, the series can be truncated and yields reliable results. For strong fields, however, it clearly diverges. The perturbative series above is the key point of the discussion that follows.

We consider now an atom initially in the state $|\psi(t=0)\rangle = |i\rangle$ subject to the perturbation H_l^F. The time-dependent atomic wave function is given by

$$|\psi(t)\rangle = U_j^S(t,0)\,|i\rangle = \sum_{np=0}^{\infty} \left|\psi^{(np)}(t)\right\rangle, \qquad \text{(B.2)}$$

where $\left|\psi^{(np)}(t)\right\rangle$ denotes the wave function to np-th order perturbation theory, obtained by truncating the time-evolution operator until the n-th order of (B.1). In the computations that follow, we take the Hamiltonian in the length gauge, the field to be of the form $E(t) = E_0 \sum_n \sin(\omega_n t)\hat{e}_x$, and an atom with m bound states, such that

$$|\psi(t)\rangle = e^{-i\varepsilon_i t}\,|i\rangle + i\sum_n E_0 \int_0^t ds e^{-iH_l^A(t-s)} \mathbf{x} \sin(\omega_n s) e^{-i\varepsilon_i s}\,|i\rangle \qquad \text{(B.3)}$$

$$-E_0^2 \sum_{n,n'} \sum_{\mu=0}^{m} \int_0^t ds \int_s^t ds' \, e^{-iH_I^{\Lambda}(t-s')} \, \mathbf{x} \sin(\omega_n s) \sin(\omega_{n'} s') \, |\mu\rangle \langle\mu| \, e^{-i\varepsilon_\mu (s'-s)} \mathbf{x} e^{-i\varepsilon_i s} \, |i\rangle + \dots$$

B.1 Harmonic generation

In order to calculate the harmonic response, one needs the time-dependent dipole moment $\langle\psi(t)|\,\mathbf{x}\,|\psi(t)\rangle$. To first order perturbation theory, this quantity is given by

$$d^{(1)} = 2\,\mathrm{Re}\left\{ \sum_{\omega_n} \frac{E_0}{\omega_n} \sum_{\mu=0}^{m} e^{-i\omega_{\mu i} t} \, |x_{\mu i}|^2 F(t, \omega_{i\to\mu} - \omega_n) \right\}, \tag{B.4}$$

with

$$F(t, \omega_{i\to\mu} - \omega_n) = \frac{e^{i/2(\omega_{\mu i} - \omega)t} \sin[(\omega_{i\to\mu} - \omega_n)t/2]}{(\omega_{i\to\mu} - \omega_n)t/2} - \frac{e^{i/2(\omega_{\mu i} + \omega)t} \sin[(\omega_{i\to\mu} + \omega_n)t/2]}{(\omega_{i\to\mu} + \omega_n)t/2} \tag{B.5}$$

Here we introduced the notation $\langle i|\,\mathbf{x}\,|j\rangle = x_{ij}$ and $\omega_{j\to i} = \varepsilon_i - \varepsilon_j$. A quick inspection of (B.5) shows that the terms in brackets are sharply peaked around $\omega_n = \pm(\varepsilon_\mu - \varepsilon_i)$, such that only the terms satisfying this condition survives in the sum above. Physically, this means that a one-photon transition can couple a final state $|\mu\rangle$ to the initial state $|i\rangle$ if they are resonant or nearly resonant with the driving field. In other words, to first order perturbation theory, the atom responds linearly to the field. The positive and negative signs correspond to, respectively, one-photon absorption and stimulated emission processes. The higher-order perturbative terms yield the nonlinear response of the atom. The dipole moment to np-th order perturbation theory, $d^{(np)}$, is given by

$$d^{(np)} = \mathrm{Re}\left\{ \sum_{q=1}^{np} E_0^q \sum_{\text{all combinations of } \omega_q} \chi^{(q)}(\omega_1, .., \omega_q) e^{i\omega_1 t} ... e^{i\omega_q t}, \right\} \tag{B.6}$$

with the nonlinear susceptibility

$$\chi^{(q)}(\omega_1, .., \omega_q) = \sum_{\substack{\text{all intermediate} \\ \text{states } \mu_n}} \sum_{\substack{\text{all permutations} \\ \text{involving } \omega_q}} (\omega_1 + \omega_2 + ... + \omega_q) \times \frac{\langle i|\,\mathbf{x}\,|\mu_1\rangle \langle\mu_1|\,\mathbf{x}\,|\mu_2\rangle \dots \langle\mu_q|\,\mathbf{x}\,|i\rangle}{(\omega_{i\to\mu_1} - \mathfrak{P}_1(\omega_1..\omega_q))(\omega_{i\to\mu_2} - \mathfrak{P}_2(\omega_1..\omega_q))...(\omega_{\mu_{q\to i}} - \mathfrak{P}_q(\omega_1..\omega_q))} \tag{B.7}$$

The derivation of these formulae can be seen in detail in, for instance, [164]. In equations (B.6) and (B.7), both positive and negative frequencies are taken into account. There are $(q+1)!$ permutations involving the frequencies $\omega_0 ... \omega_q$[1]. The terms $\mathfrak{P}_j(\omega_1..\omega_q)$ correspond to the sum $\sum \omega_n$ until the j-th term of the chosen permutation[2]. Specifically concerning the generation of the qth harmonic of a monochromatic driving field, one must take (B.6) at least until q-th order, with the absorption of q photons of frequency ω and the emission of a single photon of frequency $q\omega$. The absorption of each low-frequency photon requires intermediate atomic states, which are connected by matrix elements of the form $\langle\mu_j|\,\mathbf{x}\,|\mu_i\rangle$. The emission of the harmonic photon is given by $\langle\mu_q|\,\mathbf{x}\,|i\rangle$. The operator $\mathbf{x}$

[1] For instance, concerning third harmonic generation, to third order perturbation theory there are four possible processes, which must be taken into account in (B.7).

[2] For instance, for a permutation $\mathfrak{P}(\omega_1, \omega_3)$, $\mathfrak{P}_1(\omega_1, \omega_3) = \omega_1$ and $\mathfrak{P}_2(\omega_1, \omega_3) = \omega_1 + \omega_3$. More details on these permutations can be found, for instance, in [173].

has odd parity. For the harmonic emission to take place, it is necessary that all matrix elements are non-vanishing. For isotropic systems, like a single atom, the Hamiltonian commutes with the parity operator, such that eigenstates have a definite parity. This implies that the matrix elements above are only nonvanishing if the states $|\mu_i\rangle$ and $|\mu_j\rangle$ are of opposite parities. In this case, harmonic emission is just possible if q is odd. Therefore, even harmonics are absent. For other systems, like for instance some crystals, due to the lack of inversion symmetry, the eigenstates do not have a definite parity, and the emission of even harmonics is possible.

This argument also serves to justify the absence of even harmonics for strong laser fields. The harmonic intensities are of course not given correctly, since the perturbative series in the field diverges.

B.2 Fermi's golden rule

In this case, we are interested in the transition probability from the bound state $|i\rangle$ to a continuum of states with energy ε_μ such that $\varepsilon_\mu \simeq \varepsilon_i$ to first order in standard perturbation theory. For a set of discrete states, this probability is defined as $\sum_{\mu, \varepsilon_\mu \simeq \varepsilon_i} \left| \langle\mu|\,\psi^{(1)}(t)\right\rangle \right|^2$, with $\left|\psi^{(1)}(t)\right\rangle$ being given by the first-order term of the expansion (B.2). For continuum states, one has

$$\sum_{\mu, \varepsilon_\mu \simeq \varepsilon_i} \left| \langle\mu|\,\psi^{(1)}(t)\right\rangle \right|^2 \to \int d\varepsilon_\mu \rho(\varepsilon_\mu) \left| \langle\mu|\,\psi^{(1)}(t)\right\rangle \right|^2, \tag{B.8}$$

where $\rho(\varepsilon_\mu)$ is the density of final states with energy between ε and $\varepsilon + d\varepsilon$. For the sake of simplicity, we consider here a monochromatic field of frequency ω. The first-order transition amplitude is given by

$$\langle\mu|\,\psi^{(1)}(t)\right\rangle = iE_0 e^{-i\varepsilon_\mu t} x_{ni} e^{i(\omega_{i\to\mu} - \omega)t/2} \frac{\sin[(\omega_{i\to\mu} - \omega)t/2]}{(\omega_{i\to\mu} - \omega)/2}. \tag{B.9}$$

Since physically it only makes sense that the atom absorbs a photon and goes to the continuum, we do not take the term corresponding to the emission of a photon into account. For very large times,

$$\frac{\sin^2[(\omega_{i\to\mu} - \omega)t/2]}{(\omega_{i\to\mu} - \omega)^2} \simeq \frac{\pi t}{2} \delta(\omega_{i\to\mu} - \omega), \tag{B.10}$$

such that the ionization probability is time-proportional and the ionization rate is given by

$$\frac{dP}{dt} = \frac{E_0^2 \pi^2}{4} |x_{\mu i}|^2 \, \rho(\varepsilon_\mu \simeq \varepsilon_i + \omega). \tag{B.11}$$

Equation (B.11) is known as "Fermi's golden rule", and it clearly shows the ionization rate as proportional to the square of the field strength. As already discussed in Part II, this is not true anymore in the strong-field regime.

Appendix C

The quasi-static tunneling formula

In this appendix, we shall briefly recall an important formula, initially derived for the Hydrogen atom in a static field [66]. This formula has also proven to yield a reasonable approximation for fields with very low frequencies [65], and has been widely used for describing tunneling processes in the quasi-static field regime. For the discussions in Part I, it will suffice to present a one-dimensional derivation of this formula. As a starting point, we take the stationary Schrödinger equation,

$$\left[-\frac{1}{2}\frac{d^2}{dx^2} + V(x) - E_0 x\right]\psi(x) = \varepsilon\psi(x), \tag{C.1}$$

where E_0, ε, and $V(x)$ denote, respectively the static field, the energy of the electron and the binding potential. One can regard (C.1) as describing an electron in the effective potential barrier $V_{eff}(x) = V(x) - E_0 x$. Let us take $x = x_1$ as a turning point and consider that, inside the barrier, for $x \geq x_0$, such that $\psi(x_0)$ is given, the WKB approximation is valid (this approximation is also discussed in [66]). Within this formalism, the wave function for the electron inside and outside the barrier is given approximately by

$$\psi(x) = \begin{cases} \frac{C}{\sqrt{p}}\exp(i\int_{x_1}^{x} p dx + i\frac{\pi}{4}), & x > x_1 \\ \frac{C}{\sqrt{|p|}}\exp\left(\left|\int_{x_1}^{x} p dx\right|\right), & x_0 < x < x_1 \end{cases}, \tag{C.2}$$

where the momentum $p(x) = \sqrt{2\varepsilon + 2E_0 x}$ for $x > x_0$(one should note that, inside the barrier, p is imaginary). One can calculate the constant C using the boundary condition at x_0, such that.

$$C = \sqrt{|p_0|}\psi(x_0)\exp\left(-\left|\int_{x_1}^{x_0} p dx\right|\right). \tag{C.3}$$

Here we denoted $p(x_0) = p_0$. This way, the probability current for $x > x_1$is given by

$$\Gamma = p\,|\psi(x)_{x>x_1}|^2 = |p_0|\,|\psi(x_0)|^2\exp\left(-\left|\int_{x_1}^{x_0} p dx\right|\right). \tag{C.4}$$

Now a further assumption is made on the wave function inside the barrier, namely that it decays exponentially with x, i.e., $\psi(x_0) = D_1\exp(-kx_0)$. Normally, $\psi(x_0)$ is determined by fitting a tail

of the wave function we are taking into account (for instance, for the bound state of the gaussian potential of chapter D_1 we performed a fit for a numerically calculated wave function $\varphi_0 =< x|0 >$). If we consider a short-range potential, such that even for strong fields $|E_0 x_0| \ll |\varepsilon|$, then

$$\Gamma = kD_1^2 \exp\left[-2(2|\varepsilon|)^{3/2}/3E_0\right]. \tag{C.5}$$

This probability current can also be viewed as the ionization rate, since $\int \Gamma dt = \int |\psi(x)|^2 dx$. To first approximation, for quasi-static (low frequency) fields, one takes $E_0 \to |E(t)|$. Clearly, as the frequency increases, this approximation gets inapplicable.

Appendix D

Numerical Methods

In this appendix, the numerical methods used in this thesis are briefly discussed.The inverse iteration and the Crank Nicolson methods are the main structure of the TDSE solution used in Chapters 5, 6 and 7. The Runge Kutta method is used in the investigation of the semiclassical return times (Chapters 5 and 7), and in the numerical integration of the Bloch equations for the two-level atom (Chapter 6). The six point integration method is used for calculating quadratures throughout Part I, which are necessary, for instance, in the simulations involving the three-step model (Chapter 5), or in the time-dependent projections (Chapter 6).

D.1 Inverse Iteration Method

The initial wave function$|\psi(t=0)\rangle = |0\rangle$ corresponds to the ground state, and will be propagated in time within the TDSE framework is calculated solving the stationary Schrödinger equation

$$H^A |\varphi_0\rangle = \varepsilon_0 |0\rangle, \tag{D.1}$$

with H^A being the atomic Hamiltonian of Chapter 2 for a one-dimensional "atom" confined in a box of length L (the distinction between this Hamiltonian in the length and velocity gauges, H_l^A and H_v^A, is only necessary when the external field is present). We are mainly interested in a fully numerical solution for the eigenvalue equation above, since (D.1) is analytically solvable only for very few potentials. Equation (D.1) is solved in the configuration space through the inverse iteration method. This numerical method requires an approximate eigenvalue ε_0' and an initial guess function $\varphi_G(x)$, which will be taken as a first step for approximating the eigenfunction $\varphi_0(x) = \langle x\,|0\rangle$. The approximated eigenvalue is found by diagonalizing the matrix $H^A - \varepsilon_n$. These parameters are inserted in the equation

$$\left(H^A - \varepsilon_0'\right)\varphi_0(x) = \varphi_G(x), \tag{D.2}$$

which is solved iteratively: the function $\varphi_0^{(n)}(x)$ at the n-th iterative step will now be used as the guess function $\varphi_G^{(n+1)}(x)$ in the next step. We take the guess function for the first step as $\varphi_G(x) = \cos(x/L)$, or $\varphi_G(x) = \sin(x/L)$, depending on the parity of the bound state in question. For instance, for the ground state, which is even, we take the first choice of $\varphi_G(x)$. At each iteration step, the eigenfunction $\varphi_0(x)$ is normalized to one.Within this iterative scheme, the eigenvalues of the successive steps are related by

$$\varepsilon_0^{(n+1)} = \varepsilon_0^{(n)} + \frac{1}{\left\langle \varphi_G^{(n)} \,|0^{(n)}\right\rangle}. \tag{D.3}$$

Particularly for the atomic Hamiltonian

$$H^A = -\frac{1}{2}\frac{d^2}{dx^2} + V(x), \tag{D.4}$$

considering a discrete grid in the variable x, one can write, at $x = x_j$,

$$H^A\varphi_0(x_j) = -\frac{\varphi_0(x_{j+1}) - 2\varphi_0(x_j) + \varphi_0(x_{j-1})}{2\,(\Delta x)^2} + V(x_j)\varphi_0(x_j), \tag{D.5}$$

where Δx is the grid spacing and $x_{j\pm1} = x_j \pm \Delta x$. Inserting (D.5) in (D.2), one obtains a system of linear equations with nonzero elements only in the main diagonal plus or minus one column. Such systems, known as "tridiagonal systems", are given in general by

$$\begin{pmatrix} \beta_1 & \gamma_1 & \dots & 0 \\ \alpha_1 & \beta_2 & \ddots & \vdots \\ \vdots & \ddots & \ddots & \gamma_{n-1} \\ 0 & \dots & \alpha_n & \beta_n \end{pmatrix} \begin{pmatrix} u_1 \\ u_2 \\ \vdots \\ u_n \end{pmatrix} = \begin{pmatrix} r_1 \\ r_2 \\ \vdots \\ r_n \end{pmatrix}. \tag{D.6}$$

Concerning our specific problem, $u_j = \varphi_0(x_j)$, $r_j = \varphi_G(x_j)$, $\alpha_j = \gamma_j = -1/2(\Delta x)^2$ and $\beta_j = 1/(\Delta x)^2 + V(x_j) - \varepsilon_0'$. These systems can be easily solved numerically using standard subroutines (see e.g. subroutine "tridag" in [172]).

D.2 Crank Nicolson Method

The initial wave function $\varphi_0(x)$ found using the inverse iteration method must now be propagated in time. For that, the time-dependent Schrödinger equation (2.1) must be solved numerically. The most popular way of doing this is the Crank Nicolson method. Its main advantage lies on its stability for all values of the time increment used.

Taking the Hamiltonian (4.31) in the configuration space, (2.1) is written as the partial differential equation

$$i\frac{\partial\psi(x,t)}{\partial t} = \left[-\frac{1}{2}\frac{\partial^2}{\partial x^2} + iA(t)\frac{\partial}{\partial x} + V(x)\right]\psi(x,t). \tag{D.7}$$

The formal time-propagated solution of this equation is

$$\psi(x,t) = e^{-iHt}\psi(x,0). \tag{D.8}$$

The time evolution operator, for a time increment Δt, is discretized using Cayley's form[1]. This approximation is second-order accurate in Δt.

$$e^{-iH\Delta t} \simeq \frac{1 - iH\Delta t/2}{1 + iH\Delta t/2} \tag{D.9}$$

Using (D.9), one can write the scheme used in the time propagation,

$$\left(1 + i\frac{H\Delta t}{2}\right)\psi(x, t+\Delta t) = \left(1 - i\frac{H\Delta t}{2}\right)\psi(x,t). \tag{D.10}$$

[1] One of the main differences in the propagation methods concerns this discretization. A few examples can be seen, for instance, in [172].

The discretized Hamiltonian is written, for fixed $x = x_j$, as

$$\begin{aligned} H(t)\psi(x,t) &= -\frac{\psi(x_{j+1},t) - 2\psi(x_j,t) + \psi(x_{j-1},t)}{2\,(\Delta x)^2} \\ &\quad + iA(t)\left[\frac{\psi(x_{j+1},t) - \psi(x_{j-1},t)}{2\Delta x}\right] + V(x_j)\psi(x_j,t). \end{aligned} \tag{D.11}$$

Substituting this expression in (D.10), one obtains the tridiagonal system with

$$\alpha_j = -i\frac{\Delta t}{4\,(\Delta x)^2} - \frac{A(t)\Delta t}{4\Delta x}, \tag{D.12}$$

$$\beta_j = i\frac{\Delta t}{2\,(\Delta x)^2} + 1 + i\frac{\Delta t}{2}V(x_j) \tag{D.13}$$

$$\gamma_j = -i\frac{\Delta t}{4\,(\Delta x)^2} + \frac{A(t)\Delta t}{4\Delta x} \tag{D.14}$$

and

$$\begin{aligned} r_j &= \psi(x_{j+1},t)\left[i\frac{\Delta t}{4\,(\Delta x)^2} + \frac{A(t)\Delta t}{4\Delta x}\right] \\ &\quad + \psi(x_j,t)\left[-i\frac{\Delta t}{2\,(\Delta x)^2} + 1 - i\frac{\Delta t}{2}V(x_j)\right] + \psi(x_{j-1},t)\left[i\frac{\Delta t}{4\,(\Delta x)^2} - \frac{A(t)\Delta t}{4\Delta x}\right] \end{aligned} \tag{D.15}$$

which is, as in the previous section, solved according to [172].

D.3 Runge-Kutta Method

This is a typical method used for solving a set of n coupled first-order ordinary differential equations of the generic form

$$\frac{dy_n}{dx} = f_i(x, y_i, ..., y_n), \tag{D.16}$$

to which any problem involving ordinary differential equations can be reduced. In this thesis, such problems occur twice:

- In the computation of the bound-state amplitudes of a two-level atom as functions of time, solving the Bloch equations (4.27) given in Sec.4.2. These equations are given in the form D.16, with the initial condition that the atom is in the ground state, i.e.,

$$C_1(0) = 0; C_0(0) = 1. \tag{D.17}$$

- In the integration of the equation of motion of a classical electron in an external field, where the second-order equation (4.3) can be rewritten as

$$\begin{aligned} \frac{dx}{dt} &= v \\ \frac{dv}{dt} &= -\frac{dV(x)}{dx} + E(t). \end{aligned} \tag{D.18}$$

To first approximation, the influence of the binding potential is neglected. The initial conditions are given by the assumption that the electron leaves the atom at $t = t_0$ with zero velocity. In case the potential is taken into account, the initial velocity is given by $\sqrt{2|\varepsilon_0|}$. In order words,

$$\begin{aligned} x(t_0) &= 0 \\ v(t_0) &= \begin{cases} 0, & V(x) = 0 \\ \sqrt{2|\varepsilon_0|}, & V(x) \neq 0 \end{cases} . \end{aligned} \tag{D.19}$$

This initial time is varied then over a field period, and, within the time propagation, when the condition $x(t) = 0$ is satisfied, the return time t_1 and the corresponding kinetic energy are stored.

In general, in Runge Kutta methods, the derivative of a function is evaluated at several "trial points", taken between two consecutive points of the grid, such that these are used to compute the function at the next point of the grid. Concerning the fourth-order Runge-Kutta method, which is used in this work, the derivative is evaluated four times: once at a n-th and at the n+1-th points of the grid, and twice at trial midpoints. More precisely, we take

$$\begin{aligned} k_1 &= \Delta x f(x_n, y_n) \\ k_2 &= \Delta x f(x_n + \Delta x/2, y_n + k_1/2) \\ k_3 &= \Delta x f(x_n + \Delta x/2, y_n + k_2/2) \\ k_4 &= \Delta x f(x_n + \Delta x, y_n + k_3), \end{aligned} \tag{D.20}$$

with the derivatives denoted by k_i and the increment by Δx, such that the function at the next point of the grid is given by

$$y_{n+1} = y_n + \frac{k_1}{6} + \frac{k_2}{3} + \frac{k_3}{3} + \frac{k_4}{6} + O(\Delta x^5). \tag{D.21}$$

D.4 Six-point integration method

This method was used in the computation of several integrals in this thesis, for instance:

- The average dipole acceleration $\ddot{x}(t) = \langle\psi(t)|\ \ddot{\mathbf{x}}\ |\psi(t)\rangle$ in the TDSE computation (see also Eq. (4.33)), as well as its time-dependent projections (Chapter 6)
- The Fourier and Gabor transforms in Chapters 5, 6 and 7.
- The time integral (4.18) in order to compute the three-step model dipole moment (Chapter 5).

The idea behind the six-point integration method is very simple: Let us consider a function $f(x)$, which must be integrated in the interval $[a, b]$. The increment in x is given by Δx. We divide $[a, b]$ in several subintervals, such that the width of each interval is $\Delta\xi = 5\Delta x$. The integral $\int_a^b f(x)dx$ is the sum of the integrals calculated in each subinterval, which are approximated by

$$\int_{\xi}^{\xi+\Delta\xi} f(x)dx \simeq C_1 \left\{19\left[f_0 + f_5\right] + 75\left[f_1 + f_4\right] + 50\left[f_3 + f_2\right]\right\}, \tag{D.22}$$

where we used the notation $f_n = f(x + n\Delta x)$. Here, we introduced the normalizing constant $C_1 = 5\Delta x/288$.

Appendix E

Hydrogen matrix elements

In this appendix we will provide the explicit calculation of the term

$$N^2(\vec{\zeta}, \psi) = \langle\psi, V(\vec{r})^2\psi\rangle + \langle\psi, V(\vec{r} - \vec{\zeta})^2\psi\rangle - 2\langle\psi, V(\vec{r} - \vec{\zeta})V(\vec{r})\psi\rangle \tag{E.1}$$

For $\psi = \psi_{nlm}$ the first term is well known to equal $\frac{1}{n^3(l+1/2)}$ [138]. We did not find a computation for the matrix element involving the Coulomb potential in the Kramers-Henneberger frame in the literature and will therefore present it here. Starting with the familiar expansion of the shifted Coulomb potential in terms of spherical harmonics

$$\frac{1}{|\vec{r} - \vec{\zeta}|} = \sum_{l=0}^{\infty} \left(\frac{r_<^l}{r_>^{l+1}}\right) \sqrt{\frac{4\pi}{2l+1}} Y_{l\,0}(\theta, \phi) \tag{E.2}$$

where $r_< = Min(|\vec{r}|, |\vec{\zeta}|)$ and $r_> = Max(|\vec{r}|, |\vec{\zeta}|)$, we obtain

$$\begin{aligned} \langle\Psi_{nlm}|\ |\vec{r} - \vec{\zeta}|^{-1}\ |\vec{r}|^{-1}|\Psi_{nlm}\rangle &= \sum_{l'=0}^{\infty} \int d\Omega Y_{l\,m}^* Y_{l'\,0} Y_{l\,m} \sqrt{\frac{4\pi}{2l'+1}} \\ &\left(\int_0^{|\vec{\zeta}|} dr \left(\frac{r}{|\vec{\zeta}|}\right)^{l'+1} R_{nl}^2 + \int_{|\vec{\zeta}|}^{\infty} dr \left(\frac{|\vec{\zeta}|}{r}\right)^{l'} R_{nl}^2\right) \end{aligned}$$

which by the well known formula from angular momentum theory

$$\int d\Omega Y_{l\,m}^* Y_{l_1\,m_1} Y_{l_2\,m_2} = \sqrt{\frac{(2l_1+1)(2l_2+1)}{4\pi(2l+1)}} \langle l_1 l_2; 00|l0\rangle \langle l_1 l_2; m_1 m_2|lm\rangle \tag{E.3}$$

leads to

$$\sum_{l'=0}^{\infty} \langle ll'; 00|l0\rangle \langle ll'; m0|lm\rangle \left(\int_0^{|\vec{\zeta}|} dr \left(\frac{r}{|\vec{\zeta}|}\right)^{l'+1} R_{nl}^2 + \int_{|\vec{\zeta}|}^{\infty} dr \left(\frac{|\vec{\zeta}|}{r}\right)^{l'} R_{nl}^2\right) . \tag{E.4}$$

Here $\langle l_1 l_2; m_1 m_2|lm\rangle$ denote the Wigner or Clebsch-Gordan coefficients in the usual conventions (see e.g. [174]).

We shall now consider the term

$$\langle\Psi_{nlm}|\ |\vec{r} - \vec{\zeta}|^{-2}\ |\Psi_{nlm}\rangle \tag{E.5}$$

Employing (E.2) and the formula

$$Y_{l_1 m_1} Y_{l_2 m_2} = \sqrt{\frac{(2l_1+1)(2l_2+1)}{4\pi}} \sum_{l'm'} \frac{1}{(2l'+1)} Y_{l'm'} \langle l_1 l_2; m_1 m_2 | l' m' \rangle \langle l_1 l_2; 00 | l' 0 \rangle$$

yields

$$\frac{1}{|\vec{r}-\vec{\zeta}|^2} = \sum_{k,l'} \sum_{\tilde{l}=|k-l'|}^{|k+l'|} \frac{r_<^{k+l'}}{r_>^{k+l'+2}} \sqrt{\frac{4\pi}{2\tilde{l}+1}} \langle kl'; 00 | \tilde{l}0 \rangle^2 Y_{\tilde{l}0} \ . \tag{E.6}$$

Once again applying (E.3) shows that (E.5) equals

$$\sum_{\tilde{l},\bar{l},l'} \langle \tilde{l} l'; 00 | \tilde{l}0 \rangle^2 \langle \bar{l} l; 0m | lm \rangle \langle \bar{l} l; 00 | l0 \rangle \left(\int_0^{|\vec{\zeta}|} dr \left(\frac{r}{|\vec{\zeta}|} \right)^{l'+\tilde{l}+2} R_{nl}^2 + \int_{|\vec{\zeta}|}^{\infty} dr \left(\frac{|\vec{\zeta}|}{r} \right)^{l'+\bar{l}} R_{nl}^2 \right) . \tag{E.7}$$

For s-states, i.e. ($l = 0$), we may carry out the sums over the Clebsch-Gordan coefficients easily. In (E.4) the only contribution comes from $l' = 0$ and we trivially obtain

$$\langle \Psi_{n00} | \ |\vec{r}-\vec{\zeta}|^{-1} \ |\vec{x}|^{-1} | \Psi_{n00} \rangle = \int_0^{|\vec{\zeta}|} dr \frac{r}{|\vec{\zeta}|} R_{n0}^2 + \int_{|\vec{\zeta}|}^{\infty} dr R_{n0}^2 \ . \tag{E.8}$$

In (E.7) the sum over $\bar{l}$ contributes only for $\bar{l} = 0$ and together with $\langle \tilde{l} l'; 00 | 00 \rangle^2 = \frac{\delta_{\tilde{l}l'}}{2\tilde{l}+1}$ it leads to

$$\langle \Psi_{n00} | \ |\vec{r}-\vec{\zeta}|^{-2} \ | \Psi_{n00} \rangle = \sum_{l=0}^{\infty} \frac{1}{2l+1} \left(\int_0^{|\vec{\zeta}|} dr \left(\frac{r}{|\vec{\zeta}|} \right)^{2l+2} R_{nl}^2 + \int_{|\vec{\zeta}|}^{\infty} dr \left(\frac{|\vec{\zeta}|}{r} \right)^{2l} R_{nl}^2 \right) . \tag{E.9}$$

We turn to the case $n = 1$ (with $\Psi_{100} = \frac{2}{\sqrt{4\pi}} e^{-r}$) for which (E.4) becomes

$$\langle \Psi_{100} | \ |\vec{r}-\vec{\zeta}|^{-1} \ |\vec{r}|^{-1} | \Psi_{100} \rangle = \frac{1 - e^{-2|\vec{\zeta}|}}{|\vec{\zeta}|} \ . \tag{E.10}$$

As consistency check one may consider the asymptotic behaviors $|\vec{\zeta}| \to \infty$ and $|\vec{\zeta}| \to 0$, which give, as expected, 0 and 2 respectively. Using the series expansion for the logarithm, (E.9) for $n = 1$ becomes

$$\langle \Psi_{100} | \ |\vec{r}-\vec{\zeta}|^{-2} \ | \Psi_{100} \rangle = \frac{2}{|\vec{\zeta}|} \left(\int_0^{|\vec{\zeta}|} dr \ln \left(\frac{|\vec{\zeta}|+r}{|\vec{\zeta}|-r} \right) r e^{-2r} + \int_{|\vec{\zeta}|}^{\infty} dr \ln \left(\frac{r+|\vec{\zeta}|}{r-|\vec{\zeta}|} \right) r e^{-2r} \right) . \tag{E.11}$$

Using then the integrals

$$\int dr \ln(1 \pm r) r e^{-2cr} = \frac{1}{4c^2} \Big((1 \mp 2c) e^{\pm 2cr} Ei\left(\mp 2c(1 \pm r)\right) - e^{-2cr} \left(1 + (1+2cr) \ln(1 \pm r)\right) \Big) \tag{E.12}$$

$$\int dr \ln(1 \pm r^{-1}) r e^{-2cr} = \frac{1}{4c^2} \Big((1 \mp 2c) e^{\pm 2cr} Ei\left(2c(\mp 1 - r)\right) - Ei(-2cr) - (1+2cr) e^{-2cr} \ln(1 \pm r^{-1}) \Big) \tag{E.13}$$

we obtain

$$\langle \Psi_{100} | \ |\vec{r}-\vec{\zeta}/2|^{-2} \ | \Psi_{100} \rangle = (1 - |\vec{\zeta}|^{-1}) e^{-|\vec{\zeta}|)} Ei(|\vec{\zeta}|) + (1 - |\vec{\zeta}|^{-1}) e^{|\vec{\zeta}|)} Ei(-|\vec{\zeta}|) \tag{E.14}$$

As a consistency check we may again consider the asymptotic behavior, that is $|\vec{\zeta}| \to 0$ and $|\vec{\zeta}| \to \infty$, which gives correctly 2 and 0, respectively. Assembling now (E.1), (E.10) and (E.14) gives as claimed (9.14). In the same fashion one may also compute $N(\vec{\zeta}, \psi_{nlm})$ for arbitrary n, l and m.

Appendix F

Convergence of the Volterra equation

In this appendix we discuss the convergence of the iterative solution of the Volterra equation (10.20), which after integrating the free term acquires the form

$$\psi_I(t) = \sqrt{\frac{\alpha}{2}} e^{i\frac{c(t)^2}{2t}} \left(U_{\frac{1}{2},\frac{1}{2}}(\Phi_-) + U_{\frac{1}{2},\frac{1}{2}}(\Phi_+) \right) + \alpha \sqrt{\frac{i}{2\pi}} \int_0^t ds \psi_I(s) \frac{e^{i\frac{c_{Ls}^2}{2(t-s)}}}{\sqrt{t-s}}. \tag{F.1}$$

It is crucial to note that unlike the Gordon-Volkov iterative series, this procedure always converges with some natural assumption on the functions involved. With an obvious identification we may write (F.1) in the general form

$$\psi(t) = g(t) + \alpha \int_0^t K(t,s)\psi(s)\, ds \quad . \tag{F.2}$$

We will now closely follow the line of argumentation in [151] and show that once the free term in (F.2) is absolutely integrable, i.e. $\left|\int g(t)dt\right| \leq \int |g(t)|\, dt$, the iterative procedure converges for all values of α. The proof serves to provide the necessary estimations of the higher terms, which we employ to justify the termination of the iteration.

Iterating (F.2) leads to

$$\psi(t) = g(t) + \sum_{n=1}^{\infty} \alpha^n \int_0^t K_n(t,s)\psi(s)\, ds = g(t) + \sum_{n=1}^{\infty} \psi_n(t), \tag{F.3}$$

where

$$K_n(t,s) = \int_0^t dx_1 \ldots \int_0^t dx_{n-1} K(t,x_1) \ldots K(x_{n-1},s) = \int_s^t dx K(t,x) K_{n-1}(x,s). \tag{F.4}$$

Here we assumed w.l.g. for the kernel $K(t,s) = 0$ for $s > t$ and furthermore that the kernel is bounded by some value of the form

$$|K(t,s)| \leq \frac{\kappa}{\sqrt{t-s}}\ , \tag{F.5}$$

that is we allow a weak singularity of the type which occurs in (F.1), we will now show by complete induction that for all n the bound

$$|K_n(t,s)| \leq \frac{\pi^{\frac{n}{2}}\kappa^n (t-s)^{\frac{n}{2}-1}}{\Gamma\left(\frac{n}{2}\right)} \tag{F.6}$$

holds. Considering now (F.4) for $n \to n+1$ we obtain upon the use of (F.5) and (F.6)

$$|K_{n+1}(t,s)| = \int_s^t dx K(t,x) K_n(x,s) \tag{F.7}$$

$$\leq \frac{\pi^{\frac{n}{2}}\kappa^{n+1}}{\Gamma\left(\frac{n}{2}\right)} \int_s^t dx \frac{(x-s)^{\frac{n}{2}-1}}{\sqrt{t-x}} = \frac{\pi^{\frac{n}{2}+\frac{1}{2}}\kappa^{n+1}(t-s)^{\frac{n}{2}-\frac{1}{2}}}{\Gamma\left(\frac{1}{2}+\frac{n}{2}\right)}, \tag{F.8}$$

which concludes the induction. Using the bound (F.6) we may estimate the terms in the expansion (F.3)

$$|\psi_n(t)| = \alpha^n \left| \int_0^t K_n(t,s)\psi(s)\, ds \right| \tag{F.9}$$

$$\leq \frac{\alpha^n \pi^{\frac{n}{2}} \kappa^n}{\Gamma\left(\frac{n}{2}\right)} \Lambda \int_0^t ds (t-s)^{\frac{n}{2}-1} = \frac{2\Lambda}{n\Gamma\left(\frac{n}{2}\right)} \left(\kappa\alpha\sqrt{\pi t}\right)^n \quad , \tag{F.10}$$

where Λ denotes an upper bound for the absolute value of the free term

$$|f(t)| \leq \Lambda \quad . \tag{F.11}$$

We will now show that the infinite sum in (F.3) is indeed convergent and satisfies the Cauchy criterium. For this purpose we carry out the Cauchy root test, i.e. we use the fact that if $\lim_{n\to\infty} (|\psi_n|)^{1/n} \leq 1$ the series $\sum_{n=1}^{\infty} \psi_n$ is absolutely convergent. Approximating in (F.10) the gamma function by Stirling's formula as $n \to \infty$

$$\Gamma\left(\frac{n}{2}\right) \sim \sqrt{2\pi} e^{-\frac{n}{2}} \left(\frac{n}{2}\right)^{\frac{n}{2}-\frac{1}{2}} \tag{F.12}$$

we obtain

$$\lim_{n\to\infty} (|\psi_n|)^{1/n} = \lim_{n\to\infty} \frac{\kappa\alpha\sqrt{\pi t}\Lambda^{\frac{1}{n}} 2^{\frac{1}{n}-\frac{1}{2}}}{e^{-\frac{1}{2}} n^{\frac{1}{n}} \pi^{\frac{1}{2n}} n^{\frac{1}{2}+\frac{1}{n}-\frac{1}{2n}}} = 0 \quad . \tag{F.13}$$

Hence the iterative procedure converges for <u>all</u> values of α.

For the particular Volterra equation which concerns us, namely (F.1), we have

$$\kappa = \frac{1}{\sqrt{2\pi}} \qquad \text{and} \qquad \Lambda = \sqrt{2\pi}\alpha, \tag{F.14}$$

where we used the fact that the confluent hypergeometric is bounded by $\left|U_{\frac{1}{2},\frac{1}{2}}(z)\right| \leq \sqrt{\pi}$. Hence in our case the upper bound in (F.10) acquires the form

$$|\psi_n(t)| \leq \sqrt{8\alpha\pi} \frac{1}{n\Gamma\left(\frac{n}{2}\right)} \left(\alpha\sqrt{t/2}\right)^n . \tag{F.15}$$

In particular we have

$$|\psi_1(t)| \leq 2t^{\frac{1}{2}}\alpha^{\frac{3}{2}} \quad , \quad |\psi_2(t)| \leq \sqrt{\frac{\pi}{2}} t\alpha^2, \quad |\psi_3(t)| \leq \frac{2}{3} t^{\frac{3}{2}} \alpha^{\frac{7}{2}}. \tag{F.16}$$

It is important to note that it is essentially the occurrence of the gamma function $\Gamma\left(\frac{n}{2}\right)$, which in (F.13) ensured the convergence and that this property is independent of the parameters α and t. However, in (F.16) we observe that for some choices of α and t this convergence might be quite slow and we are therefore restricted to particular values of these parameters if we want to have a reasonable approximation after only a few number of iterative steps. In order to obtain a general criterion by which one may decide at which order it will be safe to terminate the iteration, we should sum up all the remaining terms

$$\sum_{n=1}^{\infty} |\psi_n(t)| = \sqrt{2\alpha\pi} \left(2\exp(\alpha^2 t/2) - 1 - U_{\frac{1}{2},\frac{1}{2}}\left(\alpha^2 t/2\right)/\sqrt{\pi}\right) . \tag{F.17}$$

Hence the maximal relative error after the zeroth order reads

$$\mu := 2\sqrt{\pi} \left| \frac{\left(2\exp(\alpha^2 t/2) - 1 - U_{\frac{1}{2},\frac{1}{2}}\left(\alpha^2 t/2\right)/\sqrt{\pi}\right)}{\left(U_{\frac{1}{2},\frac{1}{2}}(\Phi_-) + U_{\frac{1}{2},\frac{1}{2}}(\Phi_+)\right)} \right| \quad . \tag{F.18}$$

Frame of this research and Acknowledgements

The work presented in this thesis was performed mainly at the *Technische Universität Berlin/Max Born Institut für Nichtlineare Optik and Kurzzeitspektroskopie* between July 1995 and September 1998, under the supervision of Prof. Dr. Wolfgang Sandner and Dr. Martin Dörr and with the collaboration of Dr. Wilhelm Becker. It also includes extensive collaborations with Dr. Andreas Fring and Prof. Dr. Robert Schrader, from the theory group of the *Freie Universität Berlin*, and with Dr. H. Steudel, Dr. M.G.A. Paris, Dr. O Steuernagel, from the *Humboldt Universität Berlin*, and Prof. Dr. A.M. Kamchatnov, from the *Institute of Spectroscopy of the Russian Academy of Sciences*. Parts of it can also be found in the following publications:

Part I:

Paper 1 C. Figueira de Morisson Faria, M. Dörr, and W. Sandner, *"Time profile of harmonic generation"*, *Phys. Rev. A* **55**, 3961 (1997) (reference [55])

Paper 2 C. Figueira de Morisson Faria, M. Dörr and W. Sandner, *"Importance of excited bound states in harmonic generation"*, *Phys. Rev. A* **58**, 2990 (1998) (reference [56])

Paper 3 C. Figueira de Morisson Faria, M. Dörr, W. Becker and W. Sandner, *"Time-frequency analysis of two-color high-harmonic generation"*, to appear in Phys. Rev. A (reference [57])

Paper 4 C. Figueira de Morisson Faria,W. Becker, M. Dörr and W. Sandner, *"Phase- and intensity dependence of the cutoffs in two-color high-harmonic generation"*, *Laser Phys.* **9**, 379 (1999).

Part II:

Paper 5 C. Figueira de Morisson Faria, A. Fring and R. Schrader, *"On the influence of pulse shapes on ionization probability"*, *J. Phys. B* **31**, 449 (1998) (reference [135])

Paper 6 C. Figueira de Morisson Faria, A. Fring and R. Schrader, *"Analytical treatment of stabilization"*, *Laser Phys.* **9**, 388 (1999).

Paper 7 C. Figueira de Morisson Faria, A. Fring and R. Schrader, *" Momentum transfer, displacement and stabilization"*, in preparation

Part III:

Paper 8 H. Steudel, C. Figueira de Morisson Faria, M.G.A. Paris, A.M. Kamchatnov and O. Steuernagel, *"Second harmonic generation: the solution for an amplitude-modulated initial pulse"*, *Opt. Comm.* **150**, 363 (1998).

Since scientific productivity is always related to very good collaborators, a lot of support and, not to forget, emotional stability, I shall now write a long acknowledgment list. All my thanks to:

Prof. Dr. Wolfgang Sandner, for accepting me in the group, his support in several scientific matters and his openess towards my parallel research activities, which originated Parts II and III of this thesis.

Dr. Martin Dörr for his supervision, accessibility, and for bearing a large amount of psycho-terror from my side since 1995, when I started working on high-harmonic generation with him. I must also say I profited very much from our work together, learning not only high-intensity laser physics, but also a lot of programming. Nowadays, being able to do both is never too much!

Dr. W. Becker for very useful discussions and hints on literature (concerning this thesis and my publications in general), the collaborations which resulted in Chapter 7 of this thesis and invaluable support inside the group.

R. Kopold for discussions concerning HHG in molecules, which were extremely useful for the interpretation of the results in Chapter 6.

G. Sommerer, for providing me useful information about the HHG experiments at the MBI (and of course some related pictures, one of which is seen in Chapter 3).

My collaborators at the FU-Berlin, Prof. Dr. R. Schrader and Dr. A. Fring, for learning a lot of interesting mathematics (and also how to fight with referees) within the more than stressful context of atomic stabilization along non-orthodox lines. I also think I would have never learned Mathematica without Chapter 9 (or, before that, Paper 5). To Andreas my ultra-especial thanks for the psychological/emotional support in all the hard periods of this Ph.D., and in many other situations which contradicted the well-known brazilian proverb "onde se ganha o pão não se come a carne". We know what we have been through!

My collaborators from Part III of this thesis, Dr. H. Steudel, Dr. M.G.A. Paris, Dr. O Steuernagel, and Prof. Dr. A.M. Kamchatnov (especially the first two), which at the time were part of the group 'Nichtklassische Strahlung' at the Max-Planck Institute, Berlin, and now are spread all over the world. Without them I would have had no idea of what to do with *low* harmonics. Our collaboration also taught me quite a bit about the Liouville equation and short pulse propagation. I also would like to thank Prof. Dr. H. Paul, at the HU-Berlin, for reference letters.

Dr. Stefan Henz, Dr. T.M. Kruel, Dr. M. Müller and Dr. S. Gatz for help with computers and related things, especially at the beginning of my Ph.D., when I was almost unix-illiterate.

The DAAD for the very effective financial support. The main difference between them and some brazilian foundations is that they actually pay. And every month!

My family, especially my mother, for emotional support, love and understanding, in all the maxima- and minima I sometimes went through. I am also deeply grateful to my parents for financial support at the beginning of this PhD, when I had to deal with a fully unreliable brazilian foundation. Still within the family context, I would like to thank my aunt Y.C. de Andrade Figueira for official translations of my documents.

And, finally, several people who indirectly helped: Dr. U. Eichmann and R. Schumann, concerning 'hot tips' which were useful for getting the equivalence of my brazilian degree, E. and S. Kendziorra, for filling out forms about my german skills and Dr. P. Mani for making the procedure of getting a health certificate (an important prerrequisite for obtaining german money) a lot more unbureaucratic and uncomplicated than it usually is.

Of course I can not forget Yin, who, without knowing, considerably helped me with my stress management, especially in the three months I spent writing up this thesis.

Bibliography

[1] For a review see, e.g., R. Eisberg and R. Resnick, *"Quantum Physics of Atoms, Molecules, Solids, Nuclei and Particles"* (J. Wiley & Sons, New York, 1974); T. Mayer-Kuckuk, *"Atomphysik"* (Teubner, Stuttgart, 1994).

[2] A. Einstein, *Ann. der Phys.* **17**, 132 (1905).

[3] M. Göppert-Mayer, *Ann. der Phys.* (Leipzig) **9**, 273 (1931).

[4] P.A. Franken, A.E. Hill, C.W. Peters and G. Weinreich, *Phys.Rev.Lett.* **7** , 118 (1961).

[5] W. Kaiser, C.G. B. Garret, *Phys. Rev. Lett.* **7**, 229 (1961).

[6] For a review, see, e.g., Y.R. Shen, *"The principles of nonlinear optics"* (J Wiley & Sons, New York, 1984).

[7] J.L. Hall, E.J. Robinson and L.M. Branscomb, *Phys. Rev. Lett.* **14**, 1013 (1965); G.S. Voronov and N.B. Delone, *Sov. Phys. JETP* **23**, 54 (1966); P. Agostini, G. Barjot, J.F. Bonnal, G. Mainfray, C. Manus and J. Morellec, *IEE J. Quantum Electron.* **QE-4**, 667 (1968).

[8] See, e.g., M. Gavrila eds., *"Atoms in Intense Laser Fields"* (Advances in Atomic, Molecular and Optical Physics, Academic, London, 1992).

[9] P. Agostini, E. Mevel, P. Breger, A. Migus and L.F DiMauro, *"Super Intense Laser-Atom Physics ", B. Piraux et al. eds.*, p. 155 (Plenum, New York, 1993).

[10] P. Gibbon and E. Förster, *Plasma Phys. Control. Fusion* **38**, 769 (1996); A. Pukhov, J. Meyer-ter-Vehn, *Phys. Rev. Lett.* **76**, 3975 (1996); ibid. **79**, 2686 1997).

[11] H. Reiss, *J. Math. Phys.* **3**, 59 (1962); N.B. Nahrozhnhy, *Sov. Phys. JETP* **20**, 622 (1967); C. Symanowski, V. Véniard, R. Taieb, A. Maquet and C.H. Keitel, *Phys. Rev. A* **56**, 3846 (1997); G. Pretzler, A. Saemann, A. Pukhov, D. Rudolph, T. Schätz, U. Schramm, P. Thirolf, D. Habs, J. Meyer-ter-Vehn, G.D. Tsakiris and K.J. Witte, *Phys. Rev. E* **58**, 1165 (1998).

[12] A. L'Huillier and Ph. Balcou, *Phys. Rev. Lett.* **70**, 774 (1993).

[13] See, e.g., A. Rundquist, C.G. Durfee III, Z. Chang, C. Herne, S. Backus, M.M. Murnane, H.C. Kapteyn, *Science* **280**, 1412 (1998); X. F. Wang, R. Fedoseyevs, G.D. Tsakiris, *Opt. Comm.* **146**, 363 (1998); I.P. Christov, M.M. Murnane and H.C. Kapteyn, *Phys. Rev. A* **57**, R2285 (1998).

[14] See, *e.g*, Stuart et al, *Opt. Lett.* **22**, 242 (1997).

[15] L.S. Brown and T.W.B. Kibble, *Phys.Rev.* **133**, 705 (1964); J.H. Eberly and A. Sleeper, *Phys. Rev.* **176**, 1570 (1968); A. Sarachik and E.S. Chappert, *Phys. Rev. D* **1**, 2738 (1970); A. Bugacov, M. Pont and R. Shakeshaft, *Phys. Rev. A* **48**, R4027 (1993); M. Protopapas, C.H. Keitel and P.L. Knight, *J. Phys. B* **29**, L591 (1996); N. Kylstra et al., *J. Phys. B* **30**, L449 (1997); U.W. Rathe, C.H. Keitel, M. Protopapas, and P.L. Knight, *J. Phys. B* **30**, L531 (1997).

[16] M. Ferray, A. L'Huillier, X.F. Li, L.A. Lompré, G. Mainfray and C. Manus, *J. Phys. B* **21**, L31(1988); X.F. Li, A. L'Huillier, M. Ferray, L.A. Lompré, and G. Mainfray, *Phys. Rev. A* **39**, 5751(1989).

[17] A. McPherson, G. Gibson, H. Jara, U. Johann, T. S. Luk, I. McIntyre, K. Boyer and C. K. Rhodes, *J. Opt. Soc. Am. B* **4**, 595 (1987); R. Rosman, G. Gibson, K. Boyer, H. Jara, T. S. Luk, I. A. McIntyre, A. McPherson, J. C. Solem and C. Rhodes, *J. Opt. Soc. Am. B* **5**, 1237 (1988).

[18] J.I. Gersten and M.H. Mittleman, *Phys. Rev. A* **10**, 74 (1974) and *J. Phys. B* **9**, 2561 (1976); S. Geltman and M.R. Teague, *J. Phys. B* **7**, L22 (1974).

[19] M. Gavrila and J.Z. Kaminski, *Phys. Rev. Lett.* **52**, 614 (1984).

[20] M.P. de Boer, J.H. Hoogenraad, R.B. Vrijen, L.D. Noordam and H.G. Muller, *Phys. Rev. Lett.* **71**, 3263 (1993); M.P. de Boer, J.H. Hoogenraad, R.B. Vrijen and L.D. Noordam, *Phys. Rev. A* **50,** 4133 (1994).

[21] N.J. van Druten, R.C. Constantinescu, J.M. Schins, H. Nieuwenhuize, and H.G. Muller, *Phys. Rev. A* **55**, 622 (1997).

[22] P. Salières, A. L'Huillier and M. Lewenstein, *Phys. Rev. Lett.* **75**, 3376 (1995); J. Peatross, M.V. Fedorov and K.C. Kulander, *J. Opt. Soc. Am. B* **12**, 863 (1995); P. Antoine, M. B. Gaarde, P. Salières, B. Carré, A. L'Huillier, M. Lewenstein, in: *Proceedings of "VIIth International Conference on Multiphoton Processes "*, P. Lambropoulos and H. Walther eds, p. 142 (IOP Publishing, Bristol, 1997); J. Zhou, J. Peatross, M. M. Murnane, H. C. Kapteyn and I. P. Christov, *Phys. Rev. Lett.* **76**, 752 (1996); P. Salières, T. Ditmire, M. D. Perry, A. L'Huillier and M. Lewenstein, *J. Phys. B* **29**, 4771 (1996).

[23] P. Dietrich, N. H. Burnett, M. Ivanov, and P. B. Corkum, *Phys. Rev. A* **50**, R3585 (1994); M. Lewenstein, P. Salières, and A. L'Huillier, *ibid.* **52**, 4747 (1995).

[24] T. Zuo, S. Chelkowski, and A. D. Bandrauk, *Phys. Rev. A* **48**,580 (1993); Y. Liang, S. Augst, S.L. Chin, Y. Beaudoin and M. Chaker, *J. Phys. B* **27**, 5119 (1994); D.J. Fraser, M.H.R. Hutchinson, J.P. Marangos, Y.L. Shao, J.W.G. Tisch and M. Castillejo, *J. Phys. B* **28**, L739 (1995); H. Sakai and K. Miyazaki, *Appl. Phys. B* **61**, 493 (1995); C. Lyngå, A. L'Huillier, and C.-G. Wahlström, *J. Phys. B* **29**, 3293 (1996); Y. Liang, A. Talebpour, C.Y. Chien, S. Augst and S.L.Chin, *J. Phys. B* **30**, 1369 (1997).

[25] R. Kopold, W. Becker and M. Kleber, *Phys. Rev. A* **58**, 4022 (1998).

[26] R. Kopold and W. Becker, *Laser Phys.* **9**, 398 (1999).

[27] See, e.g., K.T. Taylor, J. S. Parker, D. Dundas, E. Smyth, and S. Vivirito, in: *Proceedings of "VIIth International Conference on Multiphoton Processes "*, P. Lambropoulos and H. Walther eds., p. 56 (IOP Publishing, Bristol, 1997), F.H.M.Faisal and A. Becker, *ibid.*, p. 118, and references therein.

[28] C. A. Ullrich, S. Erhard, and E. K. U. Gross, *Proceedings of "Super Intense Laser-Atom Physics IV", H. G. Muller and M. V. Fedorov eds.*, p. 267 (Kluwer, Dordrecht, 1996).

[29] S.A. Akhmanov, V.A. Vysloukh, and A.S. Chirkin, *"Optics of Femtosecond Laser Pulses"* (American Institute of Physics, New York, 1992).

[30] W. Vogel and D. -G. Welsch, *"Lectures on Quantum Optics"*(Akademie Verlag, Berlin, 1994); H. Paul, *"Photonen"* (Teubner, Stuttgart, 1995).

[31] H.A Kramers, *Collected Scientific Papers* (North-Holland, Amsterdam, 1956); W.C. Henneberger, *Phys. Rev. Lett.,* **21,** 838 (1968).

[32] H.L. Cycon, R.G. Froese, W. Kirsch, W. and B. Simon, *"Schrödinger Operators"* (Springer, Berlin, 1987).

[33] A. de Bohan, P. Antoine, D.B. Milošević and B. Piraux, Phys. Rev. Lett. **81,** 1837 (1998).

[34] Q. Chen and I.B. Bernstein, *Phys. Rev. A* **47** 4099 (1993) .

[35] N. L. Manakov and V. D. Ovsyannikov, *Zh. Eksp. Teor. Fiz.* **79**, 1769 (1980) (*Sov. Phys. JETP* **52**, 895 (1980)).

[36] G. Sommerer, E. Mevel, H. Hollandt, D. Schulze, P. V. Nickles, G. Ulm and W. Sandner, *Opt. Comm.* **146**, 347 (1998); D. Schulze, M. Dörr, G. Sommerer, J. Ludwig, P.V.Nickles, T. Schlegel, W. Sandner, M. Drescher, U. Kleineberg and U. Heinzmann, *Phys. Rev. A* **57**(4), 3003 (1998); see also D. Schulze, PhD thesis, Technische Universität Berlin, 1998.

[37] N. Sarukura, K. Hata, T. Adachi, R. Nodomi, M. Watanabe, and S. Watanabe, *Phys. Rev. A* **43**, 1669 (1991).

[38] See, e.g., J.J. Macklin, J. D. Kmetec, and C. L. Gordon III, *Phys. Rev. Lett.* **70,** 766(1993); A. L'Huillier and Ph. Balcou, *Phys. Rev. Lett.* **70,** 774 (1993); M.D. Perry and G. Mourou, *Science* **264**, 917 (1994).

[39] J. Zhou, J. Peatross, M.M. Murnane, H.C. Kapteyn, and I. P. Christov, *Phys. Rev. Lett.* **76,** 752 (1996).

[40] M. Yu. Kuchiev, *JETP Lett.* **45** (7), 404 (1987); K. C. Kulander, K. J.Schafer , and J. L. Krause, in: *Proceedings of the SILAP conference*, B. Piraux et al. *eds.*(Plenum, New York, 1993); P. B. Corkum, *Phys. Rev. Lett.* **71**, 1994 (1993)

[41] M. Lewenstein, Ph. Balcou, M. Yu. Ivanov, A. L'Huillier and P. B. Corkum, *Phys. Rev. A* **49**, 2117 (1994); P. Salières, Ph. Antoine and M. Lewenstein, to appear in Adv. At. Mol. Phys. (1998).

[42] W. Becker, S. Long and J. K. McIver, *Phys. Rev.* A **41**, 4112 (1990) and **50**, 1540 (1994)

[43] B. Sundaram and P. Milonni, *Phys. Rev. A* **41**, 6571 (1990) ; L. Plaja and L. Roso-Franco, *J. Opt. Soc. Am. B* **9,** 2210 (1992); A. E. Kaplan and P. L. Shkolnikov, *Phys. Rev. A* **49**, 6571 (1994); F. I. Gauthey, C. H. Keitel, P. L. Knight and A. Maquet, *Phys. Rev. A* **52**, 525 (1995); S. de Luca and E. Fiordilino, *J. Phys. B* **29**, 3277 (1996).

[44] E. Conejero Jarque and L. Plaja, *J. Opt. Soc. Am. B* **13,** 2724 (1996).

[45] E. Conejero Jarque and L. Plaja, *J. Phys. B.* **31**, 1687 (1998).

[46] F. I. Gauthey, B. M. Garraway, and P. L. Knight, *Phys. Rev. A* **56**, 3093 (1997).

[47] S. Geltman, *J. Phys. B* **10**, 831 (1977); A. Goldberg and B. Shore, *J. Phys. B* **11**, 3339 (1978); E. J. Austin, *J. Phys. B* **12**, 4045 (1979).

[48] K.C. Kulander, *Phys. Rev. A* **35**, 445 (1987); M. Dörr and R. Sahkeshaft, *Phys. Rev. A* **38**, 543 (1988); B. W. Shore and K.C. Kulander, *Phys. Rev. Lett.* **62**, 524 (1989), and *J. Opt. Soc. Am. B* **7**, 502 (1990).

[49] J. L. Krause, K. J. Schafer, and K. C. Kulander, *Phys. Rev. Lett.* **68**, 3535 (1992).

[50] See *e.g.* M. Protopapas, C. H. Keitel and P. L Knight, *Rep. Prog. Phys.* **60**, 389 (1997).

[51] R.M. Potvilege and R. Shakeshaft, *Phys. Rev. A* **40**, 3061 (1989).

[52] S.C. Rae, K. Burnett and J. Cooper, *Phys. Rev. A* **50**, 3438 (1994).

[53] P. Antoine, B. Piraux and A. Maquet, *Phys. Rev.* A **51**, R1750 (1995); R. Taïeb, A. Maquet, P. Antoine and B. Piraux, in: *Proceedings of "Super Intense Laser-Atom Physics IV",* H.G. Muller and M.V. Fedorov *eds.*, 445 (Kluwer, Dordrecht, 1996); P. Antoine, B. Piraux, D. B. Milošević and M Gajda, *Phys. Rev.* A **54**, R1761 (1996)

[54] P. Antoine, A. L'Huillier, M. Lewenstein, *Phys. Rev. Lett.* **77**, 1234 (1996).

[55] C. Figueira de Morisson Faria, M. Dörr, and W. Sandner, *Phys. Rev. A* **55**, 3961 (1997).

[56] C. Figueira de Morisson Faria, M. Dörr, and W. Sandner, *Phys. Rev. A* **58**, 2990 (1998).

[57] C. Figueira de Morisson Faria, M. Dörr, W. Becker, and W. Sandner, submitted to Phys. Rev. A.

[58] M.B. Gaarde, PhD thesis, University of Copenhagen, Denmark, 1997.

[59] C. Kan, C. E. Kapjack, R. Rankin, and N. H. Burnett, *Phys. Rev. A* **52**, R4336 (1995).

[60] P. Salières, A. L'Huillier, P. Antoine and M. Lewenstein, Adv. At., Mol. Opt. Phys. **40B** (1998)

[61] Ph. Antoine, B. Piraux, D. B. Milošević, and M. Gajda, *Phys. Rev. A* **54**, R1761 (1996); P. Antoine, D. B. Milošević , A. L'Huillier, M. B. Gaarde, P. Salières, and M. Lewenstein, preprint.

[62] P. B. Corkum, N. H. Burnett, and M. Y. Ivanov, *Opt. Lett.* **19**, 1870 (1994); M. Ivanov, P. B. Corkum, T. Zuo, and A. Bandrauk, *Phys. Rev. Lett.* **74**, 2933 (1994).

[63] W. Brefeld and P. Gürtler, in *"Handbook on Synchrotron Radiation"*, vol. 4, eds.S. Ebashi, M. Koch and E. Rubinstein (Elsevier Science, Amsterdam, 1991).

[64] M.H. Key et al, in: *"Proceedings of the 5th International Conference on X-Ray Lasers"*, eds. S. Svanberg and C.-G Wahlström (IOP Publishing, Bristol, 1996).

[65] L.V. Keldysh, *Sov. Phys. JETP* **20,** 1307 (1965).

[66] See, e.g., L. D. Landau and E. M. Lifshitz, " *Quantum Mechanics*" (Pergamon Press, Oxford, 1977).

[67] G. G. Paulus, W. Becker and H. Walther, Phys. Rev. A **52**, 4043 (1995); A. Lohr, W. Becker, S. Long and J. K. McIver, *Proceedings of "Super Intense Laser-Atom Physics IV", H. G. Muller and M. V. Fedorov eds.*, 477 (Kluwer, Dordrecht, 1996).

[68] W. Becker, A. Lohr, M. Kleber and M. Lewenstein, *Phys. Rev. A* **56** (1), 645 (1997).

[69] See e.g. H. Goldstein, *"Classical Mechanics"* (Addison-Wesley, Massachussets,1980); for a specific discussion on the HHG problem see W. Becker, A. Lohr and M. Kleber, *Quantum Semiclass. Opt.* **7**, 423 (1995).

[70] M. Bellini, C. Lyngå, A. Tozzi, M. B. Gaarde, T. W. Hänsch, A. L'Huillier, and C.-G. Wahlström, *Phys. Rev. Lett.* **81**, 297 (1998).

[71] L. Allen and J. Eberly, "*Optical Resonance and Two-Level Atoms*"(Wiley, New York, 1975)

[72] B. W. Shore "*Theory of Coherent Atomic Excitation*" (Wiley; New York, 1990).

[73] K. Burnett, V.C. Reed, J. Cooper and P. L. Knight, *Phys. Rev. A* **45**, 3347 (1992).

[74] J.L. Krause, K. Schafer and K. Kulander, *Phys. Rev. A* **45**, 4998 (1992).

[75] D. Gabor, J. IEEE **93**, 429 (1946).

[76] I. Daubechies, *"Ten Lectures on Wavelets"* (Society for Industrial and Applied Mathematics, Philadelphia, 1992).

[77] See e.g. S.G. Malat, *"A Wavelet tour of Signal Processing"* (Academic Press, London, 1998) and references therein

[78] See *e.g.* M. Protopapas, D. G. Lappas, C. H. Keitel and P. L. Knight, *Phys. Rev. A* **53**, R2933 (1996).

[79] R. R. Schlicher, W. Becker, J. Bergou and M.O. Scully, in: *"Quantum Electrodynamics and Quantum Optics"*, A.O. Barut eds., p. 405 (Plenum,1984) and references therein

[80] See *e.g.* C. Leubner and P. Zoller, *J. Phys. B* **13,** 3613 (1980) and references therein.

[81] K.J. Schafer and K.C. Kulander, *Laser Phys.* **7**, 740 (1997)

[82] S. Vivirito and K. Taylor, private communication

[83] C. Cohen-Tannoudji, B. Diu and F. Laloe, *"Quantum Mechanics"*(Wiley, Paris,1 977)

[84] K. J. Schafer and K. J. Kulander, *Phys. Rev. Lett.* **78**, 638 (1997).

[85] J. B. Watson, A. Sanpera, X. Chen and K. Burnett, *Phys. Rev. A* **53**, R1962 (1996); A. Sanpera, J. B. Watson, M. Lewenstein and K. Burnett, *Phys.Rev.A* **54**, 4320 (1996)

[86] K. Miyazaki and H. Sakai, *J. Phys. B* **25**, L83 (1992); K. S. Budil, P. Salières, A. L'Huillier, T. Ditmire and M.D. Perry, *Phys. Rev. A* **48**, R3437 (1993); K. Miyazaki, H. Sakai, G. U. Kim, and H. Takada, *Phys. Rev. A* **49**, 548 (1994); N. H. Burnett, C. Kan and P. B. Corkum, *Phys. Rev. A* **51**, R3418 (1995); K. Miyazaki and H. Takada, *Phys. Rev. A* **52**, 3007 (1995); M. Yu. Ivanov, T. Brabec, and N. Burnett, *Phys. Rev. A* **54**, 742 (1996).

[87] X. Mu, *Phys. Rev. A* **43**, 5149 (1991); H. R. Reiss and V. P. Krainov, *Phys. Rev. A* **50**, R910(1994); J. Z. Kamiński, *Phys. Rev. A* **37**, 622 (1988); M. H. Mittleman, *Phys. Rev. A* **50**, 3249 (1994); M.V. Fedorov and J. Peatross, *Phys. Rev. A* **52**, 504 (1995); J. Z. Kamiński, A. Jaroń and F. Ehlotzky, *Phys. Rev. A* **53**, 1756 (1996); S.F.J. Larochelle, A. Talebpour and S.L. Chin, *J. Phys. B* **31**, 1215 (1998).

[88] M. L. Pons, R. Taieb, and A. Maquet, *Phys. Rev. A* **54**, 3634 (1996).

[89] D. B. Milošević and B. Piraux, *Phys. Rev. A* **54**, 1522 (1996).

[90] M.B. Gaarde, A. L'Huillier and M. Lewenstein, *Phys. Rev. A* **54**, 4263 (1996).

[91] M. Protopapas, P. L. Knight, and K. Burnett, *Phys. Rev. A* **49**, 1945 (1994); S. Long, W. Becker, and J. K. McIver, *Phys. Rev. A* **52**, 2262 (1995); M. Protopapas and P. L. Knight, *J. Phys. B* **28**, 4459 (1995); M. B. Gaarde, A. L'Huillier, and M. Lewenstein, *Phys. Rev. A* **54**, 4236 (1996); J. Z. Kaminski and F. Ehlotzky, *J. Phys. B* **30**, 5729 (1997); S. Varró and F. Ehlotzky, *Phys. Rev. A* **56**, 2439 (1997).

[92] D. M. Telnov, J. Wang, and S.-I Chu, Phys. Rev. A **52**, 3988 (1995); S. Erhard and E. K. U. Gross, *Proceedings of "VIIth International Conference on Multiphoton Processes "*, ed. P. Lambropoulos and H. Walther, p. 37 (IOP Publishing, Bristol, 1997); A. D. Bandrauk, S. Chelkowski, H. Yu, and E. Constant, *Phys. Rev. A* **56,** R2537 (1997); Ph. V Ignatovich, V. T. Platonenko, and V.V. Strelkov, preprint.

[93] H. Eichmann, S. Meyer, K. Riepl, C. Momma, and B. Welleghausen, *Phys. Rev. A* **50**, R2834 (1994); M. B. Gaarde, P. Antoine, A. Persson, B. Carré, A. L'Huillier, and C-G Wahlström, *J. Phys. B* **29**, L163 (1996).

[94] H. Eichmann, A. Egbert, S. Nolte, C. Momma, B. Wellegehausen, W. Becker, S. Long and J. K. McIver, *Phys. Rev. A* **51**, R3414 (1995).

[95] M. D. Perry and J. K. Crane, *Phys. Rev. A* **48**, R4051 (1993); S. Watanabe, K. Kondo, Y. Nabekawa, A. Sagisaka, and Y. Kobayashi, *Phys. Rev. Lett.* **73**, 2692 (1994); K. Kondo, Y. Kobayashi, A. Sagisaka, Y. Nabekawa, and S. Watanabe, *J.Opt. Soc. Am. B* **13**, 424 (1996).

[96] M. Protopapas, A. Sanpera, P. L. Knight, and K. Burnett, *Phys. Rev. A* **52**, R2527 (1995); A. Sanpera., J.B. Watson, M. Lewenstein and K. Burnett, *Phys. Rev. A*, **54**, 4320 (1996).

[97] P. Lambropoulos, *Phys. Rev. Lett.* **29**, 453 (1972) .

[98] W. Gordon *Zeit. für Physik* **40,** 117 (1926); D.M. Volkov, *Zeit. für Physik* **94,** 250 (1935).

[99] H.R. Reiss, *Phys. Rev. A* **22**, 1786 (1980); *Laser Phys.* **7**, 543 (1997) .

[100] H.S. Brandi, L. Davidovich and N. Zagury, *Phys. Rev. Lett.* **24,** 2044 (1981); H.S. Antunes Neto and L. Davidovich, *Phys. Rev. Lett.* **53**, 2238 (1984).

[101] S. Geltman, *J. Phys. B* **10,** 831 (1977); *Phys. Rev. A* **45,** 5293 (1992); *J. Phys. B* **27,** 257 (1994).

[102] V.P. Krainov and M.A. Preobrazenski, *Sov. Phys. JETP* **76,** 559 (1993) .

[103] W. Rudolph and B. Wilhelmi, *"Light Pulse Compression"* (Harwood Acad. Publ., London, 1989)

[104] R. Grobe and M.V. Fedorov, *Phys. Rev. Lett.* **68**, 2592 (1992); R. Grobe and M.V. Fedorov, *J. Phys. B* **26**, 1181 (1993).

[105] S. Geltman, *J. Phys. B* **27**, 1497 (1994).

[106] L.A. Collins and A.L. Merts, *Phys. Rev. A* **37**, 2415 (1988).

[107] J.N. Bardsley, A. Szöke and M.J. Comella, *J. Phys. B* **21**, 3899 (1988).

[108] K.J. LaGattuta, *Phys. Rev. A* **40**, 683 (1989).

[109] J. Javanainen, J.H. Eberly and Q. Su, *Phys. Rev. A* **38,** 3430 (1988); *Phys. Rev. Lett.* **64,** 862 (1990); Q. Su and J.H. Eberly, *J. Opt. Soc. Am.* **7**, 564 (1990); Phys. Rev. A **43**, 2474 (1991); C.K. Law, Q. Su and J.H. Eberly, *Phys. Rev. A* **44**, 7844 (1991); Q. Su, B.P. Irving and J.H. Eberly, *Laser Phys.* **7,** 568 (1997).

[110] Q. Su, *Laser Phys.* **3**, 241 (1993).

[111] M. Pont and R. Shakeshaft, *Phys. Rev. A* **44**, R4110 (1991).

[112] K.C. Kulander, K.J. Schafer and J.L. Krause, *Phys. Rev. Lett.* **66**, 2601 (1991).

[113] V.C. Reed and K. Burnett, *Phys. Rev. A* **42**, 3152 (1990); *Phys. Rev. A* **43**, 6217 (1991).

[114] O. Latinne, C.J. Joachain and M. Dörr, *Europhys. Lett.* **26**, 333 (1994); M. Dörr, O. Latinne and C.J. Joachain, *Phys. Rev. A* **52**, 4289 (1995).

[115] J.H. Shirley, *Phys. Rev. B* **138**, 979 (1965).

[116] R.M. Potvliege and R. Shakeshaft, *Phys. Rev. A* **38**, 1098 (1988); *Phys. Rev. A* **38**, 4597 (1988); *Phys. Rev. A* **38**, 6190 (1988); *Phys. Rev. A* **40**, 4061 (1990); M. Dörr, R.M. Potvliege, D. Proulx and R. Shakeshaft, *Phys. Rev. A* **43,** 3729 (1991); M. Dörr, P.G. Burke, C.J. Joachain, C.J. Noble, J. Purvis and M. Terao-Dunseath, *J. Phys. B* **25,** L275 (1993).

[117] L. Dimou and F.H.M. Faisal, *Act. Phys. Pol.* **A** 86, 201 (1993); L. Dimou and F.H.M. Faisal, *Phys. Rev. A* **46** 4564 (1994); F.H.M. Faisal, L. Dimou, H.-J. Stiemke and M. Nurhuda, *J. Nonlin. Opt. Phys. and Materials* **4,** 701 (1995).

[118] M.J. Offerhaus, J.Z. Kaminski and M. Gavrila, *Phys. Lett.* **112A,** 151 (1985); M. Gavrila, M.J. Offerhaus and J.Z. Kaminski, *Phys. Lett.* **118A,** 331 (1986); M. Pont, M.J. Offerhaus and M. Gavrila, *Z. Phys. D* **9,** 297 (1988); J. van de Ree, J.Z. Kaminski and M. Gavrila, *Phys. Rev. A* **37,** 4536 (1988); M. Pont, N.R. Walet, M. Gavrila and C.W. McCurdy; *Phys. Rev. Lett.* **61,** 939 (1988).

[119] M. Pont and M. Gavrila, *Phys. Rev. Lett.* **65,** 2362 (1990).

[120] J.G. Leopold and I.C. Parcival, *Phys. Rev. Lett.* **41**, 944 (1978); R. Grobe and C.K. Law, *Phys. Rev. A* **44**, 4114 (1991); F. Benvenuto, G. Casati and D.L. Stepelyanski, *Phys. Rev. A* **45,** R7670 (1992); S. Menis, R. Taieb, V. Veniard and A. Maquet, *J. Phys. B* **25,** L263 (1992).

[121] W.E. Cooke and R. Shakeshaft, *Phys. Rev A* **43**, 251 (1991).

[122] J. Grochmalicki, M. Lewenstein and K. Rzażewski, *Phys. Rev. Lett.* **66**, 1038 (1991).

[123] M. Dombrowski, A.T. Rosenberger and C.C. Sung, *Phys. Lett. A* **199,** 204 (1995), A.T. Rosenberger, C.C. Sung, S.D. Pethel and C.M. Bowden, *Laser Phys.* **7**, 563 (1997).

[124] O.V. Tikhonova and M.V. Fedorov, *Laser Phys.* **7**, 574 (1997).

[125] K. Burnett, V.C. Reed and P.L. Knight, *J. Phys.* **26,** 561 (1993).

[126] J.H. Eberly and K.C. Kulander, *Science* **262,** 1229 (1993) .

[127] N.B. Delone and V.P. Krainov, *"Multiphoton Processes in Atoms"* (Springer Verlag, Berlin, 1994) Chapter 10.

[128] S. Geltman, *Chem. Phys. Lett.* **237,** 286 (1995).

[129] J. Parker and C.R. Stroud Jr., Phys. Rev. A 41, 1602 (1990)

[130] M.V. Fedorov and A.M. Movsevian, *J. Opt. Soc. Am. B* **6**, 928 (1989).

[131] B.Piraux and R.M. Potvliege, *Phys. Rev. A* **57**, 5009 (1998).

[132] E. Lieb , *Rev. Mod. Phys.* **48,** 553 (1976).

[133] E. Lieb, M. Loss, and J.P. Solovej, *Phys. Rev. Lett.* **75,** 985 (1995).

[134] A. Fring, V. Kostrykin and R. Schrader, *J. Phys.* **B 29,** 5651 (1996).

[135] C. Figueira de Morisson Faria, A. Fring and R. Schrader, *J. Phys. B* **31,** 449 (1998).

[136] A. Fring, V. Kostrykin and R. Schrader, *J. Phys. A* **30,** 8599 (1997).

[137] M. Reed and B. Simon, *"Methods of Modern Mathematical Physics"* (Academic Press, New York, Vol. 2, 1972).

[138] H.A. Bethe and E.E. Salpeter, *"Quantum Mechanics of One and Two-Electron Atoms"* (Springer, Berlin, 1957)

[139] A. Wójcik, R. Parzyński and A. Grudka, *Phys. Rev. A* **55**, 2144 (1997); R. Parzyński and A. Wójcik, *Laser Phys.* **7**, 551 (1997).

[140] M. Abramowitz and I.A. Stegun, *"Handbook of Mathemathical Functions"* (Dover Publication, New York, 1970); L.J. Slater, *Confluent Hypergeometric Functions* (CUP, Cambridge, 1960); L.J. Slater, *"Generalized Hypergeometric Functions"* (CUP, Cambridge, 1966).

[141] E.J. Austin, *J. Phys. B* **12,** 4045 (1979).

[142] K.J. LaGattuta, *Phys. Rev. A* **40,** 683 (1989).

[143] A. Sanpera and L. Roso-Franco, *Phys. Rev. A* **41,** 6515 (1990).

[144] G. Scharf, K. Sonnenmoser and W.F. Wreszinski, *Europhys. Lett.* **10,** 19 (1989); *Phys. Rev. A* **44,** 3250 (1991).

[145] R. Robustelli, D. Saladin and G. Scharf, *Helv. Phys. Acta.* **70,** 96 (1997).

[146] T.P. Grozdanov, P.S. Krstic and M.H. Mittleman, *Phys. Lett. A* **149,** 144 (1990).

[147] J. Mostowski and J.H. Eberly, *J. Opt. Soc. Am. B* **8,** 1212 (1991).

[148] A. Sanpera, Q. Su and L. Roso-Franco, *Phys. Rev. A* **47,** 2312 (1993).

[149] E.A. Volkova, A.M. Popov and O.V. Smirnova, *JETP* **79,** 736 (1994).

[150] Q. Su, B.P. Irving, C.W. Johnson and J.H. Eberly, *J. Phys. B* **29**, 5755 (1996).

[151] S.G. Mikhlin, *"Integral Equations and their applications to certain problems in mechanics, mathematical physics and technology"* (Pergamon Press, Oxford, 1964).

[152] R. Sauerbrey, private communication.

[153] E. Sidick, A. Knoesen and A. Dienes, *J. Opt. Soc. Am. B* **12**, 1704 (1995).

[154] V. Krylov, A.Rebane, A.G. Kalintsev, H. Schwoerer and U.P. Wild, *Opt. Lett.* **20**, 198 (1995).

[155] J. Liouville, *J. Math. Pure Appl.* **18**, 71 (1853).

[156] F.G. Bass and V.G. Sinitsyn, *Ukrain. Fis. Shourn.* **17**, 124 (1972) (in Russian).

[157] W.H. Glenn, IEEE J. Quantum Electron. **QE-5**, 284 (1969).

[158] A.L. Aleksandrovski, S.A. Akhmanov, V.A. D'yakov, N.I. Zheludev and V.I. Pryalkin, *Sov. J. Quant. El.* **15,** 885 (1985).

[159] T. R. Zhang, H. Ro Choo and M. C. Downer, *Appl. Opt.* **29**, 3927 (1990).

[160] S. H. Ashworth, M. Joschko, M. Wörner, E. Riedle and T. Elsässer, *Opt. Lett.* **20**, 2120 (1995).

[161] S. Szatmari, P. Simon and M. Feuerhake, *Opt. Lett.* **21**, 1150 (1996).

[162] S.A. Akhmanov , A.S. Chirkin, K.N. Drabovich, A.I. Kovrigin, R.V. Khokhlov and A.P. Sukhorukov, *IEEE J. Quantum Electron.* **QE-4**, 598 (1968)

[163] R.R. Jones, D. You, and P. Bucksbaum, *Phys. Rev. Lett.* **70**, 1236 (1993).

[164] P.N. Butcher, D. Cotter, *"The Elements of Nonlinear Optics"* (Cambridge University Press, New York, 1990).

[165] D.J. Kaup, *Stud. Appl. Math.* **59**, 25 (1978).

[166] K. Khusnutdinova and H. Steudel, *J. Math. Phys* **39**, 3754 (1998).

[167] See e.g. G. I. Stegeman, M. Sheik-Bahae, E. Van Stryland and G. Assanto, *Opt. Lett.* **18**, 13 (1993); M. M. Fejer, *Phys. Today* **47,** 25 (1994) and references therein; E. Sidick, A. Dienes and A. Knoesen, *J. Opt. Soc. Am. B* **12**, 1713 (1995); A. Otomo, G. I. Stegeman, W. H. G. Horsthuis and G. R. Möhlman, *Appl. Phys. Lett.* **68**, 3683 (1996); M. A. Arbore, O. Marco, and M. M. Fejer, *Opt. Lett.* **22**, 865 (1997).

[168] F. Calogero, in: ed. V.E. Zakharov, *"What is integrability"*, p.1 (Springer, Berlin, 1991).

[169] I. Drevensek, R. Torre, M. Copic, *Molec. Cryst.* **251**, 101 (1994) ; G. Assanto and I. Torelli, *Opt. Comm.* **119**, 143 (1995) .

[170] E. Hille, *"Ordinary Differential Equations in the Complex Plane"* (Wiley & Sons, New York, 1976).

[171] This type of equation was first investigated in connection with the theory of lunar motion by G.W. Hill, *Acta Math.* **8**, 1 (1886); it is also well known in the quantum theory of metals and semiconductors, see, e.g., L. W. Casperson, *Phys. Rev. A* **30,** 2749 (1984); S.M. Wu and C.C. Shih, *Phys. Rev. A* **32,** 3736 (1985); K. Takayama, *Phys. Rev. A* **34**, 4408 (1986) .

[172] W.H. Press, S.A. Teukolsky, W.T. Vetterling, B.P. Flannery, *"Numerical Recipes"*(Cambridge University Press, New York, 1992).

[173] H. Eichmann, PhD thesis, University of Hannover (1996).

[174] Y. Inui, Y. Tanabe and Y. Onodera, *"Group Theory and its Application in Physics"* (Springer, Berlin, 1996).